Escola Superior d'Enginyeries Industrials,
Aeroespacial i Audiovisual de Terrassa

UNIVERSITAT POLITÈCNICA DE CATALUNYA

Polytechnic University of Catalonia (UPC)

Terrassa School of Industrial, Aerospace and Audiovisual Engineering
(ESEIAAT)

Design and Performance Analysis Study of an Ion Thruster

Final Degree Project - Report

Bachelor's Degree in Aerospace Technology Engineering

Author: Carlos Sánchez Lara

Director: Josep Oriol Lizandra Dalmases

Terrassa, 22nd June, 2016

Polytechnic University of Catalonia (UPC)

Abstract

Terrassa School of Industrial, Aerospace and Audiovisual Engineering

Department of Aerospace Engineering

Bachelor's Degree in Aerospace Technology Engineering

Design and Performance Analysis Study of an Ion Thruster

by Carlos Sánchez Lara

Given that the world space market evolves towards low-cost solutions, electric propulsion is going to supersede current chemical devices over the next few years. Ion thrusters are the most developed electric engines intended for propelling large spacecraft during in-space manoeuvers, offering the highest efficiencies at reasonable power and thrust levels. Although their characteristics allow to cut down missions' costs, their development and refinement is largely experimental, involving expensive and long iterative processes to reach an optimum configuration.

On the one hand, this study provides a numerical comparison between chemically and electrically propelled missions. It demonstrates the potential of ion engines for current and future promising applications, and gives us a preliminary view of the launch cost savings using electric propulsion.

On the other hand, the study provides a quasi-unidimensional model of an ion thruster's ionisation chamber so as to assess its performance, for different operating conditions and for a given design. Moreover, the code implemented enables to optimise the parameters influencing thruster's performance for certain mission's specifications. Given the model's limitations, the degree of accuracy of the results are constrained. Nevertheless, it should provide a guidance for the thruster designing and refinement stages.

Acknowledgements

I would like to express my gratitude to all the people that made possible the elaboration of this study. I would like to specially thank to my supervisor, Oriol Lizandra. His contribution to the study has been essential to complete a high-quality report, given my initial limited awareness about space propulsion. Moreover, his support and enthusiasm have encouraged me to continue my efforts to investigate and broaden my knowledge on the fascinating world of space engineering.

Finally, my most sincere gratitude to my family for their support, patience and understanding.

Contents

List of Figures

List of Tables

Nomenclature

a	=	Semi-major axis of an ellipse [km]
a_T	=	Acceleration provided by the thrusters [m/s^2]
A_g	=	Area of grids through which the ion beam is extracted [m^2]
B	=	Magnetic field [A/m]
C_0	=	Primary electron utilisation factor [(A eq.)$^{-1}$]
d_a	=	Gap between screen and accelerator grids [mm]
d_d	=	Gap between accelerator and decelerator grids [mm]
D_a	=	Accelerator grid hole diameter [mm]
D_s	=	Screen grid hole diameter [mm]
e	=	Electron charge [C]
E	=	Electric field [V/m]
f_A	=	Fraction of ion current to anode surfaces
f_B	=	Extracted ion fraction
f_c	=	Fraction of ion current to cathode surfaces
F_L	=	Lorentz force [N]
g_0	=	Earth surface's gravity [m/s^2]
G	=	Gravitational constant [m^3/(kg·s^2)]
I_{sp}	=	Specific impulse [s]
j_B	=	Beam ion current density [A/m^2]
j_e	=	Electron current density [A/m^2]
j_i	=	Ion current density [A/m^2]
J_A	=	Ion current to anode potential surfaces [A]
J_B	=	Ion beam current [A]
J_B^+	=	Singly charged ion beam current [A]
J_B^{++}	=	Doubly charged ion beam current []
J_C	=	Ion current to cathode potential surfaces []
J_D	=	Discharge current [A]
J_E	=	Cathode emission current [A]
J_L	=	Primary electron current to the anode [A]
J_M	=	Maxwellian electron current to the anode [A]
J_P	=	Total ion production rate [A]
J_P'	=	Ion production rate by primary electron [A]
J_{acc}	=	Ion current intercepted by accelerator grid [A]
J_j	=	Production rate of jth excited state [A]

k	=	Boltzmann constant [m^{2}kg/(s^{2}K)]
l_e	=	Primary electron containment length [m]
m	=	Instantaneous spacecraft mass [kg]
$\dot{m}$	=	Propellant flow rate [A]
m_e	=	Electron mass [kg]
m_i	=	Ion mass [kg]
$\dot{m}_{p_T}$	=	Total propellant mass flow rate [kg/s]
$\dot{m}_p$	=	Mass propellant flow rate [kg/s]
M	=	Molecular mass of xenon [u]
M_E	=	Earth mass [kg]
M_f	=	Final mass of spacecraft [kg]
M_{p_0}	=	Propellant mass [kg]
M_g	=	Power plant mass [kg]
M_i	=	Initial mass of spacecraft [kg]
$\dot{n}_0$	=	Neutral atom loss rate [A eq.]
n_0	=	Neutral atom density [m^{-3}]
n_h	=	Number of holes of the grids
n_M	=	Maxwellian electron density [m^{-3}]
n_P	=	Primary electron density [m^{-3}]
n_e	=	Electron density [m^{-3}]
n_i	=	Ion density [m^{-3}]
P_g	=	Generated power [W]
q	=	Electric charge [C]
Q_0^+	=	Maxwellian electron rate factor for ionization of neutral atoms [m^3/s]
r	=	Doubly-to-singly charged ion current ratio
$\vec{r}$	=	Spacecraft position vector [km]
r_1	=	LEO radius [km]
r_2	=	GEO radius [km]
r_C	=	Larmor radius [m]
R	=	Net to total voltage ratio
R_E	=	Earth radius [km]
R_m	=	Initial to final spacecraft mass ratio
t	=	Time [s]
t_H	=	Hohmann transfer duration [s]
t_a	=	Accelerator grid thickness [mm]

t_s	=	Screen grid thickness [mm]
T	=	Thrust [N]
T_H	=	Hohmann transfer ellipse period [s]
T_A	=	Maxwellian electron temperature at anode surface [eV]
T_M	=	Maxwellian electron temperature in bulk plasma [eV]
T_T	=	Total thrust [N]
T_e	=	Electron temperature [eV]
T_w	=	Ionisation chamber walls temperature [K]
u	=	Exhaust velocity [m/s]
U_+	=	Ionisation energy [eV]
U_{ex}	=	Lumped excitation energy [eV]
U_j	=	Excitation energy of jth excited state [eV]
U_l	=	Lowest excitation energy [eV]
$\vec{v}$	=	Spacecraft velocity vector [km/s]
v_0	=	Neutral atom velocity [m/s]
v_1	=	Initial velocity of Hohmann transfer velocity [km/s]
v_2	=	Final velocity of Hohmann transfer velocity [km/s]
v_{c_1}	=	LEO velocity [km/s]
v_{c_2}	=	GEO velocity [km/s]
v_B	=	Bohm velocity [m/s]
v_{SSTO_1}	=	Velocity at the perigee of SSTO [km/s]
v_e	=	Electron velocity [m/s]
v_i	=	Ion velocity [m/s]
v_n	=	Circular ion velocity subjected to a magnetic field [m/s]
v_p	=	Primary electron velocity [m/s]
Δv_1	=	First delta-V in Hohmann transfer [km/s]
Δv_2	=	Second delta-V in Hohmann transfer [km/s]
Δv_H	=	Total delta-V for Hohmann transfer [km/s]
Δv	=	Change in velocity (delta-V) [km/s]
V	=	Volume of ion production region [m³]
V_A	=	Anode sheath voltage [V]
V_C	=	Hollow cathode potential [V]
V_D	=	Discharge voltage [V]

V_N	=	Net voltage [V]
V_T	=	Total voltage [V]
α	=	Specific power plant mass [kg/W]
β	=	Doubly charged current correction factor
ϵ_0	=	Average plasma ion energy cost considering ionisation and excitation processes only [eV]
ε_0	=	Permittivity in vacuum [F/m]
ε_B	=	Beam ion energy cost [eV/plasma ion]
ε_M	=	Average energy of Maxwellian electrons [eV]
ε_P	=	Average plasma ion energy cost [eV/plasma ion]
ε_P^*	=	Baseline plasma ion energy cost [eV/plasma ion]
η_t	=	Electric efficiency
η_u	=	Propellant utilisation efficiency
λ_D	=	Debye length [m]
μ	=	Gravitational parameter of the Earth [km³/s²]
μ_0	=	Permeability in vacuum [N/A²]
σ_+	=	Ionisation collision cross section [m²]
σ_+'	=	Ionisation collision cross section at the primary electron energy [m²]
σ_0'	=	Total inelastic collision cross section at the primary electron energy [m²]
σ_{ex}	=	Total excitation collision cross section [m²]
σ_{ex}'	=	Total excitation collision cross section at primary electron energy [m²]
σ_j	=	Excitation collision cross section of the jth state [m²]
ω_C	=	Cyclotron frequency [rad/s]
ω_p	=	Plasma frequency [rad/s]
ϕ	=	Potential [V]
ϕ_P	=	Plasma potential [V]
ϕ_{ps}	=	Potential in the plasma sheath [V]
ϕ_w	=	Potential drop in the sheath [V]
ϕ_0	=	Grid system transparency to neutral atoms
ϕ_a	=	Transparency of the accelerator grid to atoms
ϕ_i	=	Transparency of the screen grid to ions
ϕ_s	=	Transparency of the screen grid to neutral atoms
ρ	=	Charge density [C/m³]

Physical constants

Symbol		Value	Description
e	=	$1.6022 \cdot 10^{-19}\, C$	Electron charge
g_0	=	$9.81\, m\, s^{-2}$	Earth surface's gravity
G	=	$6.674 \cdot 10^{-11} m^3 kg^{-1} s^{-2}$	Gravitational constant
k	=	$1.3806 \cdot 10^{-23} m^2 kg\, s^{-2} K^{-1}$	Boltzmann constant
m_e	=	$9.1094 \cdot 10^{-31} kg$	Electron mass
M	=	131.293 u	Molecular mass of xenon
M_E	=	$5.972 \cdot 10^{24} kg$	Earth mass
R_E	=	$6378\, km$	Earth radius
ε_0	=	$8.8542 \cdot 10^{-12} F m^{-1}$	Permittivity in vacuum
μ	=	$3.9860 \cdot 10^5 km^3 s^{-2}$	Gravitational parameter of the Earth
μ_0	=	$4\pi \cdot 10^{-7} N A^{-2}$	Permeability in vacuum

Table 0.1: Physical constants.

Introduction

Aim of the Project

The main goal of this project is to develop a preliminary study of a spacecraft's electrostatic ion thruster, whose suitability will be assessed for a particular mission. Brophy's Theory shall be used in order to develop a quasi-unidimensional model of the device's ionisation chamber, allowing to determine its performance for different operating conditions.

Scope

Due to the nature of the study, it will consist of two main differentiated blocks; a first research and investigation part, and a second program development and implementation part.

The scope of the present work is structured as follows:

- Background study. Analysis of current space propulsion systems.
- State of the art research. Analysis of the ion thruster existing applications.
- Specific mission analysis so as to compare chemical and electric propulsion performance, justifying the ion thruster as a suitable propulsion system for the particular mission.
- Study of basic electromagnetism and plasma physics.
- Preliminary analytical study of an electron bombardment ion thruster.
- Ionisation chamber quasi-unidimensional model to assess ion thruster's performance for different operating conditions.
- Results validation.
- Actuations analysis so as to optimise the thruster operation given a specific mission.
- Conclusions

Requirements

The requirements for the study are listed below:

- A new non-commercial code for assess ion thruster's performance must be created.

- The model developed for the ionisation chamber must be quasi-unidimensional.

- The program must be able to consider different thruster operating conditions.

Justification

Aerospace industry involves a very wide range of engineering disciplines. Amongst them, propulsion is one of the most important branches, since any possible mission largely depends on it.

Nowadays, electric propulsion is considered in operations like orbit raising manoeuvres, station keeping or interplanetary travel. From all the propulsive systems, ion thrusters have been the most seriously considered commercially for such missions, as they require high change in velocity which can be achieved over long periods of time.

Up to this day, the development of engine designs capable of meeting these requirements has been largely experimental. Ion thrusters' development has generally been accomplished by a procedure in which the design parameters that influence thruster's performance are physically varied until an acceptable configuration is obtained. First of all, this procedure is time consuming, since a large number of parameters is involved. In addition, changes in the missions' specifications may be characterised by different propulsion requirements, implying the repetition of the iterative process.

In order to accurately assess the thruster performance without the need to perform such expensive and long tests, analytical studies and numerical models must be developed. They should allow to estimate the capabilities of the ion engine with a certain degree of accuracy or, at least, they should enable to provide a guidance for the iterative process mentioned above. It could be of crucial importance in financial matters since testing and development costs would be saved.

Analysing the outcomes, by comparing them with real experimental data, it will be seen how exact is the model employed for the simulations, and to what extent it is reliable.

Chapter 1.   Background

Since Space Age began with Sputnik 1 launch in 1957, aerospace industry has been evolving driven by the demand of the current society. Communication satellites nowadays are the best known application of space technology, since nobody could imagine their life today without services such as long distance calling or satellite television. However, there are many others uses of Earth Orbiting spacecraft, including navigation systems, Earth observation or scientific research. Some examples are GPS satellites, the International Space Station or the Hubble Space Telescope. Furthermore, technology development has enabled us to complete exploration missions, reaching important targets like the Moon or different planets in the Solar System.

One of the main challenges in each mission is to find the most suitable space propulsion system. A spacecraft does not only have to leave the Earth's surface, but it also must achieve its optimum orbit and keep it, or speed up the vehicle in order to decrease the travel time.

Until now, the only way to escape from the dense atmosphere is through huge amounts of fuel and large thrusts (achieved with chemical propulsion), but once in the space, the propulsion requirements are very different. Low thrust propulsion systems are ideal for such in-space applications and, from among them all, we can highlight the electric thrusters.

They offer several advantages with respect to the conventional chemical engines. For example, they are more efficient, requiring much less propellant to produce the same overall effect. Propellant is ejected much faster, generating higher specific impulses (I_{sp}), which is a measure of the efficiency of rockets. Consequently, they provide small accelerations, and it takes much longer to achieve particular speeds. Nevertheless, the thrust they produce can be applied over long periods of time, enabling spacecraft to acquire high speeds needed for interplanetary missions. Moreover, they are able to regulate their thrust, making it possible to control the spacecraft's attitude with exceptional precision. Next figure reflects the working ranges of thrust and I_{sp} for both propulsion systems.
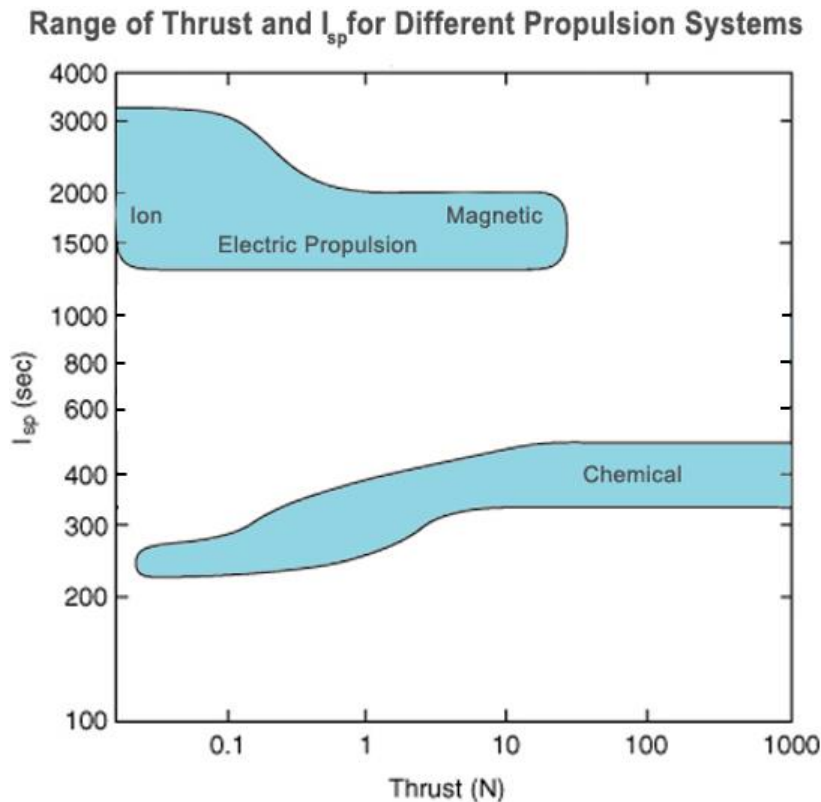
Figure 1.1: Range of thrust and I_{sp} [1].

In Fig 1.1, we can see that electrical systems provide lower accelerations (low thrust levels), but require much less propellant mass (high I_{sp}) than chemical propulsion systems. The advantages of the electrical engines make them suitable for many space missions.

Nowadays, electric propulsion is considered in operations like:

- Station keeping: keeping a spacecraft in a particular orbit counteracting perturbations.
- Attitude control: controlling the orientation of the vehicle with respect to a reference frame.
- Orbit transfer: moving a spacecraft from one orbit to another.
- Deep space missions: propelling a spacecraft to speed it up towards its target.

These manoeuvres require a high change in velocity, which can be achieved over long periods of time. The most appropriate applications of these systems make use of their long lifetime (10-15 years) [2] when significant thrust is not needed, for example, when counteracting the atmospheric drag effect or compensating the gravitational perturbations.

The concept of electric propulsion dates back to 1911, being introduced by Konstantin Tsiolkovsky in its first published mention about electric propulsion [3]. In the period between 1929 and 1931, in Leningrad's Gas-Dynamics Laboratory, it was designed and tested the first electric thruster prototype, but it was not until 1964, after some years of new concepts and models developing, that the first working ion thruster was sent into a suborbital flight, being operative during 31 minutes before falling back to Earth [4]. It was built in 1959 at NASA facilities and was tested during the 1960s [3]. Since its conception, different types of electric thrusters (discussed in next section) have been developed and tested in space.

1.1. Electric thruster types

The basic principle of electric propulsion is to apply electrical energy to the propellant from an external power source, and then, to expel it at high speed. We can classify electric thrusters based on the type of force used to accelerate the gas or plasma.

1.1.1. Electrothermal thrusters

An electrothermal engine uses electric power to heat a gas causing it to expand through a nozzle and generate thrust. Two basic types are in use today: the Resisto-jet and the Arc-jet thrusters.

In the Resisto-jet, heating is usually achieved by sending electricity through a resistor consisting of a hot incandescent wire (see Fig. 1.2). The filament cannot be cooled, and so, the gas cannot be hotter than the service temperature of the wire's material, thus fixing the ratio of flow rate to power input. Specific impulse values near 300 s are achievable [5].
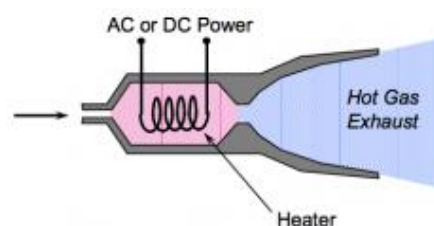
Figure 1.2: Resisto-jet simple diagram [6]*.*

In the Arc-jet, the propellant gas is heated by passing an electric arc through the flow (see Fig. 1.3). The temperature limit can be much higher than that of Resisto-jets, since highest temperatures are not in contact with engine walls. The problem is that gas particles strike the

surface of the cathode at high speed, causing vaporisation of the material. This limits the life of the cathode, and places a limit on the current that can be passed through the arc. They provide specific impulses typically in the 500–600 s range [5], higher than Resisto-jets because of the higher temperatures. However, its efficiency is lower.
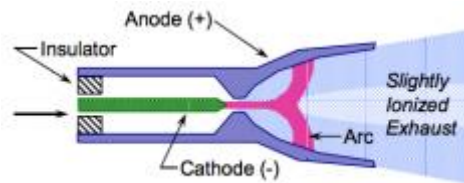
Figure 1.3: Arc-jet simple diagram [6].

1.1.2. Electromagnetic thrusters

A thruster is considered electromagnetic if ions are accelerated either by the Lorentz force or by effect of an electromagnetic field where the electric field is not in the direction of the acceleration. The magnetic and electric fields are created using a power source, which could be used to ionise the propellants as well. The most important electromagnetic thrusters are:

- Magneto Plasma Dynamic (MPD) thruster: It is the most powerful type and can generate thrust levels in the order of Newton. It consists of a central cathode sitting within a larger cylindrical anode. A gas is pumped into the annular space between the cathode and the anode. There, it is ionised by an electric current flowing radially from the cathode to the anode. This current induces an azimuthal magnetic field, which interacts with the same current that induced it to generate the thrust-producing Lorentz force. 6000 s of I_{sp} could be achieved. Such technology have been explored academically, but commercial interest has been low due to several remaining problems, such as high input power requirements for optimum performance (>100 KW) [7].

- Variable Specific Impulse Magnetoplasma Rocket (VASIMR): It uses radio waves to ionise and heat a propellant, and magnetic fields to accelerate the resulting plasma to generate thrust (it can be thought of as a convergent-divergent nozzle for ions and electrons). It is electrodeless, which is advantageous in that it eliminates problems with erosion. Furthermore, since every part of a VASIMR engine is magnetically shielded and does not come into direct contact with ions or electrons, it does not have structural limitations (gases can reach temperatures in the order of

millions of degrees). Theoretically, it could reach up to 30,000 s of I_{sp}, and continuous forces of thousands of Newton. It would be possible since this engine can deal with huge power inputs (hundreds of MW) [8].
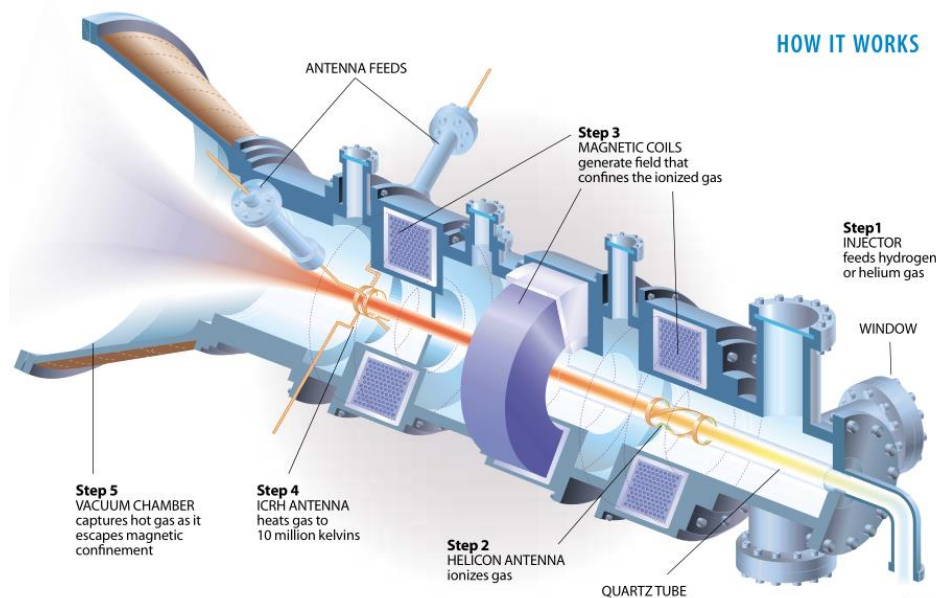
Figure 1.4: VASIMR engine schematic [8].

1.1.3. Electrostatic thrusters

Electrostatic thrusters accelerate heavy charged atoms (ions) by means of a purely electrostatic field. The two most important types are ion thruster and Hall-effect thruster, which have been the most seriously considered commercially for primary electric propulsion.

- Ion thrusters: They produce thrust by accelerating ions through the application of an electric field between two grids. The plasma is formed in a chamber by ionising the propellant. There are several ways of ionising the gas, being electron bombardment the most commonly used. Apart from the ions, electrons are also ejected from a separate cathode placed near the ion beam, called the neutraliser, to ensure that equal amounts of positive and negative charges are emitted. The main limitation of these engines, that restricts the flow and thrust, is the space-charge phenomenon. Xenon is often used as propellant and typical values of specific impulse are around 3000 s [7].
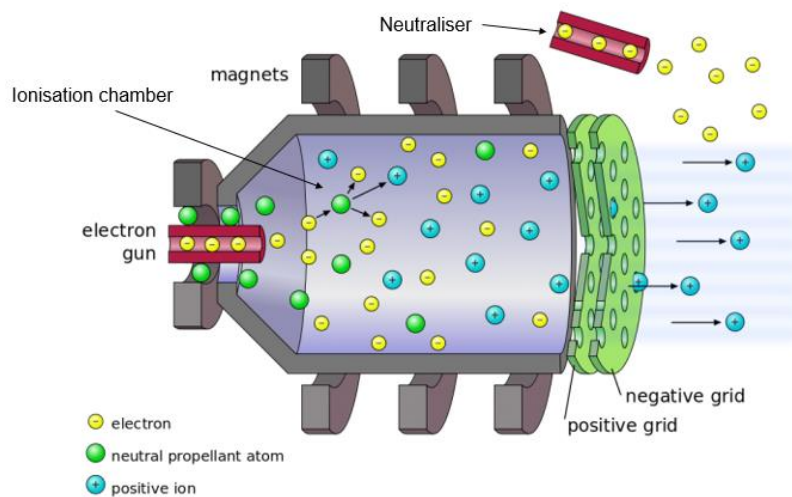
Figure 1.5: Illustration of an electron bombardment ion thruster [9].

- Hall-effect thrusters: They are electrostatic ion accelerators in which a magnetic field, perpendicular to the flow, is placed to confine an electron plasma at the open end of the thruster, playing the role of a cathode. The combination of the radial magnetic field and axial electric field causes the electrons to drift in azimuth, forming the Hall current from which the device gets its name. The trapped plasma is used to ionise propellant by means of colliding the atoms with high-energy electrons. Once positively charged, plasma is accelerated by the electric field to produce thrust. Typical I_{sp} values are in the 1,500 to 3,000 s range, while efficiency is near 60 %, lower than that of ion engines [7].
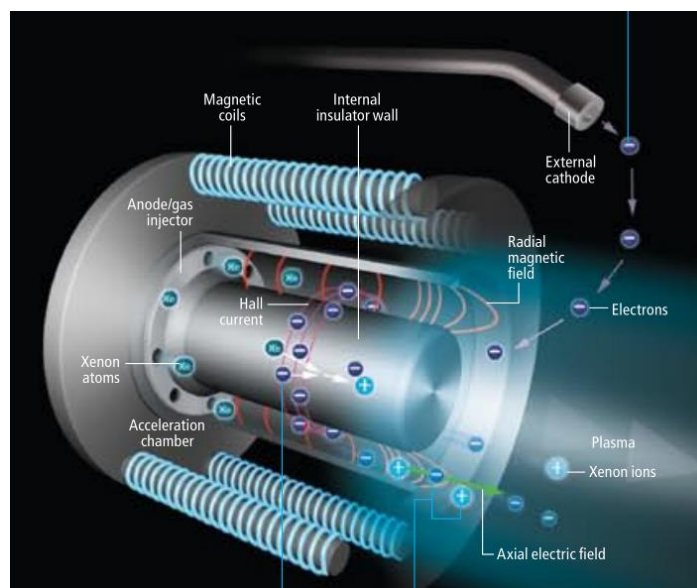
Figure 1.6: Hall thruster schematic [7].

Here below, actual performance space test data from different electric thrusters are compared.

Thruster type	Model	I_{sp} [s]	Thrust [mN]	Input power [W]	Efficiency [%]	Specific thrust [mN/kW]	Applications
Resisto-jet	XR-150	110	250	95	65	2632	Station keeping, attitude control, (for mini- and micro-satellites)
Arc-jet	AT 1K Arcjet	605	150	1000	50	150	Collision avoidance, reaction wheel desaturation, fast deorbiting
MPD[1]	200KW Li-LFA	4000	12,500	200,000	48	63	Nuclear-powered deep-space exploration (not possible right now)
VASIMR[1]	VX-200	4900	5800	200,000	72	29	Nuclear-powered deep-space exploration (not possible right now), station keeping, orbit insertion
Ion-gridded	25-cm XIPS	3500	168	4500	87	37	Orbit transference, station keeping, attitude control, deep-space exploration
Hall-effect	BPT-4000	2020	252	4500	55	56	Station keeping,

Table 1.1: Performance comparison of electric thrusters [10]*,* [11]*,* [12]*,* [13]*,* [14]*.*

From the table above, we can draw several conclusions. The first two engines (electrothermal ones) show the highest thrusts per power unit, so they require lower input power to perform the same thrust. Consequently, they provide the poorest specific impulses, which makes them unsuitable for many space missions (they would need huge amounts of fuel). Electromagnetic thrusters seem to be the most promising systems since they can deal with high input power because of their lack of structural limitations. They can provide high I_{sp}'s and relatively important thrusts. We must highlight the VASIMR's capacity of modifying its performance as required to meet the needs of the mission. Nevertheless, their demands are not affordable by current electric power sources, so nuclear reactors in spacecraft would be needed, which today entail several risks. Finally, electrostatic thrusters are the space tested systems that best fulfil propulsion requirements, since they have high specific impulses and require reasonable power levels, making possible long operations (10-15 years) with small amounts of fuel. Amongst them, ion thruster is the most developed system to this day, providing higher I_{sp} and efficiency than Hall thruster.

Therefore, nowadays, ion propulsion systems are the most suitable option for space applications and, for that reason, this work will focus on them.

---

[1] There are not real space applications yet. These are laboratory results.

Chapter 2.   Ion thruster: state of the art

Ion thrusters are the best developed type of electric propulsion device, whose conception dates back to the 1910's. Robert Hutchings Goddard presented in 1917 the world's first documented electrostatic ion accelerator intended for propulsion [3], although it was not until 1959 that the first working ion thruster was built at the NASA Glenn Research Center facilities, by Harold R. Kaufman. In the 1960s, NASA Glenn undertook a spaceflight test program called Space Electric Rocket Test (SERT), launching in 1964 two ion engines aboard the SERT 1 spacecraft, to perform a suborbital flight, that is, a spaceflight in which the spacecraft reaches space, but its trajectory does not complete one orbital revolution. One of them did not work and the other operated for 31 minutes [4]. After that, SERT 2 mission was carried out, which was equipped with another two ion thrusters and performed an orbital flight. This time, they operated for nearly 5 and 3 months respectively [15].

Since then, the main concepts of the system have been evolving through progressive refinements of the designs, driven by the needs of long operational lifetime, low propellant and structural mass and high efficiency, fundamental requirements for space propulsion.

There have been many configurations proposed throughout history, and the most significance differences between the various designs stem from the method of ionising the propellant atoms (discussed later on). Only the electron bombardment type, the radio-frequency ionised thruster and the Electron Cyclotron Resonance thruster are still in use. Other concepts, such as Cesium Contact thrusters and duo-plasmatron sources have been largely abandoned, and two new special devices, the Field Emission Electrostatic Propulsion (FEEP) and Ionic Liquid Ion Source (ILIS) have been recently added to the roster [16]. The importance of the ionisation method lies in the power required to operate the device, which, in turn, directly depends on the fuel employed.

The early designs used mercury as propellant, but its toxicity tended to contaminate the spacecraft. Current ion thrusters use xenon gas. It has a high atomic number and it is easy to ionise. Moreover, it is an inert gas and, therefore, provokes low erosion, lengthening the lifetime of the engine. The major drawback is the scarce supplies of such gas and, therefore,

its high cost. Later on, the impact of the propellant on the thruster's performance will be analysed, and we will see why xenon is the most employed gas.

 The first xenon ion drive ever flown was a Hughes[2] engine launched in 1979 on the SCATHA satellite [4], a United States Air Force satellite designed to collect data on the electrical charging of spacecraft. After that, several companies devoted their efforts to develop xenon ion engines. NASA Glenn and JPL (Jet Propulsion Laboratory) created the NSTAR project, whose purpose was to develop ion engines for deep space missions. Deep Space 1 spacecraft used these engines as primary propulsion system to demonstrate the capacity of long-duration use of an ion thruster on a scientific mission.

In August 1997, Hughes launched the first commercial use of a xenon ion engine on PanAmSat 5, a communications satellite launched on a Russian Proton rocket. This ion thruster (the so-called Xenon ion propulsion system (XIPS)) was used to maintain the position of the communications satellite in its proper orbit (geostationary) and orientation [4].

Nowadays, there are hundreds of active space vehicles fitted with electric propulsion systems, including deep space probes (e.g. *Dawn*[3]). Dozens of ion drives are currently operating on commercial spacecraft, mostly in communications satellites in geosynchronous orbit, for orbital station-keeping and attitude control, their main applications.

Nevertheless, different companies have recently started considering electric propulsion for orbit raising. It consists in transferring a satellite to the desired orbit from a lower one. The first use of ion thrusters for transferring a satellite from super-synchronous to geosynchronous (schematic of the manoeuver in Fig. 3.3) orbit dates from March 2015, when a Space X Falcon 9 rocket launched and placed the "Eutelsat 115 West B" and "ABS-3A" satellites on the planned transfer orbit. They were equipped with Boeing 702SP buses [17]. A satellite bus is the infrastructure of a satellite, a general model on which a spacecraft is based, containing among other things, the propulsion systems to execute orbit raising and station-keeping manoeuvres. After some time, both communications satellites were operative and had

---

[2] Hughes Research Laboratories was the research arm of Hughes Aircraft. It is a dedicated research centre, established in 1960, in Malibu.

[3] The Dawn spacecraft is a deep space probe propelled by three xenon ion thrusters based on an evolution of the NSTAR technology used in Deep Space 1 mission.

reached their orbits. Such transfer, as well as the orbits employed, will be explained in Chapter 3.

The problem of orbit raising with only electric propulsion is that the procedure could take up to six months, delaying the start of service for new commercial communications satellites. It is a trade-off for private operators, which must give up quicker revenue from a new satellite for the reduced launch costs or extra communications payload of a lighter spacecraft.

Down below, all spacecraft fitted with ion engines, to this day, are listed in chronological order. The role of the thrusters in their respective missions is not specified, but it can be attitude control, main propulsion system for deep space missions or orbit raising.

Spacecraft's name	Launch Date	Type of Drive	Comment
SERT 1	July 1964	Mercury Ion Engine	First ion engine in space
Program 661A	August 1964	Caesium ion engine	Suborbital, experimental test
SNAP-10A	April 1965	Caesium ion engine	Only nuclear reactor launched by the US
ATS-4	August 1968	Caesium ion engine	Experimental
ATS-5	August 1969	Caesium ion engine	Experimental
SERT 2	February 1970	Mercury ion engine	Experimental
ATS-6	May 1974	Caesium ion engine	Experimental
SCATHA (P78-2)	January 1979	Xenon ion source	First xenon ion flown
EURECA	1992-93	RIT-10 ion engine	Radio frequency ion propulsion
ETS-6 (Kiku 6)	August 1994	XIPS	Experimental
PAS-5	August 1997	XIPS	First commercial satellite with ion propulsion system
Galaxy 8i	December 1997	XIPS	Bus based on HS-601HP
Astra 2A	August 1998	XIPS	Bus based on HS-601HP
Deep Space 1	1998–2001	NSTAR	Deep space mission
Satmex 5	December 1998	XIPS	Bus based on HS-601HP
PAS 6B (Intelsat 6B)	December 1998	XIPS	Bus based on HS-601HP
Astra 1H	June 1999	XIPS	Bus based on HS-601HP
DirecTV 1R	October 1999	XIPS	Bus based on HS-601HP
Satellites based on the bus HS-702 / BSS-702	Starting on December 1999	XIPS	First satellite: Galaxy 11
Galaxy 10R	January 2000	XIPS	Bus based on HS-601HP
Superbird 4	February 2000	XIPS	Bus based on HS-601HP

Galaxy 4R	April 2000	XIPS	
PAS 9 (Intelsat 9)	July 2000	XIPS	
PAS 10 (Intelsat 10)	May 2001	XIPS	Bus based on HS-601HP
Astra 2C	June 2001	XIPS	Bus based on HS-601HP
Artemis	July 2001	Radio-frequency ion thruster	Two RIT-10 thrusters
DirecTV 4S	November 2001	XIPS	Bus based on HS-601HP
AsiaSat 4	April 2003	XIPS	Bus based on HS-601HP
Hayabusa	May 2003	4 µ10 microwave ion thruster	
Galaxy 13 (Horizons 1)	October 2003	XIPS	Bus based on HS-601HP
MEASAT 3	December 2006	XIPS	Bus based on HS-601HP
Dawn	September 2007	NSTAR	Three ion engines
GOCE	March 2009	Two gridded ion thrusters	Precise thrust control
ABS-3A and Eutelsat 115 West B	2015	XIPS	First bus for orbit transfer

Table 2.1: Chronological flights of ion engines [18].

As we can see in Table 2.1, first ion engines employed caesium or mercury as propellant. After some studies, xenon was imposed, and since then, it has been used in almost all applications.

On the other hand, orbit raising manoeuvres have recently been introduced as a promising ion thruster's application. Thus, they shall be analysed in the following section, where we will compare different transfer missions, carried out either by chemical or electric propulsion, to assess the advantages and drawbacks of these operations.

Chapter 3. Mission analysis

Costs related with placing satellites into orbit are very high, since large rockets and huge amounts of fuel are required to launch them into parking orbits around the Earth. After that, they must be propelled in order to reach their operative height, by means of circularisation, Hohmann transfer or any other method providing equivalent results. Once in the optimum trajectory, satellites are thrusted so as to counteract gravitational perturbations and compensate drag forces during their lifetime.

Private or public sectors must pay for such services, which involve a lot of money that is highly dependent on the propulsion system employed for the second and third phases discussed above.

Considering only the orbit raising phase, higher specific impulses imply lower fuel consumption. Therefore, to achieve a final orbit, having the same point of departure, a spacecraft propelled electrically would require less mass than another propelled with chemical engines. It would reduce the total spacecraft mass, requiring lower power at blast off, or allowing companies to increase payload. It is noteworthy that placing a kilogram of anything into Earth orbit costs as much as 22,000 $ [7].

Despite the efficient ion thrusters and their low fuel consumption, most satellites continue using conventional liquid propellants for their orbit-raising engines. It is due to the fact that they spend days or weeks in placing a spacecraft into their operative orbit, instead of several months, the achievable values for current ion drives.

Therefore, there is a trade-off between time employed in this operations and costs involved.

In this section we are going to discuss whether it is suitable or not employing this type of electric propulsion for orbit transfer missions, and to what extent expenses are affected.

3.1. Transfers analysis

To start with, some basic concepts must be introduced. First of all, an orbit around the Earth can be either circular or elliptical. In the latter case, we can define two important distances.

The apogee is the farthest point from the Earth within an elliptical orbit. On the contrary, the perigee is the nearest point (Fig. 3.1).
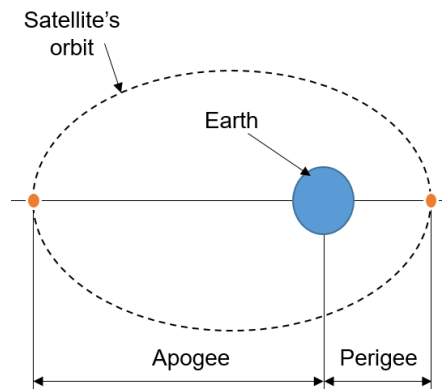
Figure 3.1: Elliptical orbit.

The study will focus on one of the most successful commercial space applications, communications satellites.

Such space vehicles are commonly located in geostationary orbits. They are circular orbits above the Earth's equator which has an orbital period equal to the Earth's rotational period (24 h). This is useful because ground antennas can be aimed at the satellite without their having to track the satellite's motion, which is relatively inexpensive.

However, after blasting off from Earth on a large rocket, communications satellites are usually released in temporary transfer elliptical parking orbits. Perigee can be anywhere above the dense atmosphere, but it is usually constrained to a few hundred kilometres above the surface. This is done to reduce launcher delta-V (Δv) requirements, and to limit the orbital lifetime of the boosters and parts not intended to stay in space, so as to cut down space junk. Δv is a measure of the total impulse that a rocket must provide to the spacecraft to perform a manoeuver.

Since satellites cannot be directly placed into their final orbits, geostationary transfer orbits (GTO) are typically employed. They are Earth orbits used to transfer a spacecraft to the geostationary orbit (GEO). Their apogee is at 35,786 km altitude (∼synchronous altitude) and, when the spacecraft reaches this point, its apogee kick motor is fired to increase the perigee altitude (see Fig. 3.2 (left)). After multiple firings, the vehicle reach GEO. If the firings are powerful enough, the transfer might be accomplished with two single burns, starting from a low Earth orbit, by means of the so-called Hohmann Transfer (see Fig. 3.2 (right)).
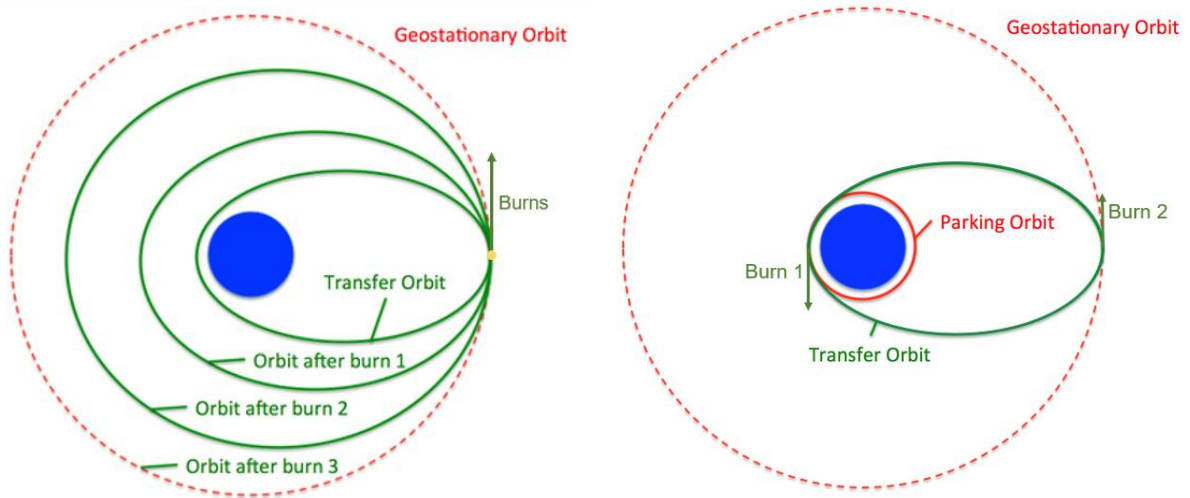
Figure 3.2: Typical chemical transfer (left) and Hohmann transfer (right) orbits [19]*.*

If low-thrust engines are used (e.g. electric propulsion), the transfer orbit usually employed is supersynchronous (SSTO). A SSTO is either an orbit with a period greater than that of a synchronous orbit, or just an orbit whose apogee is higher than that of a synchronous orbit. Typically, the satellite is injected into a SSTO orbit having the apogee above 42,164 km (synchronous radius) and then, it is thrusted continuously in the velocity vector direction at apogee (see Fig. 3.3). In this way, the vehicle raises the perigee and lowers the apogee each turn around the Earth.
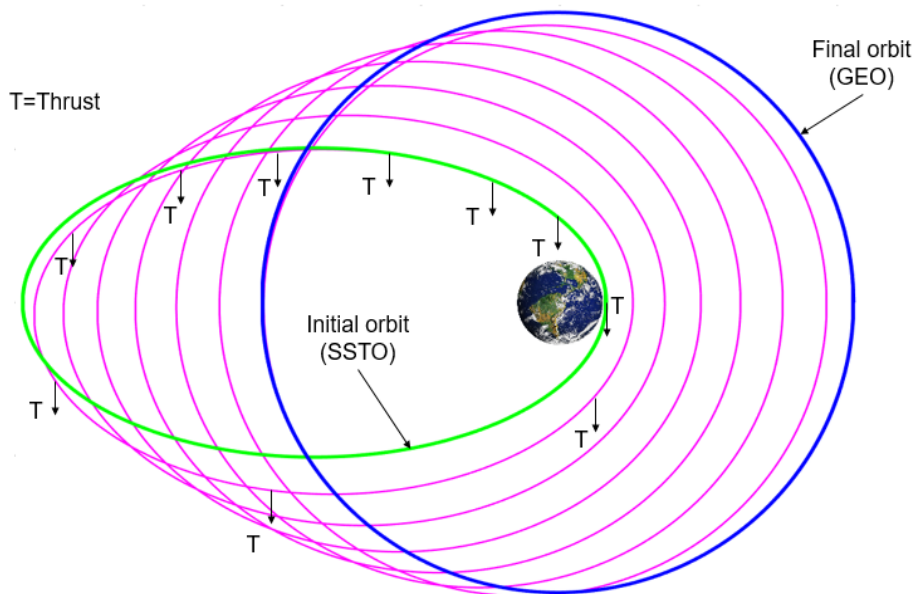
Figure 3.3: Orbit transfer schematic using electric propulsion.

We also find high thrust systems using SSTO because, in this way, orbital inclination can be changed more efficiently, since less Δv is required at higher altitudes, where orbital velocity is lower.

Finally, another low-thrust manoeuvre, also using electric propulsion, is the so-called spiral climb. It consists in a spiral trajectory around the Earth, starting from LEO and finishing in GEO. This is achieved by thrusting continuously in the direction of the spacecraft's velocity, always tangentially to the orbit (see Fig. 3.4).
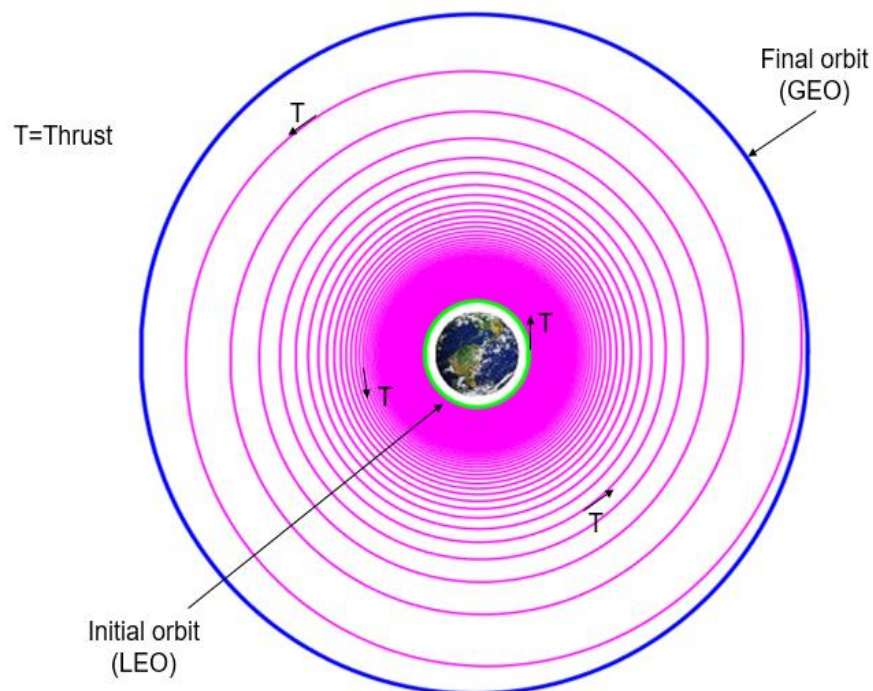
Figure 3.4: Electric propulsion transfer schematic from LEO to GEO.

In this section, a numerical comparison, between chemical and electric propulsion, will be performed in order to get a rough idea about the different benefits of each system. To that end, we will analyse three of the manoeuvres mentioned above. For electric propulsion, a transfer from SSTO to GEO (Fig. 3.3) and a transfer from LEO to GEO (Fig. 3.4) will be studied. These operations will be compared with a Hohmann transfer carried out by chemical engines. For all the missios, we will consider a final mass of the spacecraft (when placed on its destination orbit) around 2000 kg. This is the typical weight of a conventional communications satellite (without taking into account the propellant for orbit raising) [20].

For chemical and spiral climb missions, we will consider the same starting point, a circular low Earth orbit (LEO) at 300 km altitude.

For the sake of simplicity, we will not consider a plane change.

3.1.1. Chemical propulsion

Hohmann transfer is an elliptical transfer between two co-planar circular orbits. It is the most efficient planar manoeuvre (regarding Δv budget), and requires two impulses, Δv_1 and Δv_2.

First one is used to move onto the ellipse from LEO. Δv_1 is the difference between the velocity at the perigee of the ellipse and that of the circular orbit in the same point, as it is assumed an instantaneous impulse.

$$\Delta v_1 = v_1 - v_{c_1} = \sqrt{\frac{\mu}{r_1}} \left(\sqrt{\frac{2r_2}{r_1 + r_2}} - 1 \right) \tag{3.1}$$

Velocities are obtained from the total energy equation of the spacecraft (*Annex A.1*) [21].

The same procedure is followed to obtain Δv_2, which is the difference between the velocity at GEO and that of the apogee.

$$\Delta v_2 = v_{c_2} - v_2 = \sqrt{\frac{\mu}{r_2}} \left(1 - \sqrt{\frac{2r_1}{r_1 + r_2}} \right) \tag{3.2}$$

The process to obtain all the velocities is detailed in *Annex A.1* [21].

In Eqs. 3.1 and 3.2, r_1 and r_2 are respectively, the radius of LEO and GEO, and μ is the gravitational parameter of the Earth ($\mu = GM_E$).

$$r_1 = R_E + h_1 = 6378 + 300 = 6678 \; km$$

On the other hand, geostationary orbit implies that both, spacecraft and Earth (rotation), have equal angular velocities. If we take that into account, we can obtain the synchronous radius of the Earth (calculation detailed in *Annex A.1* [21]),

$$r_2 = 42241 \; km$$

Therefore, total Δv required for performing a Hohmann transfer is,

$$\Delta v_H = \Delta v_1 + \Delta v_2 \tag{3.3}$$

and using Eqs. 3.1, 3.2 and 3.3,

$$\Delta v_H = 3.900 \ km/s$$

Now, from the momentum conservation (*Annex B.1* [21]), we can obtain the Tsiolkovsky rocket equation,

$$\Delta v = I_{sp} g_0 \ln \frac{M_i}{M_f} \qquad (3.4)$$

where,

$$I_{sp} = u/g_0 \qquad (3.5)$$

Eq. 3.4 describes the motion of a vehicle that applies acceleration to itself by expelling part of its mass. The equation relates the Δv with the effective exhaust velocity (u) of the propellant and the initial (M_i) and final (M_f) mass of the spacecraft.

We should note that u is the exhaust velocity of the gases relative to the rocket.

Since gravity loses are not taken into account, the equation is applicable to orbital impulsive manoeuvres, in which the propellant is discharged and Δv is applied instantaneously. Moreover, burns are applied tangentially to Earth gravity field, so the assumption is reasonably accurate.

For this study, we are going to use the specific impulse of a bipropellant apogee engine typically employed in manoeuvres like that shown in Fig. 3.2 (left). (HiPAT™ 445 N dual mode high performance liquid apogee thruster). It is used to circularise a GTO orbit by running the engine in the apogee repeatedly. This motor would not be able to perform a Hohmann transfer with two impulses because it does not produce thrust enough, but it gives us a rough idea about the performance of chemical engines used for this purpose. It uses Hydrazine as propellant and nitrogen tetroxide (N_2O_4) as oxidiser, with an oxidiser/fuel ratio of 0.85 [22].
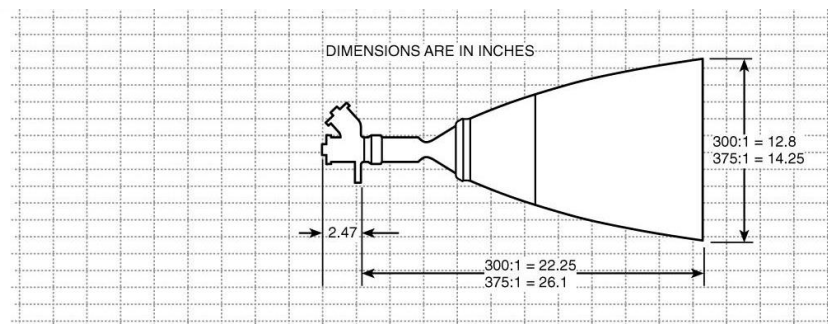
Figure 3.5: HiPAT 445 N thruster [22].

HiPAT^{TM} 445 N Dual Mode High Performance Liquid Apogee Thruster

Thrust [N]	445
Specific impulse [s]	329
Mass [kg]	5.4
Total pulses	672
Propellant	Hydrazine/NTO(MON-3)

Table 3.1: HiPAT thruster performance [22].

Using the I_{sp} from Table 3.1 and the required Δv for a Hohmann manoeuvre we can obtain the following mass ratio (R_m) from Eq. 3.4,

$$R_m = \frac{M_i}{M_f} = e^{\frac{\Delta v}{I_{sp}g_0}} = 3.348$$

Considering that typical satellites have a final mass around 2000 kg, the spacecraft mass at launch, without taking into account the launcher and its propellant, is 6696 kg. Therefore, we would need a mass of 4696 kg of fuel for the orbit-raising phase, 70% of the total initial mass.

The time employed to accomplish the transference is a half period of the transfer ellipse, which can be obtained by means of third Kepler's law,

$$\frac{4\pi^2}{T_H^2} a^3 = \mu \tag{3.6}$$

where a is the semi-major axis of the ellipse and is equal to $\frac{r_1+r_2}{2}$. Then, the time needed is,

$$t_H = \frac{T_H}{2} = \pi \sqrt{\frac{(r_1 + r_2)^3}{8\mu}} = 18982.42 \, s = 5.27h$$

3.1.2. Electric propulsion

As it has been said before, two missions will be studied to assess the electric propulsion system. To that end, we will make use of a Matlab® code (*Annex D.3* [21]) developed to solve

the differential equations governing the movement of a satellite around the Earth, without taking into account perturbations,

$$\frac{d^2\vec{r}}{dt^2} = -\frac{\mu}{r^3}\vec{r} + \vec{a}_T \tag{3.7}$$

As we can see, Eq. 3.7 is a nonlinear second order differential equation. It is a vector expression in a Cartesian coordinate system whose origin is the centre of the planet. The program, attached in *Annex D.3* [21], solves the system of equations by means of the fourth order Runge Kutta method. It is an iterative method to numerically approximate solutions of ODE's.

$\vec{r}$ is the position vector, and the term $\vec{a}_T$ corresponds to the acceleration provided by the thrust of the spacecraft. It is defined as follows,

$$\vec{a}_T = \frac{\vec{T}}{m} \tag{3.8}$$

where m is the mass of the spacecraft at each time (t), and it is defined in Eq. 3.9,

$$m = M_i - \dot{m}_p t \tag{3.9}$$

Here, $\dot{m}_p$ is the mass propellant flow rate, which is assumed to be constant over the whole trajectory.

As well as we have done for chemical propulsion, similar applications to the mission studied have been sought, in order to get a general idea about the typical parameters of the propulsion systems used in these manoeuvres. The spacecraft chosen for the comparison is the Eutelsat 115 West B satellite, which was the first one intended to use electric propulsion to fully positioning the vehicle into its orbit. It was launched in March 2015 and was equipped with the Boeing 702SP bus, which consists of four ion thrusters (XIPS) as propulsive system. Its transfer orbit was SSTO.

Figure 3.6: L-3 ETI XIPS thruster [13].

Eutelsat 115 West B	
Mass at launch [kg]	2205.0
Propulsion system	4 x XIPS
L-3 ETI XIPS (Orbit insertion mode)	
Thrust/engine [N]	0.165
Power required [W]	4500.0
Specific impulse [s]	3500
Propellant	Xenon

Table 3.2: Eutelsat 115 West B and L-3 ETI XIPS performance [23]*.*

As we can see, total force provided by the bus is,

$$T_T = 4 \cdot 0.165 = 0.660 \, N$$

and the total mass of the satellite before the transfer:

$$M_i = 2205.0 \, kg$$

Finally, making use of the thrust equation (Eq. 5.16), we can obtain the mass flow of a single engine,

$$\frac{T_T/4}{I_{sp} g_0} = \dot{m}_P = \frac{0.165}{3500 \cdot 9.81} = 4.80 \cdot 10^{-6} \frac{kg}{s}$$

Now that we have stablished the common parameters of both electrically propelled manoeuvers, let us define the particular specifications of each mission.

- Spiral climb transfer

As said before, the thrust will be always applied parallel to the velocity vector ($\vec{v}$). So,

$$\vec{a}_T = \frac{T_T}{m} \frac{\vec{v}}{|v|} \tag{3.10}$$

The initial conditions of the problem will be the same as for chemical propulsion. The satellite starts at LEO, thus

$$r_x(t = 0) = r_1 = 6678 \, km \qquad\qquad v_x(t = 0) = 0$$

$$r_y(t = 0) = 0 \qquad\qquad v_y(t = 0) = v_{c_1} = 7.743 \, km/s$$

v_{c_1} calculation is detailed in *Annex A.1* [21].

As additional information, Δv required for this manoeuvre is directly the difference between the initial and final orbit velocities [24]. Engines are continuously thrusting over the spiral and the orbit is nearly circular all the time.

$$\Delta v_e = v_{c_1} - v_{c_2} = 7.743 - 3.086 = 4.657 \frac{km}{s}$$

- Transfer from SSTO

In this case, the thrust must be applied in the opposite direction of the velocity vector in the perigee of the orbit over all the trajectory. Therefore,

$$\vec{a}_T = -\frac{T_T}{m}\vec{j} \qquad (3.11)$$

$\vec{j}$ denotes the y direction, supposing that the spacecraft begins at the x axes with its velocity vector parallel to $\vec{j}$ (Fig. 3.7).
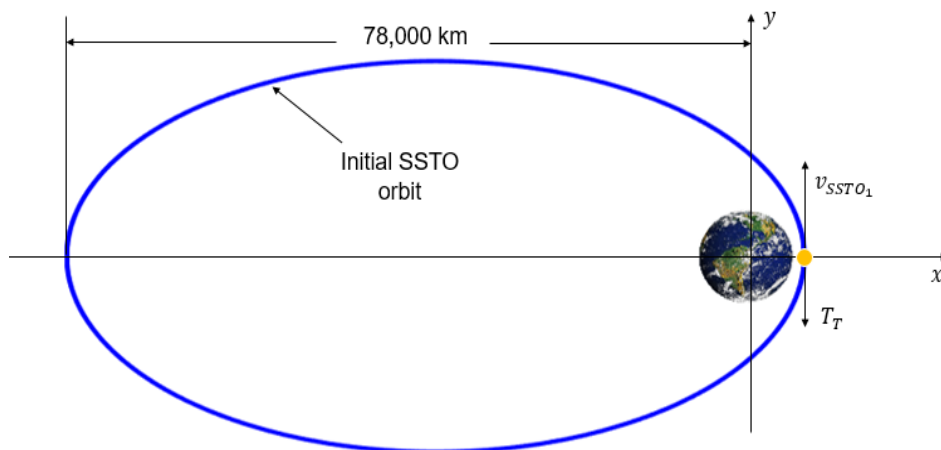
Figure 3.7: Transfer from SSTO mission initial conditions.

The initial conditions, in this case, are given by the launch vehicle, since we will analyse the particular mission of the Eutelsat 115 West B satellite. The initial transfer orbit is a highly elliptical trajectory with its apogee at a radius of 78,000 km and its perigee at 300 km altitude. Thus,

$$r_x(t = 0) = r_1 = 6678 \; km \qquad\qquad v_x(t = 0) = 0$$

$$r_y(t = 0) = 0 \qquad\qquad v_y(t = 0) = v_{SSTO_1} = 10.511 \; km/s$$

$v_y(t=0)$ is calculated from the energy equation of the spacecraft (Eq. A.2 from *Annex A.1* [21]), as well as it was made for v_{c_1}. In this case, though, r_2 would be 78,000 km and the semi-major axis of the ellipse should be recalculated.

Once we have defined our low-thrust missions' specifications, we can run the program. The code computes the time needed to finish the manoeuvres. We find out that our vehicle would reach GEO after,

Mission	*Spiral climb*	*Transfer from SSTO*
Time [months]	5.637	2.547

Table 3.3: Low thrust missions duration.

We can also get the propellant mass (M_{p_0}) needed to undertake the mission as,

$$M_{p_0} = 4 \cdot \dot{m}_p \cdot t \qquad (3.12)$$

Finally, the Δv provided by the thrusters over the transfer, can be computed using Eq. 3.4.

The following table comprises the missions' performance for both electric propelled missions.

Mission	*Spiral climb*	*Transfer from SSTO*
Time [months]	5.637	2.547
M_i *[kg]*	2205.0	2205.0
M_f *[kg]*	1924.1	2078.1
M_{p_0} *[kg]*	280.9	126.9
Δv *[km/s]*	4.678	2.035

Table 3.4: Low-thrust missions' performance

3.2. Results analysis

In the table below, the significant parameters of missions analysed in Section 3.1 are retrieved.

Parameter	Hohmann transfer	Spiral climb	Transfer from SSTO
Thrust [N]	445	0.660	0.660
I_{sp} [s]	329	3500	3500
M_i [kg]	6696.0	2205.0	2205.0
M_f [kg]	2000.0	1924.12	2078.09
M_{p_0} [kg]	4696.0	280.9	126.9
Δv [km/s]	3.9	4.678	2.035
Mission duration	5.27 h	5.637 months	2.547 months
Propellant	Hydrazine/NTO(MON-3)	Xenon	Xenon

Table 3.5: Summary of missions' performance.

From Table 3.5, we can draw several conclusions. First of all, there is a large difference between the amount of propellant employed by chemical and electric propulsion. The fuel mass of the chemical system suppose around 70 % of the total initial mass of the vehicle, whereas for the electric case, the propellant mass fractions are around 13 % and 6 %. It does not imply significant cost differences for the orbit raising manoeuver, since costs of xenon gas (∼1200 $/kg) [25] is much higher than hydrazine (∼17 $/kg) [26] and nitrogen tetroxide (N_2O_4) (∼6 $/kg) [26]. Nevertheless, it would result in substantial launch cost savings, since, as it has been said, placing a kilogram of anything into Earth orbit costs as much as 22,000 $ [7].

Therefore, considering that the launch vehicle places the spacecraft in the same orbit (LEO for chemical and spiral climb transfers), the launch cost savings would be,

$$cost\ savings = (4696 - 280.88)kg \cdot 22,000\ \$/kg = 97,132,640\ \$$$

This is a preliminary study and actual values could vary considerably. However, the analysis gives us a rough idea about the order of magnitude of the cost savings using electric propulsion.

Another important fact presented in Table 3.5 is the mission duration. Hohmann transfer is clearly the fastest one, (in the order of hours) although a real mission, carried out with the bipropellant engine considered, would perform a transfer like shown in Fig. 3.2 (left). In such case, the total time of the manoeuver would take some days or weeks, still faster than electrically propelled missions. On the other hand, if we compare both electric propulsion manoeuvers, we can see that, with the same thrust, and less than half of propellant mass, the transfer from SSTO takes 3.090 months less to reach GEO.

Finally, the Δv budgets are exposed. First of all, we must highlight that, for the spiral climb, the value matches to that given in Section 3.1.2 (Spiral climb transfer), which was calculated as the difference between initial and final velocity. Small differences may be due to the accuracy level of the numerical method employed to integrate the differential equations (Eq. 3.7).

We can see that, having the same departure orbit, Hohmann transfer is the most efficient one (regarding Δv budget).

With respect to the transfer from SSTO, Δv required is much lower. This is due to the fact that the launch vehicle place the spacecraft in a different initial orbit. Taking into account that all the vehicles (of the three missions) are released in the same point (LEO radius at 300 km altitude), the launch vehicle of the transfer from SSTO should provide an extra Δv of,

$$\Delta v_{extra} = v_{SSTO_1} - v_{c_1} = 10.511 - 7.743 = 2.768 \ km/s$$

We may conclude that there is a trade-off between costs and time. Electric propulsion is much cheaper than chemical one. However, the latter is quicker, and companies can meet their needs without waiting months. Within electric propulsion missions, transfer from SSTO seem to be the most suitable option, since it spends 2.2 times less time in placing the vehicles in their final orbit, and the propellant consumption is much lower. In exchange, spiral climb requires a minor launch vechicle's Δv budget.

Once we have demonstrated the usefulness of an electric propulsion system, we will conduct an accurate study about the working principle of an ion thruster, the most developed electric engine, up to this day. We will make use of the Brophy's theory to study the main parameters affecting the device's performance and optimise them.

Chapter 4.   Electromagnetism and plasma physics

Before starting with a detailed analysis of the ion thruster's working principle, it is worthwhile introducing the reader to the electromagnetic theory and its extension to plasma physics, since they are essential to understand the way in which electric propulsion devices work. Although magnetic forces are not responsible for the acceleration of particles in ion engines, we will see, later on, the importance of magnetic fields in such drives.

4.1.   Electromagnetic theory

Generally, we find four equations that describe how electric and magnetic fields behave in vacuum, the so-called Maxwell's Equations. All of them were synthesised from a set of five different laboratory experiments.

First experimental observation let to Coulomb's law,

$$\vec{F} = q\vec{E} = \frac{q^2}{4\pi\varepsilon_0|\vec{r}|^3}\vec{r} \qquad (4.1)$$

which expresses the force that an electrically charged particle feels when it is under the effect of an electric field. ε_0 is the vacuum permittivity, q is the charge of the particle.

Noting that,

$$\vec{E} = -\nabla\phi \qquad (4.2)$$

and

$$q = \int_V \rho dV \qquad (4.3)$$

where ϕ is the electric potential and $\rho \ [C/m^3]$ is a charge distribution, we obtain, after several rearrangements, Poisson's equation (first Maxwell's Equation),

$$\nabla^2 \phi = -\frac{\rho}{\varepsilon_0} = -\nabla \cdot \vec{E} \qquad (4.4)$$

Second experiment states the torque $(\vec{T})$ at which a magnetic dipole is subjected when a magnetic field $(\vec{B})$ is applied,

$$\vec{T} = \vec{m} \times \vec{B} \qquad (4.5)$$

Third observation stablishes that the divergence of a magnetic field is equal to zero, since no isolated magnetic charges have been found up to this day, and divergence represents the density of the outward flux of a vector field from an infinitesimal volume around a given point,

$$\nabla \cdot \vec{B} = 0 \qquad (4.6)$$

Fourth experiment states that an electric current induces a magnetic field,

$$\oint_C \vec{B} \cdot \vec{dl} = \mu_0 I \qquad (4.7)$$

which, using Stoke's theorem and considering that the current (I) arises from a distribution $(\vec{J})$, turns into,

$$\nabla \times \vec{B} = \mu_0 \vec{J} \qquad (4.8)$$

where μ_0 is the permeability in vacuum.

The fifth observation, unlike the previous ones, describes a non-static situation, where a relation between electric and magnetic fields is found (Faraday's law). A time change of magnetic flux induces an electric field,

$$\nabla \times \vec{E} = -\frac{\partial \vec{B}}{\partial t} \qquad (4.9)$$

In order to be consistent with conservation of charges, Eq. 4.7 must be modified by taking into account a change of the electric field with time,

$$\nabla \times \vec{B} = \mu_0 \vec{j} + \mu_0 \varepsilon_0 \frac{\partial \vec{E}}{\partial t} \tag{4.10}$$

Therefore, we have obtained the four Maxwell's Equations that explains electric and magnetic fields behaviour in vacuum. They are compiled down below:

$$\frac{\rho}{\varepsilon_0} = \nabla \cdot \vec{E} \qquad\qquad\qquad \nabla \times \vec{E} = -\frac{\partial \vec{B}}{\partial t}$$

$$\nabla \cdot \vec{B} = 0 \qquad\qquad\qquad \nabla \times \vec{B} = \mu_0 \vec{j} + \mu_0 \varepsilon_0 \frac{\partial \vec{E}}{\partial t}$$

Such equations should be modified if matter is involved, because atoms in materials react to applied electric and magnetic fields generating fields on their own, modifying the magnitude and direction of the former ones. Nevertheless, due to the low density of particles in the region of the thruster to be studied, the medium can be assumed vacuum.

4.2. Plasma physics

Plasma is one of the four fundamental states of matter. It is an electrically quasineutral medium of unbound positively charged ions, negatively charged electrons and neutral species. The overall charge of a plasma is roughly zero, that is, it is electrically neutral at macroscopic scale, although such neutrality is broken down when looked at atomic scale.

Hereafter, the effect of perturbing fields on plasmas is discussed. Two essential quantities can be derived when studying such perturbations: the Debye length and the plasma frequency.

By considering a 1D plasma and using the equations of Section 4.1, we can find a characteristic length of a plasma, Debye length (λ_D). To see the procedure followed to obtain this quantity, see [27],

$$\lambda_D = \sqrt{\frac{\varepsilon_0 k T_e}{e^2 n_e}} \tag{4.11}$$

where k is the Boltzmann constant, e is the electron charge, n_e the electron density and T_e the electron temperature.

Such length is an estimation of the size of the non-neutral regions in a plasma, and is of crucial importance when studying the effects of plasmas in contact with materials. For example, it gives us an idea of the thickness of the layer produced around a charged piece immersed in a plasma. We will discuss this issue in more detail in Section 4.2.2.

Another characteristic quantity of a plasma, mentioned above, is the plasma frequency (ω_p), which can be obtained from the equation of motion for electrons subjected to an electric field. To see the procedure followed to obtain this quantity, see [27],

$$\omega_p = \sqrt{\frac{e^2 n_e}{\varepsilon_0 m_e}} \qquad (4.12)$$

where m_e is the electron mass.

It represents the rate at which electrons oscillate about their equilibrium positions with respect to an immobile ion background. This frequency is important when talking about propagation of electromagnetic waves, since those with frequencies lower than ω_p will not propagate as their fields are shielded by the plasma.

4.2.1. Plasma particles motion under the effect of electromagnetic fields

Plasmas are very dynamic conductive media that respond to electric and magnetic fields. As it is known, when a charged particle moves within a magnetic field, it generates an electric current. In plasma, the movement of a charged particle affects and is affected by the general field created by the movement of other charges. Because of that, an in-depth study of the plasma dynamics becomes too complex. Fortunately, if plasmas are dilute enough, charged particles behaviour is nearly independent of each other, allowing a simpler description of the motion of the particles.

Lorentz force is a combination of electric and magnetic forces on a point charge due to electromagnetic fields, and it determines the motion of charged particles in a plasma. If a particle of charge q moves with velocity v in the presence of an electric field E and a magnetic field B, then it will experience a force,

$$\vec{F_L} = m_i \frac{d\vec{v}}{dt} = q(\vec{E} + \vec{v} \times \vec{B}) \qquad (4.13)$$

where m_i is the particle mass.

From the latest equation, and assuming $E = 0$, it is possible to integrate twice the expression and obtain both the velocity and position vectors (planar motion (2D)),

$$v_x = \frac{q}{|q|} v_n \sin(\omega_C t + \varphi) \qquad\qquad v_y = -\frac{q}{|q|} v_n \cos(\omega_C t + \varphi) \qquad (4.14)$$

$$x = \frac{v_n}{\omega_C} \cos(\omega_C t + \varphi) \qquad\qquad y = \frac{v_n}{\omega_C} \sin(\omega_C t + \varphi) \qquad (4.15)$$

We can see that the particle performs a circular motion around the magnetic field, with a constant velocity of v_n and a gyration rate,

$$\omega_C = \frac{qB}{m_i} \qquad (4.16)$$

the so-called cyclotron frequency.

Eq. 4.16 can be also easily inferred from Fig. 4.1, by means of a forces equilibrium.
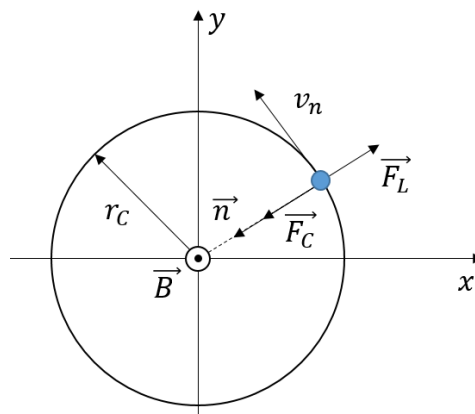
Figure 4.1: Motion of a charged particle within a magnetic field diagram.

If we consider that Lorentz force (Eq. 4.13) equals the centripetal force, we have,

$$-q \, \overrightarrow{v_n} \times \vec{B} = m_i \frac{v_n^2}{r_C} \vec{n} \qquad \rightarrow \qquad qB = m_i \frac{v_n}{r_C}$$

where r_C is the gyration radius, also known as the Larmor radius, and it is defined as,

$$r_C = \frac{v_n}{\omega_C} = \frac{m_i v_n}{qB} \tag{4.17}$$

Hence, we obtain again Eq. 4.16,

$$\omega_C = \frac{qB}{m_i}$$

If an E (constant) is added, the solution turns out to be as follows:

$$v = v_n e^{-i\omega_c t} - i\frac{E}{B} \tag{4.18}$$

Therefore, we still have the same homogeneous part ($v_n e^{-i\omega_c t}$, which is the same as Eqs. 4.14 and 4.15), but we add a particular solution $\left(-i\frac{E}{B}\right)$. It is noteworthy to highlight that the final solution is a cycloid, in which the Larmor motion is superimposed to a drift in the same direction as $\vec{E} \times \vec{B}$.

The motion of charged particles under the effect of electromagnetic fields is of crucial importance when determining ion thruster's performance. The need of a magnetic field lays in the fact that, for example, it modifies the electron containment length within the discharge chamber of the ion thruster. This and other issues, regarding electromagnetic fields in the thruster, shall be discussed further on.

4.2.2. The plasma boundary: the sheath

The sheath analysis is a critical point within the study of ionised gases, since it determines the plasma's overall behaviour inside its boundaries.

Let us see how the plasma sheath is generated.

When the plasma is first ignited, ions and electrons hit the walls of the device and are lost. Because electrons have much higher thermal velocities than ions, they will make more collisions with the wall and be lost faster while the wall is at plasma potential (ϕ_P). Due to the higher mobility of the electrons, at the beginning, there is a net electron current to the chamber walls. Over time, this leaves the plasma bulk with a net positive charge and, therefore, the potential of the walls becomes negative with respect to the plasma. This potential difference

cause that all ions directed towards the wall fall on it, whereas electrons are reflected. The repulsion of electrons results in the formation of a positive space-charge region (sheath) shielding the neutral plasma from the negative wall. The equilibrium potential drop $(-\phi_w)$ is that required to equalise electron and ion losses. Thanks to the shielding that occurs, over distances greater than the Debye length, the bulk of the plasma will be at a roughly constant potential (ϕ_P).
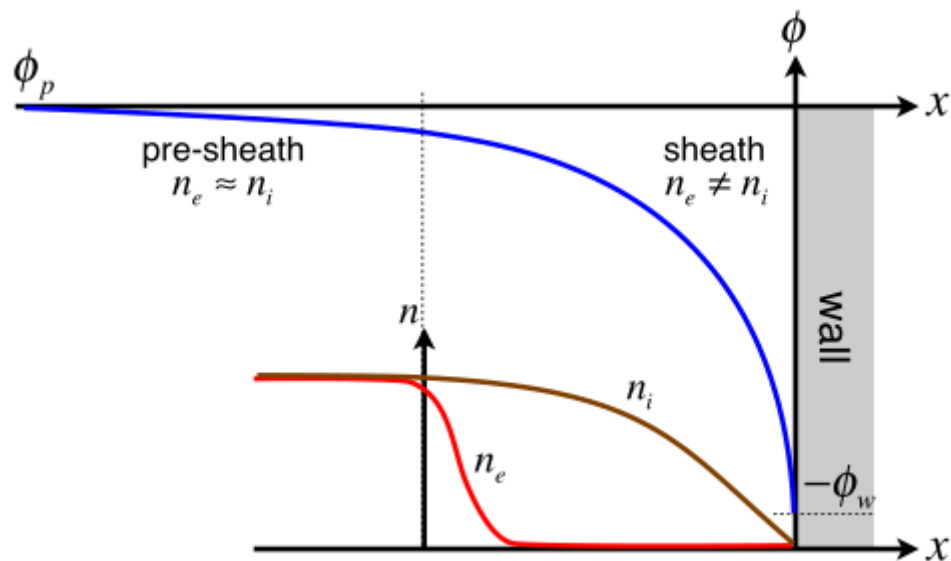
Figure 4.2: Potential and plasma distribution near the material wall.

The sheath extension is given by the Debye length (λ_D), introduced before in Eq. 4.11.

However, to reach the equilibrium point, ions must enter the sheath region with a specific high velocity, and so, they must be accelerated by an electric field. This is achieved by means of a small potential drop in the pre-sheath (see Fig. 4.2), which is the region that spreads some Debye lengths beyond the sheath. It is a quasi-neutral region.

This study will be aimed to analyse the structure of the non-neutral layer adjacent to materials in contact with the plasma (sheath).

To that end, we will make use of the continuity statement for ion and electron currents, which must be the same when the equilibrium wall potential is achieved. Ion and electron current densities are respectively given by,

$$j_i = e n_i v_i \tag{4.19}$$

and

$$j_e = -\frac{e n_{e_w} v_e}{4} \tag{4.20}$$

In Eq. 4.20, n_{e_w} is the electron number density adjacent to the wall. The electron distribution near the wall is assumed Maxwellian and, therefore, we can use the Boltzmann equilibrium relation in order to determine their population.

$$n_{e_w} = n_{e_\infty} e^{\left(-\frac{e\phi_w}{kT_e}\right)} \tag{4.21}$$

Where n_{e_∞} is the electron density far away from the wall and k is the Boltzmann constant. T_e is the temperature of the electrons.

On the other hand, v_e is the mean electron thermal speed, which is given by,

$$v_e = \sqrt{\frac{8kT_e}{\pi m_e}} \tag{4.22}$$

Now, the ion current density must be calculated, and it will be evaluated in the limit of the pre-sheath. At such point, $n_i = n_e$, hence, we can use the Boltzmann relation for electrons, but this time in the pre-sheath, characterised by the potential (ϕ_{ps})

$$n_i = n_e = n_{e_\infty} e^{\left(-\frac{e\phi_{ps}}{kT_e}\right)} \tag{4.23}$$

To obtain the ions velocity at the pre-sheath, the momentum equations of ions and electrons must be formulated in such point.

$$n_i m_i V_i \frac{dV_i}{dx} + \frac{dP_i}{dx} = e n_i E_x - F_i \tag{4.24}$$

$$n_e m_e V_e \frac{dV_e}{dx} + \frac{dP_e}{dx} = -e n_e E_x - F_e \tag{4.25}$$

Where F_i and F_e are frictional forces due to collisions and, P_i and P_e, are pressures. Making use of $P = nkT$ and $\Gamma_i = n_i v_i = ct$, we get,

$$\frac{d}{dx}\left(m_i\Gamma_iv_i + kT_e\frac{\Gamma_i}{v_i}\right) = -F_i - F_e \qquad (4.26)$$

We should note that, the sum between parentheses is minimum for the so-called Bohm velocity,

$$v_{i_{x=\lambda_D}} = v_B = \sqrt{\frac{kT_e}{m_i}} \qquad (4.27)$$

This is a similar concept to that of speed of sound, for plasmas (see Fig. 4.3).
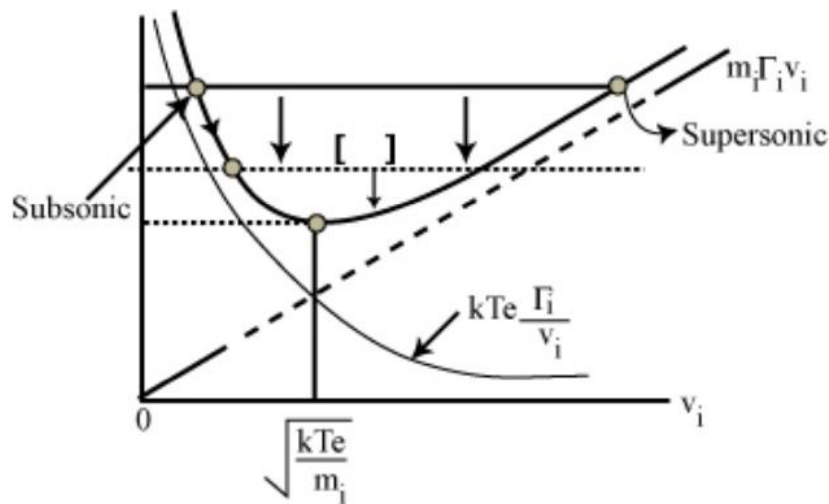
Figure 4.3: Bohm velocity illustration.

Therefore, ions will accelerate to $v_i = v_B$, the velocity at which they will enter the plasma sheath.

Returning to Eq. 4.23, and using the mean thermal energy expression,

$$e\phi_{ps} = \frac{1}{2}m_iv_B^2 \qquad (4.28)$$

We get,

$$n_{i_{x=\lambda_D}} = n_{e_\infty}e^{-1/2} \qquad (4.29)$$

Using Eqs. 4.19 to 4.22, 4.27 and 4.29, we can finally equalise both current densities $(j_i = j_e)$,

$$en_{e_\infty} e^{-1/2} \sqrt{\frac{kT_e}{m_i}} = e\frac{n_{e_\infty}}{4} \sqrt{\frac{8kT_e}{\pi m_e}} e^{(-\frac{e\phi_w}{kT_e})}$$

And sheath potential is approximated by,

$$\phi_w \approx \frac{kT_e}{e} ln\sqrt{\frac{m_i}{m_e}} \qquad (4.30)$$

As a summary, walls in contact with plasmas become negatively charged, producing a shield (with a characteristic Debye length) which confine electrons and let the ions fall to the walls with a velocity of the order of the Bohm velocity.

As we will see later on, the sheaths are of crucial importance for the operation of ion thrusters, since they determine the extracting capabilities of the device and the efficiency of their ionisation chamber.

Chapter 5.   Ion thruster: preliminary analysis

Now that we have a rough idea about how plasmas behave in vacuum and how they interact with electromagnetic fields, we can study in detail how an ion thruster uses the propellant gas to generate a thrust.

The ion engine is a simple device in concept. It accelerates heavy positive ions through a strong electric field placed between two grids that work as electrodes. Such particles leave the engine as a high-velocity exhaust stream, producing a relatively low thrust and a high I_{sp}. Before that, propellant must be ionised.
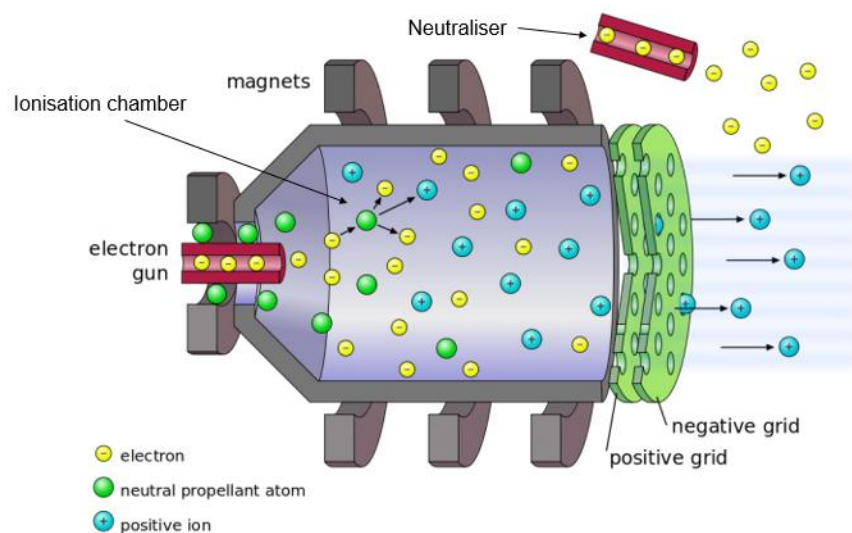
Figure 5.1: Electron bombardment ion thruster schematic [9]*.*

The main functional elements in an ion thruster are listed below:

- Ionisation chamber
- Grids
- Neutraliser
- Power supplies

The power supplies are the most important elements regarding mass and parts amount. They affect largely the final weight of the power plant. Grids are essential elements too, since

extraction capabilities depend on them and erosion due to ion impacts conditions their operation. Finally, another critical part of these devices is the ionisation chamber, whose characteristics control the losses and, therefore, the efficiency of the thruster. It can operate on a variety of principles, so we can distinguish several types of ion thrusters depending on the ionisation method employed.

5.1. Types of ion thrusters

As said above, there are different ion thrusters depending on the ionisation method employed. The most commonly used are:

5.1.1.   Electron bombardment thruster

In an electron bombardment thruster (Fig. 5.1), a gas propellant enters a discharge chamber at a controlled rate. A hot, hollow cathode (negative electrode) at the centre of the chamber emits electrons, which are attracted to a cylindrical anode (positive electrode) around the walls of the chamber. Some of the electrons collide with and ionise atoms of the propellant, creating positively charged ions. These ions are then drawn toward the grids to be accelerated.

5.1.2.   Radio-frequency ionisation thruster

Radio Frequency Ion thrusters are operated without any hot cathode inside the thruster's ionisation unit. Instead, the propellant is ionised by electromagnetic fields. For that, the ioniser chamber, which is made of an isolating material, is surrounded by a radio frequency coil. The coil induces an axial magnetic field. Finally, the primary magnetic field induces a secondary circular electric field in which free electrons gain the energy for impact ionisation.

5.1.3.   Contact ionisation thruster

In this type, ions are produced on a heated surface. Then, they are accelerated in an electric field. It has been one of the most intensively studied over the past 40 years. Nevertheless, it is of little use for space applications. A primary reason is that only Cesium has been shown to work with this method because of its electronic configuration, and due to its high corrosiveness, this propellant is not suitable for operate over long periods of time, so this model has been largely abandoned.

5.1.4. Electron Cyclotron Resonance (ECR) Microwave discharge ion thruster

In this thruster, plasma is produced by ionising propellant with high-energy electrons accelerated with ECR phenomenon using microwaves in a magnetic field formed by permanent magnets. Since the thruster utilises no cathode for plasma production, it is relieved from the cathode heater failures that result from the degradation of the cathodes, allowing longer lifetimes. That, in addition to its reliability because of its simple architecture and reduced number of components, are the major advantages of this ion drive. However, no much space flight experience has been gained and different limitations constrict its performance. For example, microwave power is physically limited because a plasma density that would exceed the cut off density would result in the microwaves to be reflected, thus not delivering power to the resonance region, impeding in this way the scalability of the thruster. Moreover, electric efficiency is low because of a weak coupling between plasma and microwaves.

The present document will focus on the electron bombardment type, also known as Kaufman ion engine. It is the most developed one and the best known. Furthermore, a great deal of experimental data has been reported, since ground and space flight tests have been performed since it was conceived and manufactured for the first time, five decades ago. A detailed explanation of this thruster (components, principles of operation, etc.) will be provided in the next section.

5.2. Electron bombardment ion engine

This engine consists of a cylindrical structure delimited by a set of two (or three, depending on the thruster) precisely placed grids at the end side. Such grids have a matrix of tailored holes in order to suitably extract the ion beam. The first grid is called screen grid, whereas the second one is referred to as the accelerator grid. When a third grid is used, it is known as decelerator grid. The other side of the cylinder is bounded by a flat plate. The volume delimited by this structure (cylinder, grids and flat plate) is referred to as the discharge chamber or ionisation chamber (see Fig. 5.2).
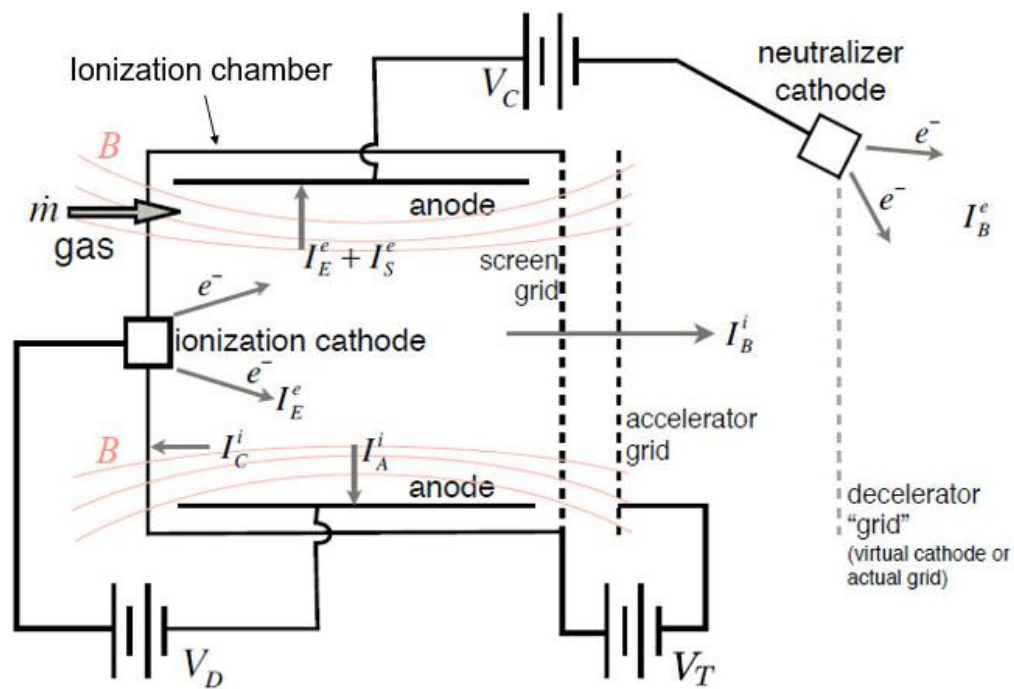
Figure 5.2: Ion thruster schematic [16]*.*

Propellant is injected into this chamber as a neutral gas. Coupled to the flat plate mentioned above, there is the cathode through which energised electrons are emitted. Such electrons are responsible for ionising the atoms of the gas contained in the ionisation chamber by colliding with them. The negative particles are accelerated by an electric field adjacent to the cathode, which is stablished by settling the chamber walls (anode) at some voltage above that of the cathode by means of a power supply.

The ions produced are then accelerated by a potential difference between the perforated plates, which define the exhaust velocity of these particles. Due to the sheath created in the screen grid's surface (as explained in Section 4.2.2), electrons are kept inside the ionisation volume, so they are collected by the anode and extracted in order to prevent negative charging of the spacecraft. For the purpose of increasing the probability of impact between electrons and propellant atoms before these are lost to the anode, a magnetic field is employed. After being collected, electrons are ejected by means of the neutraliser (electron-emitting device) to join the ions downstream and neutralise (but not recombine) the beam. The momentum exchanged between the ion beam and spacecraft constitutes the thrust of the device. Electrons ejected are not taken into account in the computation of the thrust since their momentum is some orders of magnitude below than that of the ions.

Now that we have a rough idea about the operation of an electron bombardment ion thruster, we can analyse exhaustively the different sections of the device that determine the performance of the device.

There are two imperative stages in which we will divide this analysis, ion extraction and acceleration system, on the one hand, and ionisation chamber operation, on the other hand.

5.2.1. Ion extraction and acceleration system

The main functional elements of this stage are the grids. As well as it was stated before, they are responsible for the extraction capabilities of the device, so they largely determine the thrust and exhaust velocity limits.

The grids are perforated plates whose size and number of wholes depend on the scale of the thruster, although typically, they are constituted by a set of hundreds to thousands holes, resulting in the same number of ion beamlets. Nevertheless, there are several parameters that can be optimised and are quite independent of the total diameter of the total exhaust area. Here below, it can be seen a schematic figure about the two grids layout.
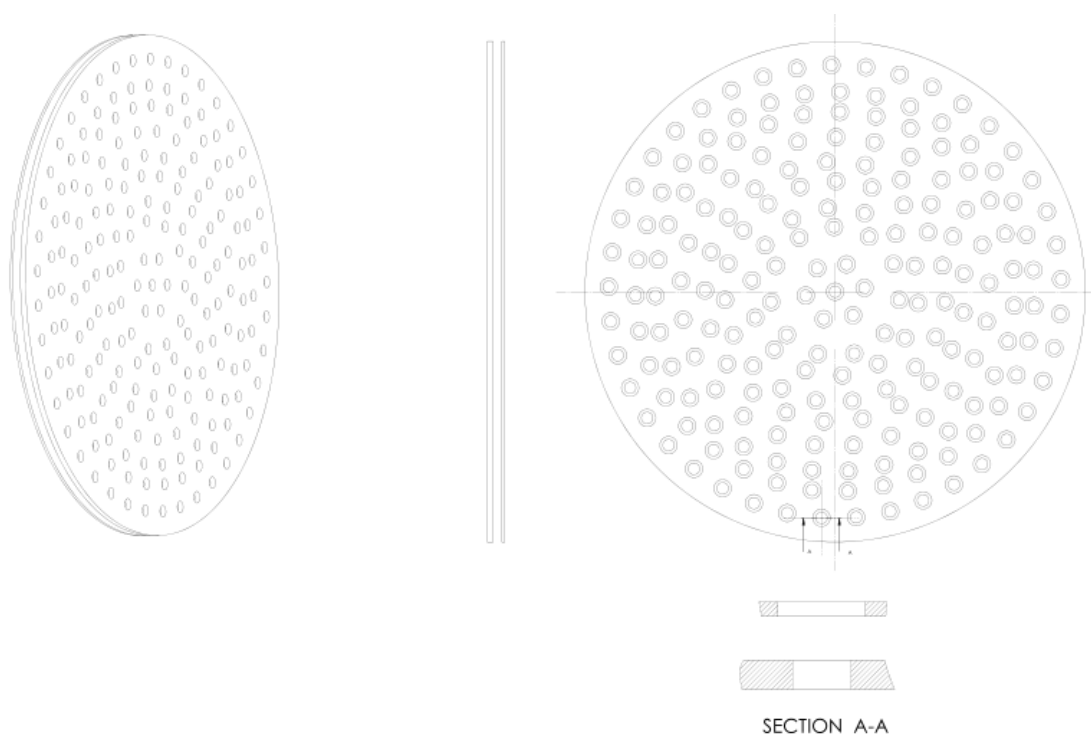
SECTION A-A

Figure 5.3: Grids schematic.

In Fig. 5.4 (as well as in section A-A of Fig. 5.3), we can see depicted the region around an aligned pair of screen and accelerator holes.
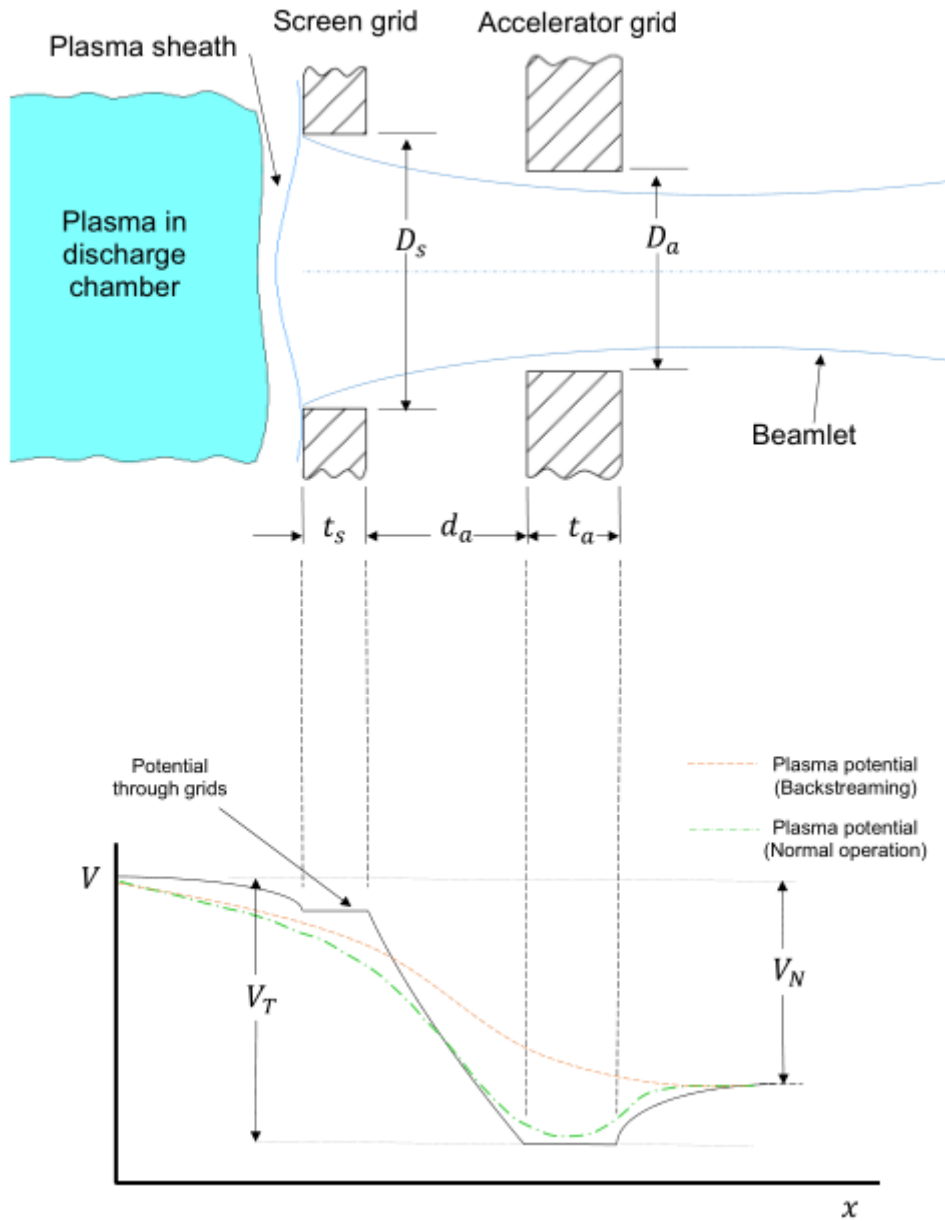
Figure 5.4: Aligned pair of holes schematic and potential through them.

Let us analyse the potential diagram shown in Fig 5.4. First of all, as a reference, in $x = 0$, the potential is that of the plasma, which is near that of the anode in the chamber. The screen, however, is at somewhat lower potential, near that of the cathode. Hence, ions fall through the accelerating potential when wandering in the proximity of the grid. This occurs due to a sheath creation in the plasma-grid contact region, as explained in Section 4.2.2. That shielding is also

responsible for keep electrons inside the ionisation chamber. Recall that ions enter the sheath at the Bohm velocity (Eq. 4.27).

Once ions are inside the region between the two grids, they are accelerated. Their final velocity will be defined by V_N (Net voltage), which is the difference between plasma and neutraliser potentials. V_T (Total voltage) is the difference between plasma and accelerator grid potentials, and it can be defined the ratio $R = V_N/V_T$, which will be fundamental when computing the extraction capacity of the system. It is important to note that, the exhaust velocity, can be maintained constant by fixing V_N, which is mainly determined by the neutraliser potential, which is, in turn, determined by the electrons flux, whose current charge must equal that of the ion stream. At the same time, V_T can be modified and, therefore, R too, in order to optimise the operation. When a third grid is used, it is set at neutraliser potential.

Apart from this, the potential through the holes has been represented in Fig. 5.4, which is the one that an ion would feel following the accelerating path. With green colour, it is shown the shape of such function when working in a normal way, that is, with an $R < 1$. On the other hand, the orange curve is given for a $R = 1$, resulting in a positive field in that region, which would derive in a backstreaming of the electrons ejected by the neutraliser. It is noteworthy to highlight that, for normal operation, the electric field is negative before leaving the last grid. In this way, electrons are rejected and do not go back into the ionisation chamber.

5.2.1.1. Child-Langmuir equation

The qualitative explanation given in the last section can be analysed by means of a set of equations governing the plasma's behaviour. However, due to the complexity of the potential and flow structures, it would be cumbersome to perform a three-dimensional study. Therefore, an idealisation of the problem will be made by considering the multiple beamlets as a single one.

The result of such derivation is known as Child-Langmuir space charge limited current equation, and it makes use of a one-dimensional model.

This model is valid to predict the value of the potential distribution ant current between the two grids, so it does not take into account the plasma sheath potential or the downstream conditions after the last grid.

The basic equations employed are:

- Poisson's equation (derived in Section 4.1)

$$\nabla^2 \phi = \frac{d\phi^2}{dx^2} = -\frac{\rho}{\varepsilon_0}$$

(5.1)

where $\rho = en_i$

- Ion continuity over the gap (between grids)

$$j_i = en_i v_i$$

(5.2)

Ions velocity (v_i) can be obtained as a function of the potential from a balance of forces inside the gap region. We only consider electrostatic forces:
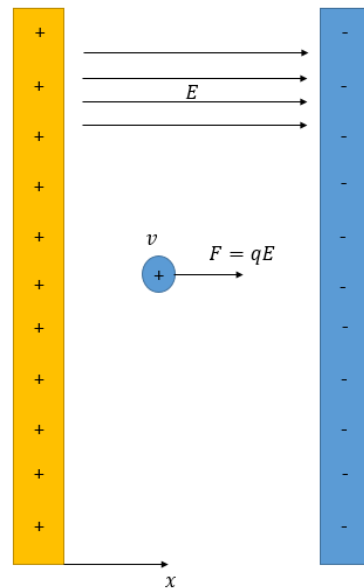
Figure 5.5: Accelerating field between two plates.

$$F = qE = -e\frac{d\phi}{dx} = m_i \frac{dv}{dt}$$

(5.3)

If we multiply both sides of Eq. 5.3 by dx, we get,

$$-e\frac{d\phi}{dx}dx = m_i \frac{dv}{dt}dx \qquad \rightarrow \qquad -ed\phi = m_i v dv$$

(5.4)

Integrating Eq. 5.4,

$$e\phi + \frac{1}{2}\, m_i v^2 = ct = e\phi_0 + \frac{1}{2}\, m_i {v_0}^2 \tag{5.5}$$

Finally,

$$v_i{}^2 - v_0{}^2 = \frac{2e(\phi_0 - \phi)}{m_i} \tag{5.6}$$

By assuming $v_0 = 0$,

$$v_i = \sqrt{\frac{2e(\phi_0 - \phi)}{m_i}} \tag{5.7}$$

Combining Eqs. 5.1, 5.2 and 5.7 we obtain a second order, nonlinear differential equation,

$$\frac{d^2\phi}{dx^2} + \frac{j_i}{\varepsilon_0}\sqrt{\frac{m_i}{2e(\phi_0 - \phi)}} = 0 \tag{5.8}$$

It can be integrated to yield

$$\left(\frac{d\phi}{dx}\right)^2 - \left(\frac{d\phi}{dx}\right)_0^2 = \frac{4j_i}{\varepsilon_0}\sqrt{\frac{m_i(\phi_0 - \phi)}{2e}} \tag{5.9}$$

We have obtained an expression for the electric field along the gap at any point where the potential is known. Now we can introduce the following boundary condition,

$$\left(\frac{d\phi}{dx}\right)_{x=0} = 0 \tag{5.10}$$

This assumption comes from the space charge limit condition, which gives the name to this model. This is the main limitation of the thruster and it is related with the maximum extraction capacity of the grids.

In the absence of ions, the electric field between the grids is constant, and only depends on the potential difference and separation between the electrodes. Once the thruster is operative and ions are introduced, they modify such field. In fact, first grid is partially shielded like it was explained in Section 4.2.2. The degree at which the field is altered is a function of the number of ions in the beam (mass flow rate). Therefore, there is a point when the accelerating field at the first grid drops to zero, being cancelled by the downstream positively charged ions. At this

point, the grids are extracting the maximum ion current possible (maximum flow rate) and we are space charge limited (it would be ideal to work at this regime). It should be noted that exhaust velocity is not limited by this phenomenon, since it only depends on the potential difference between the grids, as it can be seen in Eq. 5.7.

So, considering the optimum point of operation, the electric field becomes,

$$E = \left(\frac{4j_i}{\varepsilon_0}\right)^{\frac{1}{2}} \left(\frac{m_i(\phi_0 - \phi)}{2e}\right)^{\frac{1}{4}} \tag{5.11}$$

Integrating, again, the last expression, we arrive to,

$$\phi = \phi_0 - \left[\frac{3}{2}\left(\frac{j_i}{\varepsilon_0}\right)^{\frac{1}{2}}\left(\frac{m_i}{2e}\right)^{\frac{1}{4}} x\right]^{\frac{4}{3}} \tag{5.12}$$

The last expression determines the potential at any point in the gap as a function of the current density. Introducing the boundary conditions,

$$\phi_{x=0} = \phi_0 = 0 \qquad\qquad \phi_{x=d_a} = -V_T$$

and substituting it into Eq.5.12, we can find the value of the maximum current density j_i for a given potential difference V_T,

$$j_i = \frac{4}{9}\varepsilon_0 \sqrt{\frac{2e}{m_i}} \frac{V_T^{\frac{3}{2}}}{d_a^2} \tag{5.13}$$

Rearranging Eqs. 5.11 and 5.12, introducing 5.13, yields to the voltage and electric field profiles between the grids,

$$\phi(x) = -V_T \left(\frac{x}{d_a}\right)^{\frac{4}{3}} \tag{5.14}$$

$$E(x) = \frac{4}{3}\frac{V_T}{d_a}\left(\frac{x}{d_a}\right)^{\frac{1}{3}} \tag{5.15}$$

Eqs. 5.14 and 5.15 are represented below.
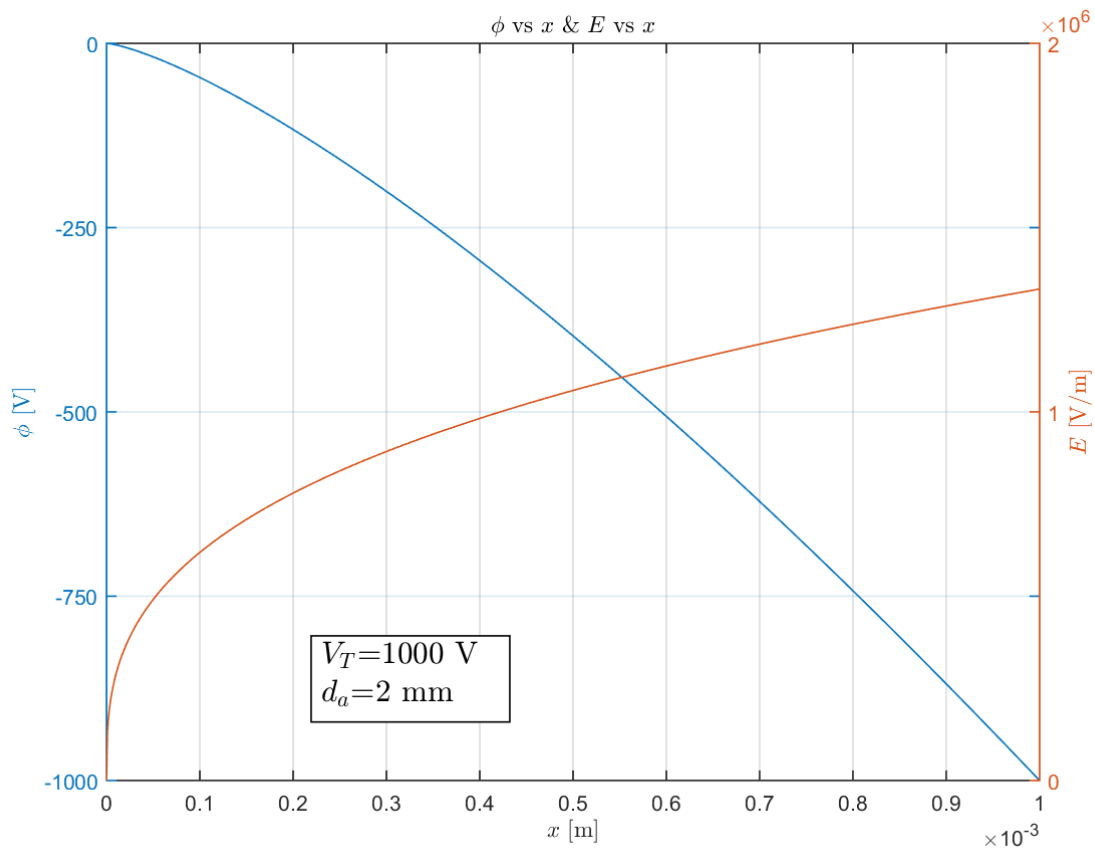
Figure 5.6: Electric field and potential in space charge limit condition.

As we can see in Fig. 5.6, the electric field is zero at $x = 0$ (space charge limit). After that, it is positive, making possible the acceleration of the ions. On the other hand, the potential decreases from 0 to -1000, being the latter the total voltage assumed to generate the curves.

Given Eq. 5.13, the thrust provided by the thruster may be computed, using the classical rocket thrust equation. As in chemical thrusters, the force per unit area is

$$\frac{T}{A} = \frac{\dot{m}}{A} u \tag{5.16}$$

Where the mass flow rate $(\dot{m})$ is related to the current by,

$$\dot{m} = j_i A \frac{m_i}{e} \tag{5.17}$$

and exhaust velocity is given by (using thermal energy equation),

$$u = \sqrt{\frac{2eV_T}{m_i}} \tag{5.18}$$

Therefore,

$$\frac{T}{A} = j_i \frac{m_i}{e} \sqrt{\frac{2eV_T}{m_i}} \tag{5.19}$$

And substituting j_i from Eq. 5.13,

$$\frac{T}{A} = \frac{8}{9} \varepsilon_0 \left(\frac{V_T}{d_a}\right)^2 \tag{5.20}$$

This thrust per unit area as a function of $\frac{V_T}{d_a}$ is shown in Fig. 5.7.
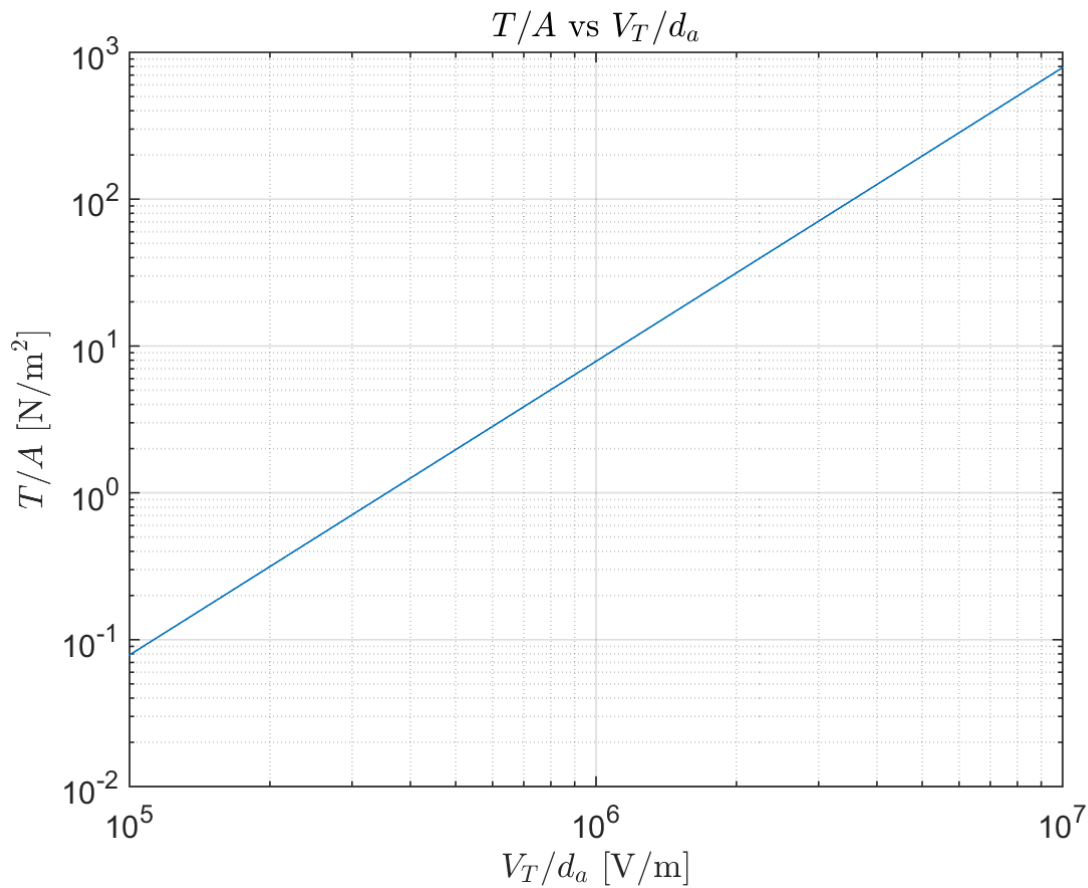
Figure 5.7: Thrust per unit area as a function of V_T/d_a.

Analysing the results obtained, one can realise that the current density (j_i), and therefore the thrust, can be increased by increasing the total voltage V_T or decreasing the gap distance d, so, increasing the electric field. The problem is that these parameters cannot be modified indefinitely. The electric field is mechanically limited since warping or irregularities during the construction of the grids exist, which could cause a breakdown or shorting between them, due to field concentrations. So typical maximum values are of the order of 10^6 V/m [16]. Electrical breakdown is a long reduction in the resistance of an insulator, (vacuum in our case) when the voltage applied across it exceeds the breakdown voltage. This results in the insulator becoming electrically conductive.

5.2.1.2. Decelerator grid

Now, we are going to analyse which would be the effect of considering a third decelerating grid.

First of all, it consists of a third electrode downstream of the second grid, at a somewhat higher potential. Therefore, after leaving the second electrode, the ions are decelerated to a lower exhaust velocity.

Regarding the lower velocity, for the typical current missions, not too large exhaust velocities are required in order to be optimal. So slowing the ions down would improve the overall efficiency of the thruster (as we will see in Chapter 9). It must be said that, the loss of thrust, resulting from the speed reduction, is outweighed by the benefit on the performance. That is, for a given energy cost, this system produces a higher thrust than the conventional.

Another question involved is the backstreaming problem, mentioned before. The third grid forces the electrons ejected by the neutraliser to get away from the grids. Otherwise, they would be accelerated backwards toward the ion source, damaging it.

It should be noted that the ion current remains constant by adding a third grid. For usual configurations, the screen-accelerator gap (d_a) still controls the ion current because the mean ion velocity is high in the second gap, and so, the mean ion density is low. In this way, electrostatic choking does not occur. However, this applies provided that following condition is fulfilled [28],

$$\frac{d_d}{d_a} < \left(1 - R^{1/2}\right)^{1/2}\left(1 + 2R^{1/2}\right) \tag{5.21}$$

Eq. 5.21 can be obtained by assuming that the divergence of the potential is zero in the last grid, as it is schematically shown in Fig. 5.8.

$$\left(\frac{d\phi}{dx}\right)_{x=d_a+d_d} = 0 \tag{5.22}$$

If condition in Eq. 5.22 is given, Eq. 5.21 becomes an equality and we are in the limit where the screen-accelerator gap still controls the ion current and, therefore, the mass flux passing through the grids.
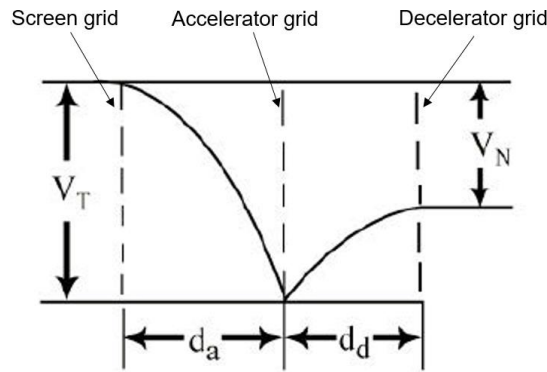
Figure 5.8: Accelerating and decelerating potentials through the grids [16].

Assuming that Eq. 5.21 is met, the role of the decelerator grid can be incorporated in the model by only considering that now, the exhaust velocity depends on V_N and not on V_T.

$$u = \sqrt{\frac{2eV_N}{m_i}} \tag{5.23}$$

The gap distance, on the other hand, is still d_a, the distance between the two first grids. Hence, thrust density can be rewritten as

$$\frac{T}{A} = \frac{8}{9}\varepsilon_0 \frac{V_T^{3/2}V_N^{1/2}}{d_a^2} = \frac{8}{9}\varepsilon_0 \left(\frac{V_T}{d_a}\right)^2 R^{1/2} = \frac{8}{9}\varepsilon_0 \left(\frac{V_N}{d_a}\right)^2 R^{-3/2} \tag{5.24}$$

A comparison between Eqs. 5.20 and 5.24 is done in Fig. 5.9.
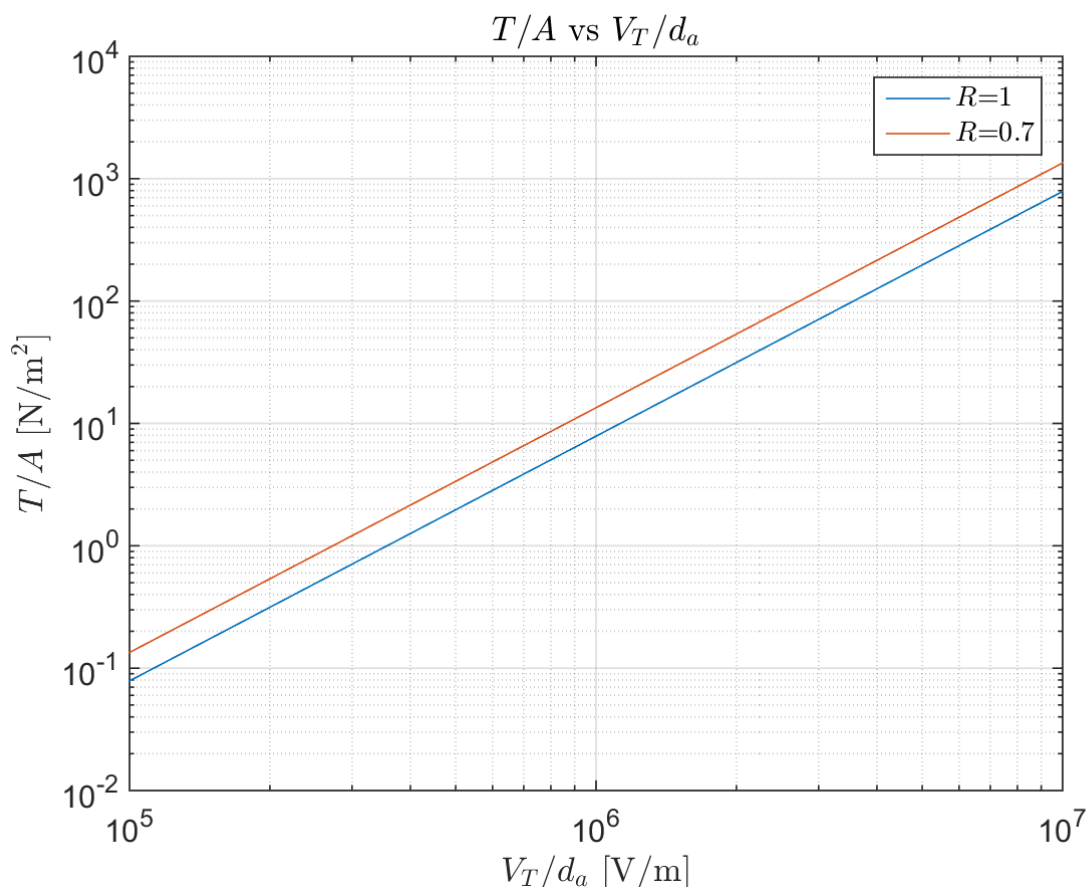
Figure 5.9: Comparison between 2 (R=1) or 3 (R=0.7) grids thrust.

As we can see, thrust density is increased by reducing the ratio V_N/V_T. We should note that V/d in the horizontal axis of the fig. 19 is different for each case. We represent $T/A = f(V_T/d_a)$ for $R = 1$ grid and $T/A = f(V_N/d_a)$ for $R = 0.7$.

Finally, we can compute the total beam current by integrating the current density over all the open area of a grid hole, of diameter D_a, and multiplying it by the number of holes (n_h) of the grids,

$$J_B = n_h \frac{\pi}{9} \varepsilon_0 \sqrt{\frac{2e}{m_i}} \left(\frac{D_s}{d_a}\right)^2 V_T^{\frac{3}{2}} = P V_T^{\frac{3}{2}} \tag{5.25}$$

Where P is the "perveance".

Such parameter gives us information about the extraction system capabilities. In Eq. 5.25, P corresponds to the one-dimensional model, where it is important to qualitatively identify many

parameters that have influence in the determination of the beam current. Nevertheless, it does not offer good quantitative results when compared to experimental data [16].

In a three-dimensional model, other elements should be taken into consideration. Those are:

- Ratio of extractor to accelerator holes diameter $\left(\frac{D_a}{D_a}\right)$
- Grid thicknesses (t_a, t_s)
- Potential variation across the beam
- Discharge voltage (V_D)
- Sheath thickness
- Etc.

Hence, the perveance would become a function of the different parameters,

$$P = P\left(\frac{d_a}{D_a}, \frac{D_a}{D_s}, \frac{t_a}{D_s}, \frac{t_s}{D_s}, R, etc.\right)$$

All these dependencies were studied for a 2-grid extractor bombardment ion thruster with Argon as propellant. Experimental results and conclusions obtained are listed below, which have been extracted from [16].

1. *"Varying the screen hole diameter D_s while keeping constant all the ratios $(d_a/D_s, D_a/D_s , etc.)$ has only a minor effect, down to $D_s \sim 0.5$ mm if the alignment can be maintained. This confirms the dependence upon the ratio d_a/D_s ."*

2. *"The screen thicknesses are also relatively unimportant in the range studied $(t/D_s \sim 0.2 - 0.4).$ "*

3. *"Reducing $R = V_N/V_T$ always reduces the perveance, although the effect tends to disappear at large ratios of spacing to diameter (d_a/D_s) , where the effect of the negative accelerator grid has a better chance to be felt by the ions. The value of d_a/D_s at which R becomes insensitive is greater for the smaller R values."*

4. *"For design purposes, when V_N and not V_T is prescribed, a modified perveance $J_B/V_N^{3/2}$ (called the "current parameter") is more useful. One would expect this parameter to scale as $R^{-3/2}$ (as Eq.5.25 shows), favoring low values of R (strong accel-decel design). This trend is observed at low R, but, due to the other effects mentioned, it reverses for R near unity, as shown in Fig. 5.10. This is especially noticeable at small gap/diameter ratios, when a point of maximum extraction develops at $R \sim 0.7 - 0.8$, which can give currents as high as those with $R \sim 0.2$. However, as the figure also shows, the low R portion of the operating curves will give currents which are independent of the gap/diameter ratio (this is in clear opposition to the 1-D prediction of Eq. 5.25). Thus, the current, in this region, is independent of both d and D_S. This opens up a convenient design avenue using low R values: Fix the smallest distance d compatible with good dimensional control, then reduce the diameter D_s to the smallest practicable size (perhaps 0.5 mm). This will allow more holes per unit area (if the hole spacing varies in proportion to their size), hence more current per unit grid area."*

5. *The perveance generally increases as D_a/D_s increases, with the exception of cases with R near unity, when an intermediate $D_a/D_s = 0.8$ is optimum.*

6. *Increasing V_D/V_T, which increases the plasma density, appears to flatten the contour of the hole sheath, which reduces the focusing of the beam. This results in direct impingement on the screen, and, in turn, forces a reduction of the beam current.*
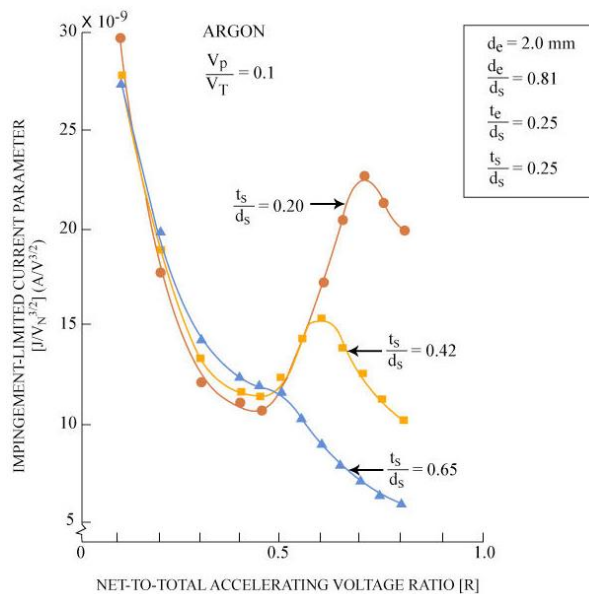
Figure 5.10: Effect of grid separation on impingement-limited current parameter [28]. *In the picture d_s corresponds to d_a .*

With the experimental results obtained and stated above, a 3-D correction of the expression 5.25 can be made by replacing d_a^2 by $(d_a + t_s)^2 + D_s^2/4$. It has demonstrated much closer values to experimental data obtained for J_B. Hereafter, J_B expression is rewritten taking into account such modification,

$$J_B = n_h \frac{\pi}{9} \varepsilon_0 \sqrt{\frac{2e}{m_i}} \left(\frac{D_s^2}{(d_a + t_s)^2 + D_s^2/4} \right) V_T^{\frac{3}{2}} \qquad (5.26)$$

Results given by Eq. 5.26 are presented in Fig. 5.12. Geometrical parameters requested have been taken from a real J-series ion thruster and those are specified in the table below.

Moreover, observed extraction capacity from the same thruster has also been plotted in Fig. 5.12. The reported beam current show the following correlation [16],

$$J_{B\,J-series} = \frac{17.5(V_T/1000)^{2.2}}{\xi \sqrt{M}} \pm 25\,\%$$

Where ξ is a double-ion correction factor and M is the molecular mass of the propellant in atomic mass unit.

30 cm J-Series ion thruster	
d_a [mm]	0.50
t_s [mm]	0.38
D_s [mm]	1.90
D_a [mm]	1.14
Grids diameter [cm]	30
Number of holes	14860
R	0.7
ξ	0.934
Propellant	Xenon
M [u]	131.3

Table 5.1: J-Series ion thruster parameters [16].
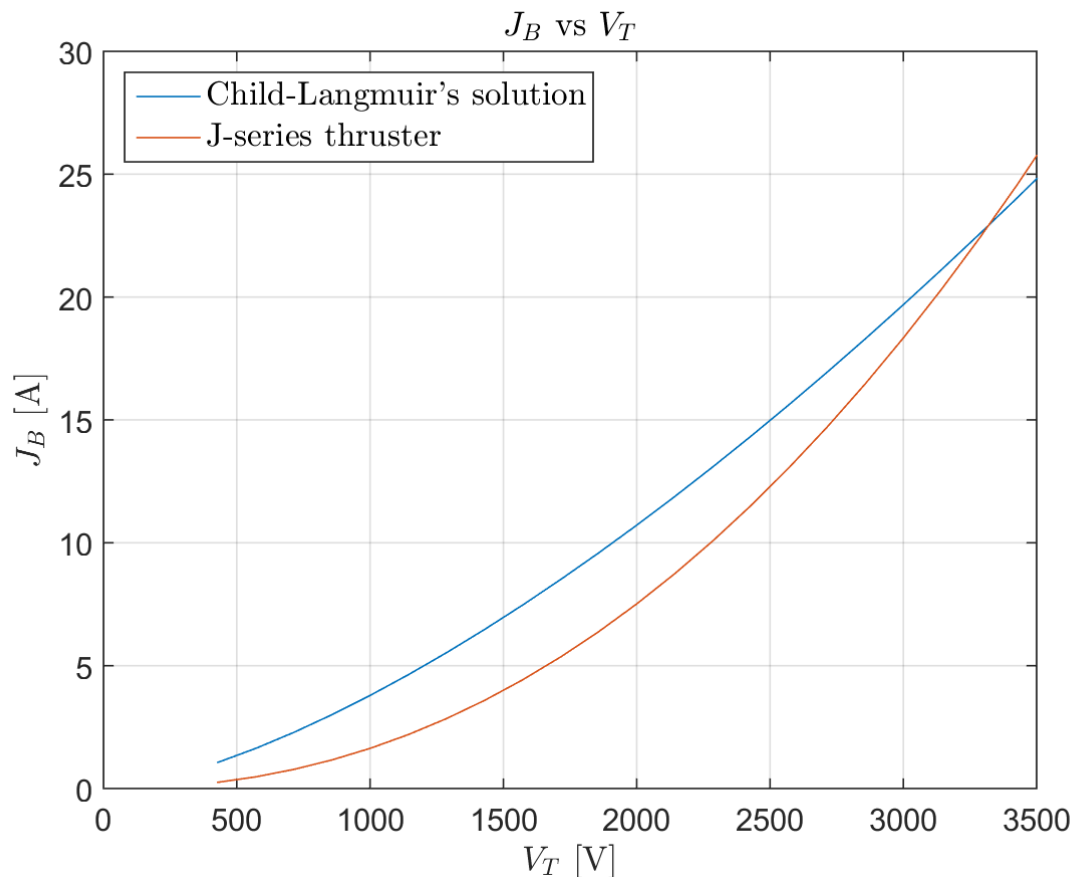
Figure 5.11: Maximum ion current and thrust, given a thruster design, as a function of the total voltage.

We should remind that, this study (Section 5.2.1), is a preliminary analysis to assess the limitations of an ion thruster, given an extracting system configuration, since we have assumed that our thruster is in the space charge limited operating condition (ideal point to maximise the mass propellant flow rate).

If we compare results obtained in Fig. 5.12, we see that, for reasonable values of V_T (< 2500 V), differences between observed data and calculated currents exceed 25 % (margin of error for reported data).

Therefore, we can conclude that Child-Langmuir's solution does not provide accurate results for maximum beam currents, given an extracting system design. Nevertheless, as a preliminary analysis, it gives a rough idea about the $J_B - V_T$ curve shape and the order of magnitude of the maximum ion flux (and hence, the thrust) of an ion thruster.

5.2.2. Ionisation chamber

The other main stage of the ion thruster is focused on the discharge chamber, where ionisation takes place. In an electron bombardment ioniser, two conveniently located electrodes are responsible for creating a DC discharge, in order to energise the electrons which will impact the atoms of the neutral plasma injected. The cathode can be a simple heated tungsten filament or a hollow cathode, which has a longer lifetime. The anode consists of the lateral walls of the chamber.

Before examining the procedures occurring inside the chamber, the different particles that coexist in the region should be distinguished.

First of all, we find the neutral atoms of the propellant gas, being the most commonly used xenon, argon, krypton or mercury. Such atoms, after suffering a collision can be singly or multiply ionised. The latest is not desirable although it occurs to some extent. However, we will consider a plasma of singly charged ions (higher ionisation levels can be neglected).

On the other hand, we find negatively charged particles, the electrons, among which we can differentiate two species, primary and secondary (also called Maxwellian) electrons.
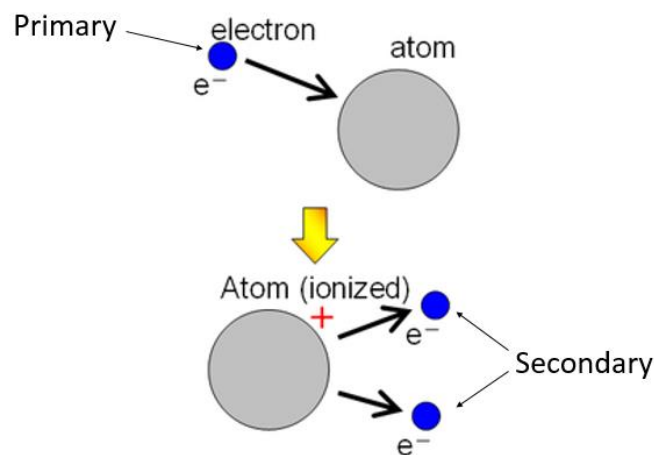
Figure 5.12: Ionisation procedure [29].

Primary electrons are those accelerated through an electric field adjacent to the cathode, and they have energies on the order of three or four times that of the first ionisation energy of the propellant gas (12.13 eV for xenon). The energy of these particles is determined by the cathode-anode potential difference (V_D), about 30-50 V, which are typical values for most

gases. The magnitude of this voltage is chosen so that first ionisation is highly likely whereas multiply ionisation probability is small. Once an inelastic interaction has occurred between a neutral propellant atom and a primary electron, a second group of electrons is originated (Fig. 5.13).

On the one hand, the collision cuts down the energy of the primary electron and it becomes secondary. On the other hand, ionisation results in the release of low energy secondary electron from the atom. Therefore, there is an electron population with a "Maxwellian" energy distribution which is characterised by a temperature on the order of a few eV (3-8 eV). The term Maxwellian comes from the so-called Maxwell-Boltzmann distribution, a probability distribution for describing particles speed in idealised gases. It indicates which range of speeds are more likely and, therefore, which temperatures. Gases studied here, mentioned above, behave very nearly like an ideal gas at ordinary temperatures and low particle densities ($\sim 10^{18} cm^{-3}$), and the Maxwell speed distribution is an excellent approximation for such gases.

It should be noted that ionisation may be due to either primary or secondary electrons. Only the high energy part of the Maxwellian energy distribution is above the ionisation energy and can contribute to such process, but their number density greatly exceeds that of the primaries, and both contributions are in fact, of the same order.

The walls of the chamber constitute the anode through which electrons leave the container to be ejected then by the neutraliser. In order to avoid the loss of electrons to the anode before having an inelastic collision, it is desirable to maximise the residence time of both types of electrons in the chamber. This is achieved by means of a suitable distribution of confining magnetic fields. Different configurations have been employed over time; axial magnetic field (Fig. 5.16 (left)), divergent-field (Fig. 5.16 (right)) and ring cusped field (Fig. 5.16 (down)) are examples. The last one is the most effective configuration and it will be discussed in this document.

As it has been said, the thruster operates with the entire discharge chamber at anode potential (except for the screen grid). Therefore, magnetic field lines at the field cusps end on such anode potential surfaces, allowing electrons to be lost to the anode by travelling along the magnetic field lines.
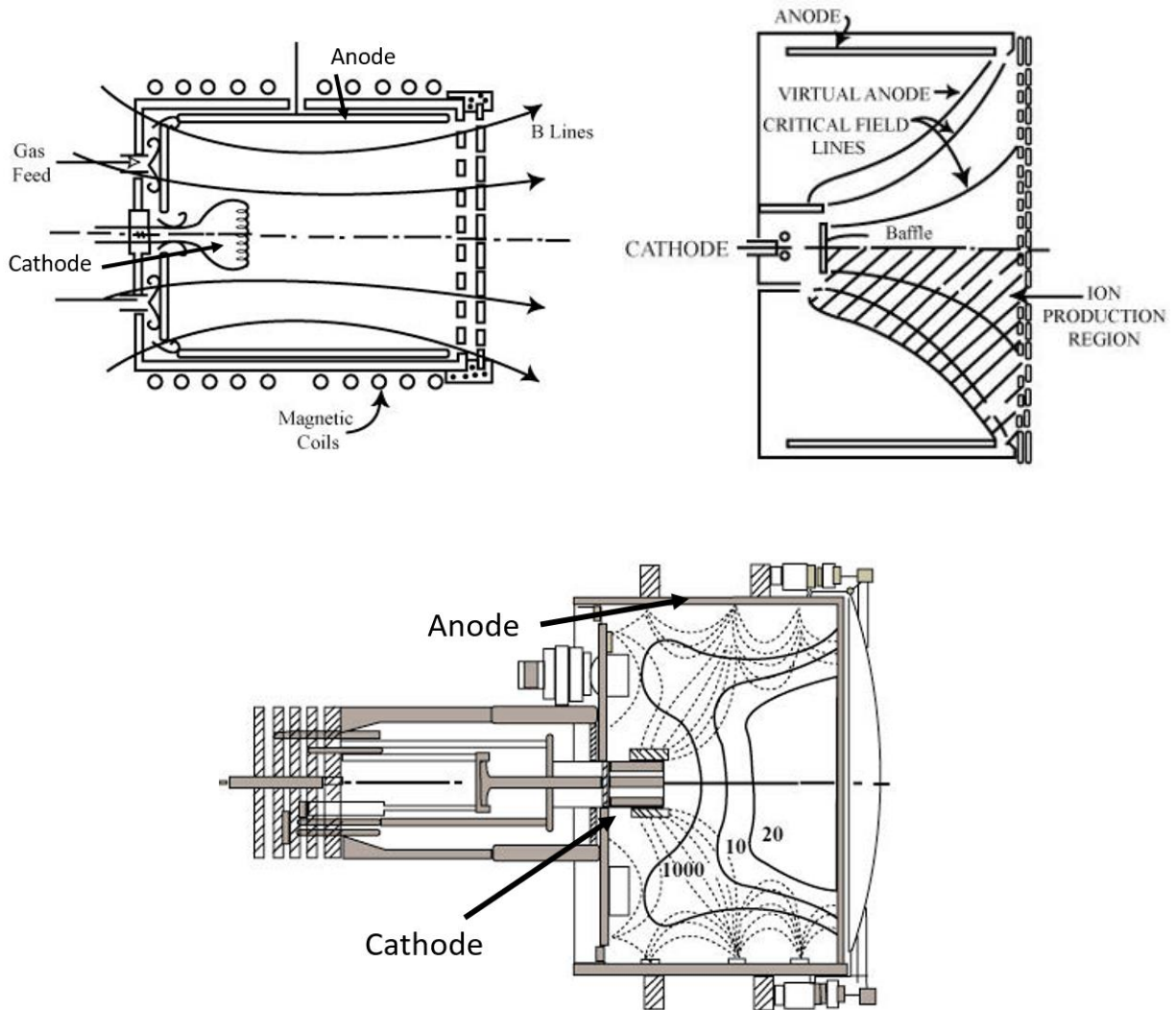
Figure 5.13: Types of ion thrusters depending on the magnetic field. Axial magnetic field ion thruster (left), divergent field ion thruster (right) and ring cusped field ion thruster (down) [16].

After being ionised, the positively charged particles wander randomly in the discharge chamber. When they reach any of the walls at cathode potential (which are negatively charged with respect to plasma), they penetrate the sheath at a velocity of the order of the Bohm velocity (Section 4.2.2),

$$v_B = \sqrt{\frac{kT_e}{m_i}} \qquad (5.27)$$

These walls can be either solid walls or the screen grid. The former ones are not desirable since ions collide with them being neutralised and leading to sputtering. After that, neutral atoms return to the plasma where they can be ionised again. Otherwise, if ions reach a hole of the screen grid, they are accelerated and become part of the ion beam, generating the thrust as it was explained in Section 5.2.1.

In Chapter 6, a theoretical model shall be developed in order to assess the performance of the ionisation chamber, allowing us to numerically analyse the process described above.

Chapter 6.   Theoretical chamber performance model (Brophy's Theory)

In this section, a theoretical model to assess thruster's performance will be developed using Brophy's Theory. It shall enable us to know and optimise the main parameters that affect the operation of the ionisation chamber.

Ion thruster's performance are typically measured in terms of the power required to produce an ion beam current at a given propellant utilisation efficiency. It must be noted that power needed to accelerate ions should not be considered.

Before finding a general expression that represents the performance, all power sources and currents must be identified.

A schematic design of an ion thruster is shown in Fig. 6.1.
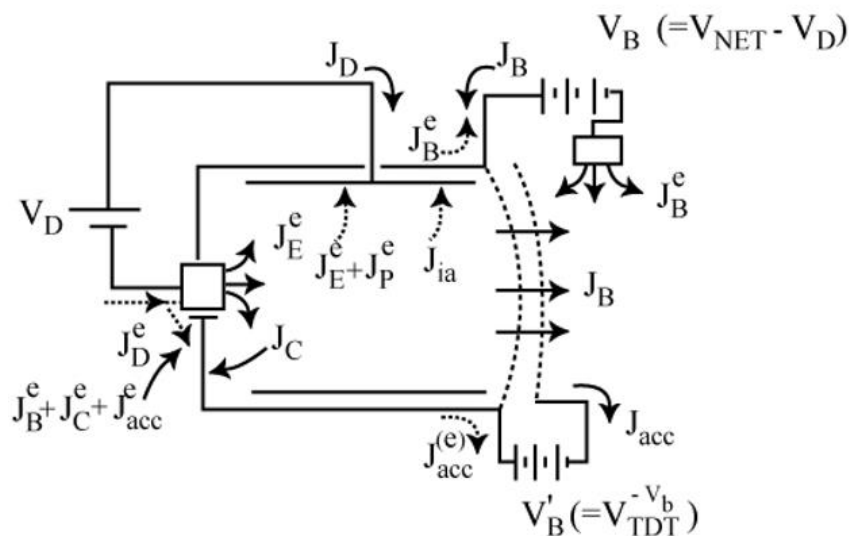
Figure 6.1: Schematic of an ion thruster [28]*.*

It is worth recalling that a potential sheath will exist at all plasma boundaries. The plasma in the discharge chamber will typically assume a few volts above the wall's potential (potential

drop ϕ_w in Section 4.2.2). Therefore, ions will be able to reach all the discharge chamber walls, entering the sheath at the Bohm velocity. Electrons, on the other hand, will be reflected by the sheath at cathode potential surfaces (cathode and screen grid). They will leave the ionisation chamber, hence, only at anode potential surfaces, where the potential drop is not enough to reflect them. Actually, the most energetic electrons in the tail of the Maxwellian distribution, would be able to reach cathode potential surfaces (they will be neglected).

J_P is the total ion current produced (measured in Amperes), and there must be, therefore, the same ion current leaving the plasma because of the statement of continuity. Since the evacuation routes for ions are cathode potential surfaces (J_C), anode potential surfaces (J_A) or the extraction grids (a part is intercepted by the accelerator grid (J_{acc}) and other is extracted into the beam (J_B)), the next balance can be done, which is the statement of continuity for the ions,

$$J_P = J_B + J_C + J_A + J_{acc} \tag{6.1}$$

Regarding electrons, an equal electron current of the same magnitude as the total ion production rate must be also produced ($J_P^e = J_P$) because of the collisions that take place. Moreover, there is the electron current emitted by the cathode (J_E). Both of the electron currents must be evacuated by the anode and they must equal the discharge current (J_D). We have to subtract the ion current that is also lost to the anode and neutralised.

$$J_D^e = J_P^e + J_E^e - J_A \tag{6.2}$$

On the other hand, from the total discharge current (J_D^e) returned to the cathode, a part of the electrons is emitted (J_E^e) and another part is managed by the neutraliser, which produces a current of the same magnitude as the ion beam current to achieve a neutral exhaust stream ($J_B^e = J_B$). Furthermore, we have to consider the electrons used to neutralise ions lost to cathode potential surfaces (J_C^e) and those by the accelerator power supply to neutralise the ions intercepted by the accelerator grid (J_{acc}^e). Making this balance, we reach the continuity statement for the electrons.

$$J_D^e = J_B^e + J_E^e + J_C^e + J_{acc}^e \tag{6.3}$$

Combining Eqs. 6.1, 6.2 and 6.3 leads to a total current rate of zero. That means the balance is correctly done:

$$J_B + J_C + J_A + J_{acc} + J_E^e - J_A - (J_B^e + J_E^e + J_C^e + J_{acc}^e) = 0$$

Regarding the power sources, three of them can be distinguished in Fig. 6.1. The first one is the discharge power supply, which is used to operate the discharge chamber, and works at a voltage V_D .

Another one is used to operate the neutraliser. This power source must generate an electron current at a sufficient rate to neutralise the exhaust stream, and works at a voltage V_B.

The last one is applied between the grids in order to neutralise the intercepted ion current J_{acc}. This power source works at a voltage difference of $V_B^{'}$.

6.1. Beam ion energy cost

Since the average energy cost per beam ion (ε_B) must be determined to assess the thruster's performance, a first definition is needed:

$$\varepsilon_B = \frac{Total\ Power - Useful\ Power}{J_B} \tag{6.4}$$

This parameter represents the energy invested in producing a beam ion (eV/ beam ion), where,

$$Useful\ Power = J_B(V_B + V_D) \tag{6.5}$$

$$Total\ Power = J_B V_B + J_D V_D + J_{acc} V_B' + J_E V_C \tag{6.6}$$

$Useful\ power$ is the one that may be used to generate thrust, whereas $total\ power$ take into account the power spent over all the thruster to operate it.

It should be noted that an extra power has been added to the last expression ($J_E V_C$). This missing power is used to operate the hollow cathode and it is assumed that primary electrons are accelerated from this potential difference (V_C). For thermionic cathodes, $V_C = 0$, however, additional power should be supplied to operate them.

Therefore, ε_B yields

$$\varepsilon_B = \frac{(J_D - J_B)V_D + J_{acc}V_B{'} + J_E V_C}{J_B} \tag{6.7}$$

Similarly, an average cost per plasma ion (ε_P) can be defined:

$$\varepsilon_P = \frac{Input\ Power}{J_P} \tag{6.8}$$

ε_P represents the energy investment to create ions in the discharge chamber plasma (eV/plasma ion), where,

$$Input\ Power = J_E V_D + J_E V_C \tag{6.9}$$

The last expression reflects the power provided to the primary electrons, that is, the total power to only operate the discharge chamber.

Finally, ε_P can be expressed as,

$$\varepsilon_P = \frac{J_E(V_D + V_C)}{J_P} \tag{6.10}$$

Rearranging terms, Eq. 6.7 can be rewritten as,

$$\varepsilon_B = \frac{\varepsilon_P J_P}{J_B} + \frac{V_D J_C}{J_B} + \frac{J_{acc}(V_B' + V_D)}{J_B} \tag{6.11}$$

From now on, the following ion fractions, referred to the total ion current produced, will be used, since it is more useful and convenient to work with dimensionless quantities,

$$f_B = \frac{J_B}{J_P} \qquad f_C = \frac{J_C}{J_P} \qquad f_A = \frac{J_A}{J_P} \qquad f_{acc} = \frac{J_{acc}}{J_P}$$

Therefore,

$$\varepsilon_B = \frac{\varepsilon_P}{f_B} + \frac{V_D f_C}{f_B} + \frac{(V_B' + V_D)f_{acc}}{f_B} \tag{6.12}$$

We have obtained an equation that describes the beam ion energy cost as a function of the plasma ion energy cost (ε_P), the different ion fractions (f_B, f_C, f_{acc}), and the voltages V_D and V_B'.

The first term of the right hand side of the equation shows the missing energy associated with extracting only a fraction from all ions produced. As it is shown in Eq. 6.1, there are some current losses to the walls (J_C, J_A, J_{acc}).

The second term represents the energy loss for accelerating ions towards cathode potential surfaces inside the chamber, leading, moreover, to undesirable sputtering.

The third term represents the energy wasted by ions intercepted by the accelerator grid. This contribution could be neglected in front of the magnitude of the other terms, since a very small part of the ions produced is intercepted ($J_{acc} \ll J_P$). That would yield, for ε_B,

$$\varepsilon_B = \frac{\varepsilon_P}{f_B} + \frac{V_D f_C}{f_B}$$

(6.13)

Therefore, we must obtain a model to express the behaviour of the right hand side terms as a function of the propellant utilisation efficiency (η_u), in order to be able to plot the performance curves.

6.2. Plasma ion energy cost

The plasma ion energy cost (ε_P) is the parameter, in Eq. 6.13, that reflects all mechanisms of energy loss from the discharge chamber plasma, except for the acceleration of ions to cathode potential surfaces, which is considered in the second term. In order to obtain an expression for ε_P as a function of the propellant utilisation efficiency (η_u), a power balance on the discharge chamber should be made.

PRIMARY ELECTRON INPUT
$J_E(V_D - V_C)$

DISCHARGE CHAMBER PLASMA (CONTROL VOLUME)

MAXWELLIAN ELECTRONS LOST TO ANODE
$J_M \epsilon_M$

EXCITATION
$\sum_j J_j U_j$

IONISATION
$J_P U^+$

PRIMARY ELECTRON LOST TO ANODE
$J_L(V_D - V_C)$
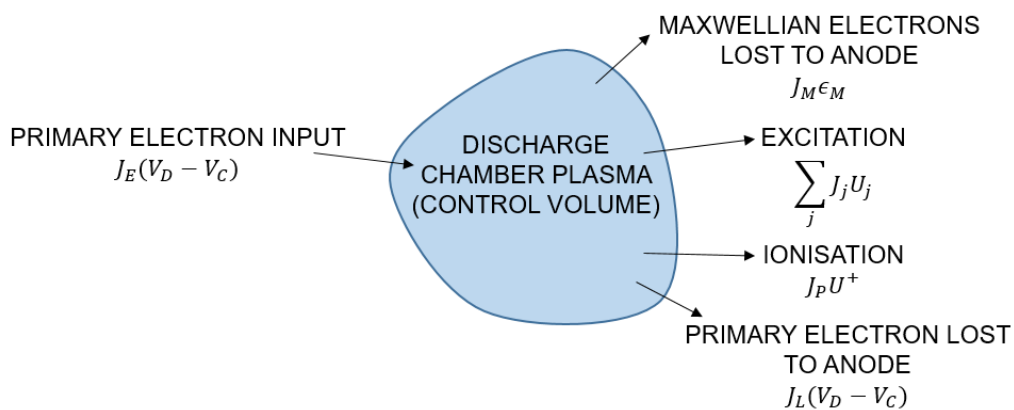
Figure 6.2: Power balance in discharge chamber.

Last figure represents the control volume of the analysis, whose boundaries are defined by the plasma sheath.

The input power is that used to accelerate primary electrons. Note that it is not the same as defined in Eq. 6.9, where we were considering the total power to operate the chamber. This idea is clarified in Fig. 6.3. We have two power sources (V_C and V_D), which contribute to the power cost to operate the device. On the other hand, the primary electrons are assumed to be accelerated from a cathode region plasma potential, which is V_C volts above cathode potential, to the potential of the bulk plasma, which is assumed to be near that of the anode (V_D in the figure, taking into account the reference of 0 V shown).

Therefore, the primary electrons power is $J_E(V_D - V_C)$.
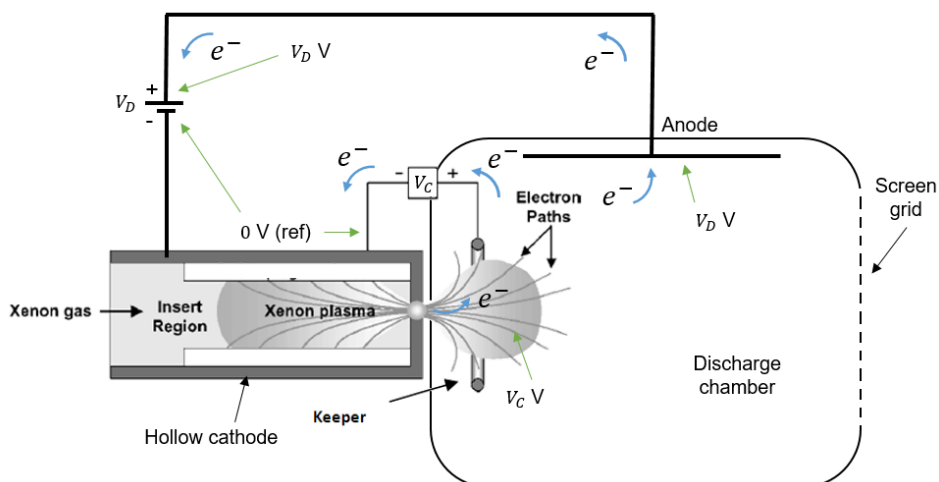
Figure 6.3: Schematic of hollow cathode and discharge power supplier operation.

On the other hand, that energy is lost across the boundaries of the plasma by means of four types of energy carriers;

-   Ions: Are lost through all interior chamber surfaces and have a rate of energy associated of $J_P U_+$, where U_+ is the first ionisation energy of the propellant atoms.
-   Photons: Can be also lost through all interior surfaces and have a rate of energy associated of $\sum_j J_j U_j$, where J_j is the rate at which the j_{th} excited neutral state of the atoms is produced. U_j is the excitation energy of each j_{th} excited state.

- Primary electrons: These are assumed to be lost only to the anode surfaces, and their energy is $J_L(V_D - V_C)$, where J_L is the part of the emitted electrons that have not had an inelastic collision.
- Maxwellian electrons: Secondary electrons are also assumed to be lost to the anode surfaces, and their energy is $J_M \varepsilon_M$. J_M is the part of the emitted electrons that have suffered an inelastic collision in addition to the electrons produced as a result of such collision. ε_M is the average energy of a Maxwellian electron lost to the anode.

If steady state is assumed, the input rate of energy must equal the evacuation rate, hence,

$$J_E(V_D - V_C) = J_P U_+ + \sum_j J_j U_j + J_M \varepsilon_M + J_L(V_D - V_C) \tag{6.14}$$

Let us analyse now, how the production rates (J_P, J_j) are calculated.

6.2.1. Ion production currents

When collisions take place in a plasma, ionisation or excitation of neutral atoms can occur. In order to quantify the particles produced per unit time, different parameters must be taken into account.

When a charged particle collides with a neutral atom, it can undergo an elastic or an inelastic collision. The probability that such a collision will occur can be expressed in terms of an effective cross-sectional area (σ $[m^2]$), also called collision cross section.

As well, such ion production rate should depend upon the density of particles concerned during collisions and the velocity of the energetic ones.

Therefore, an ion production rate per unit volume is given by,

$$\frac{dn_i}{dt} = n_o n_e < \sigma_i v_e > \tag{6.15}$$

Where σ_i is the collision cross section of the atoms, n_o is the neutral atom density, n_e is the total electron density and v_e is the electron velocity. The use of brackets in the last expression means that this parameter must be averaged over the entire electron energy distribution function (electrons velocity is directly related with their energy).

Finally, we can express the ion production current as,

$$J_P = e n_o n_e < \sigma_+ v_e > V \qquad (6.16)$$

where V is the volume of the ion production region and σ_+ is the ionisation collision cross section when singly ionisation of neutral atoms takes place.

In a similar way, the rate at which the j_{th} excited state is produced can be obtained,

$$J_j = e n_o n_e < \sigma_j v_e > V \qquad (6.17)$$

Now, σ_j indicates the probability that a particle will be excited to j_{th} level. Again, the term $< \sigma_j v_e >$ represents the product of the j_{th} excitation cross section and the electron velocity averaged over the entire electron speed distribution.

6.2.2. Electron currents

As said before, both J_M and J_L are fractions of the total electron current (J_T) so as to,

$$J_T = J_M + J_L = J_P + J_E \qquad (6.18)$$

Eq. 6.19 gives us the fraction of the emitted electrons that are lost without having an inelastic collision,

$$\frac{J_L}{J_E} = e^{-\sigma_0' n_0 l_e} \qquad (6.19)$$

It comes from a "survival analysis", statistical analysis made for calculating the population of primary electrons lost to the anode as a function of n_0, σ_0' and l_e [30].

σ_0' is the so-called total inelastic collision cross section and it is given by,

$$\sigma_0' = \sigma_+' + \sigma_{ex}' \qquad (6.20)$$

Unlike σ_+ and σ_j, these collision cross sections should be evaluated at the primary electron energy, being it denoted by the apostrophe.

On the other hand, l_e is the average distance that a primary electron would travel before being collected by the anode without having a collision. It is called primary electron containment length and its magnitude directly depends on the thruster size and the magnetic fields. This is the main parameter that one could manage by means of the strength or layout of the static magnets, in order to optimise the ionisation chamber operation. As we saw in Section 4.2.1, charged particles within a disturbing magnetic field perform a cycloidal motion around the field lines. Nevertheless, the study of this characteristic length is out of the scope of this project.

Making use of equations 6.14 to 6.20, we can arrive to an expression for ε_P that is a function of the neutral density (n_o) (Fig. 6.21).

$$\varepsilon_P = \left(\frac{\epsilon_0 + \varepsilon_M}{1 - \dfrac{V_C + \varepsilon_M}{V_D}} \right) (1 - e^{-\sigma_0' n_0 l_e})^{-1} \tag{6.21}$$

For the purpose of finding a relation between the plasma ion energy cost and the propellant utilisation efficiency (η_u) (so as to obtain the performance curves), neutral density shall be written as a function of η_u.

Propellant utilisation, by definition, is given by,

$$\eta_u = J_B / \dot{m} \tag{6.22}$$

Where $\dot{m}$ $[A]$ is the total inlet flow rate expressed in equivalent amperes, which is given by the following statement of continuity, equalling it to the outlet flow rate,

$$\dot{m} = J_B + \dot{n}_0 \tag{6.23}$$

The output stream is the beam ion current (responsible for generating thrust) in addition to the neutral flow rate, which consists of the neutral atoms leaving the chamber without being ionised. The later can be expressed as,

$$\dot{n}_0 = \frac{1}{4} n_0 e v_0 A_g \phi_0 \tag{6.24}$$

The neutral flow rate may be calculated from the kinetic theory of gases, and expression 6.24 is the result obtained from the "Free molecular flow through a sharp-edged orifice" theory [30].

It can be seen that $\dot{n}_0$ is proportional to the neutral atom thermal velocity (v_0), the total area of the grid (A_g), and the grid system transparency to neutral atoms (ϕ_0), in addition to the neutral atom density.

The mentioned velocity is obtained from the thermal energy of the neutral particles, which is assumed to be at an effective wall temperature (T_W) (in the order of 400 K), hence,

$$v_0 = \sqrt{\frac{8kT_w}{\pi m_i}} \tag{6.25}$$

Where k is the Boltzmann constant, a physical constant which relates energy with temperature of particles.

The grid transparency (ϕ_0) is a parameter that reflects the ease of crossing the grid system by the neutral atoms, and depends upon both the screen and accelerator grid transparencies (ϕ_s, ϕ_a), as it will be seen later.

It is given by the next expression, obtained from [28],

$$\frac{1}{\phi_0} = \frac{1}{\phi_s} + \frac{1}{\phi_a} - 1 \tag{6.26}$$

Finally, combining Eqs. 6.21, and 6.22 to 6.25, we obtain an expression for ε_P as a function of the propellant utilisation efficiency (η_u),

$$\varepsilon_P = \frac{\varepsilon_P^*}{1 - e^{-C_0 \dot{m}(1-\eta_u)}} \tag{6.27}$$

where,

$$C_0 = \frac{4\sigma_0' l_e}{e v_0 A_g \phi_0} \tag{6.28}$$

and,

$$\varepsilon_P^* = \frac{\epsilon_0 + \varepsilon_M}{1 - \dfrac{V_C + \varepsilon_M}{V_D}} \tag{6.29}$$

C_0 is the so-called primary electron utilisation factor and reflects the degree to which primary electrons interact with neutral atoms, that is, the confinement effectiveness for primary electrons. There is an interest in large values, since it would mean a lower plasma ion energy cost. We can see here the importance of increasing the electron path length and decreasing the transparency to neutrals. It should be noted that, if C_0 tends to infinite, ε_P tends to its lower limit, ε_P^*.

Therefore, ε_P^* represents the plasma ion energy cost without primary electron losses. It is called baseline plasma ion energy cost. ϵ_0 parameter, which is introduced in Eq. 6.21, has been defined to ease the comprehension of ε_P^* and is given by,

$$\epsilon_0 = U_+ + \frac{\sum_j <\sigma_j v_e> U_j}{<\sigma_+ v_e>} \tag{6.30}$$

Last expression reflects the energy expended in ionisation and excitation reactions, where the second term may be thought as the relative amount of energy expended in excitations compared to ionisation of neutrals atoms.

Once ε_P has been obtained, we can retrieve Eq. 6.13 to express the beam ion energy cost as a function of the propellant utilisation efficiency,

$$\varepsilon_B = \frac{\varepsilon_P^*}{f_B[1 - e^{-C_0 \dot{m}(1-\eta_u)}]} + \frac{V_D f_C}{f_B} \tag{6.31}$$

Last equation allows us to calculate performance curves for a given thruster design.

Chapter 7.   Numerical analysis

In this section, a numerical study will be performed so as to assess the performance of a given ion thruster. The model presented in Chapter 6 will be used to that end.

The performance curves shall be given by the Eq. 6.31, which is recovered hereafter,

$$\varepsilon_B = \frac{\varepsilon_P^*}{f_B[1 - e^{-C_0 \dot{m}(1-\eta_u)}]} + \frac{V_D f_C}{f_B}$$

The parameters on which ε_B depends are listed below:

- f_C: Fraction of ion current to cathode surfaces
- f_B: Extracted ion fraction
- V_D: Discharge voltage
- $\dot{m}$: Propellant flow rate
- C_0: Primary electron utilisation factor
- ε_P^*: Baseline plasma ion energy cost
- T_M: Maxwellian electron temperature in bulk plasma (Through ε_P^*)

Let us analyse how they are calculated or which values they might have.

7.1.   Parameters determination

7.1.1. Baseline plasma ion energy cost

This parameter's expression has been obtained in section 6 (Eq. 6.29) and is given by,

$$\varepsilon_P^* = \frac{\epsilon_0 + \varepsilon_M}{1 - \dfrac{V_C + \varepsilon_M}{V_D}}$$

where,

$$\epsilon_0 = U_+ + \frac{\sum_j <\sigma_j v_e> U_j}{<\sigma_+ v_e>} \tag{7.1}$$

Last equation, after several simplifications and assumptions (shown in [30]), can be rewritten as,

$$\epsilon_0 = U_+ + \frac{\left(\frac{n_p}{n_M}\sigma'_{ex}v_p + <\sigma_{ex}v_e>_M\right)U_{ex}}{\frac{n_p}{n_M}\sigma'_+ v_p + <\sigma_+ v_e>_M} \tag{7.2}$$

As it can be seen, some changes and new parameters have been introduced. First of all, since our plasma is characterised by a group of primary electrons and a Maxwellian group with a distribution of temperature T_M, reaction rates ($<\sigma v>$) have been separated into two parts. The first one refers to primary electrons and, since they are monoenergetic, they are characterised by a specific cross section and velocity. The ionisation and excitation collision cross sections at the primary electron energy are denoted, respectively, by σ'_+ and σ'_{ex}. v_p is the primary electrons velocity and it is defined using thermal energy equation,

$$v_p = \sqrt{\frac{2e(V_D - V_C)}{m_e}} \tag{7.3}$$

On the other hand, the second part of the reaction rates belongs to the Maxwellian group. Therefore, as they have an energy distribution, the enclosed product must be averaged over the Maxwellian energy distribution function. This is denoted by $<\sigma v_e>_M$.

It should be noted that, unlike Eq. 7.1, the summation over all j_{th} excited states has been approximated considering a single equivalent excited state characterised by a total excitation collision cross section(σ_{ex}) and a lumped excitation energy (U_{ex}). This term can be approximated by,

$$U_{ex} = \frac{1}{2}(U_l + U_+) \tag{7.4}$$

Where U_l is the lowest excitation energy and U_+ is the first ionisation energy.

The values of both reaction rates in Eq. 7.2, ($<\sigma_{ex}v_e>_M$ and $<\sigma_+ v_e>_M$) are a function of the mean Maxwellian electron temperature. An analytical approximation for those parameters is found in [31].

Finally, a last parameter must be determined in order to calculate the baseline energy cost. ε_M is the average energy of the Maxwellian electrons lost to the anode, which can be calculated as,

$$\varepsilon_M = 2T_A + V_A \tag{7.5}$$

where V_A is the potential difference between the plasma and the anode, and has been experimentally found that it is approximately 2 V. T_A is the electron temperature at the anode. Empirical results are depicted in the figure below, which show the variation of T_A with T_M.
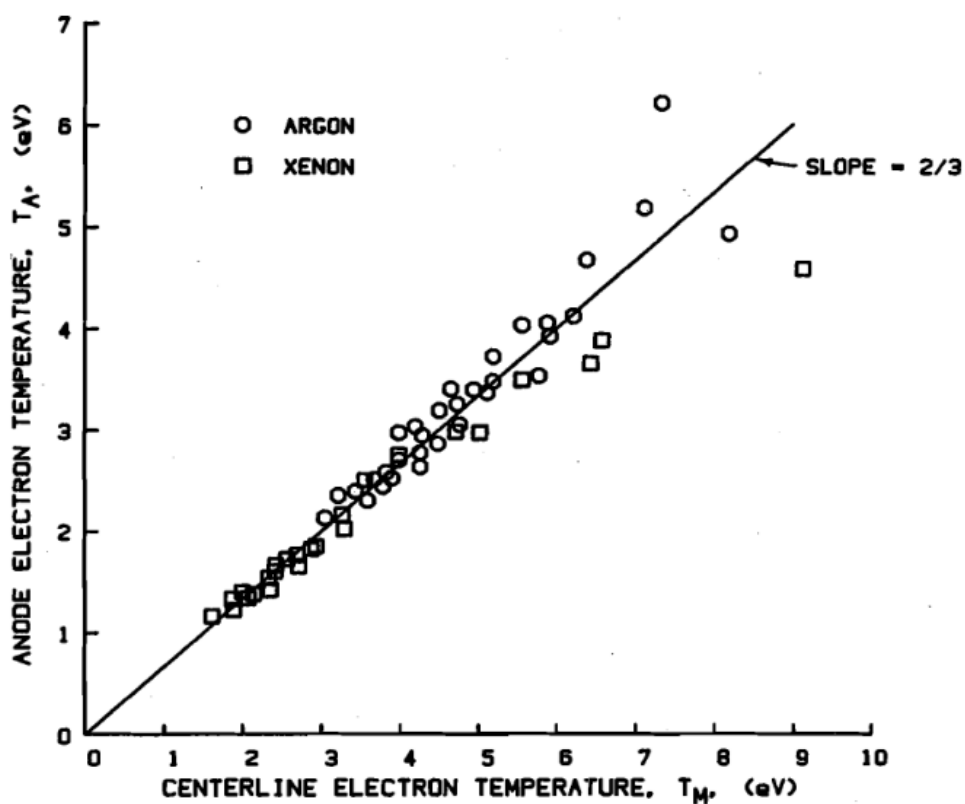

Figure 7.1: Electron temperatures at anode and bulk plasma [30].

From the slope of the curve, it can be extracted that,

$$T_A = \frac{2}{3}T_M \tag{7.6}$$

and therefore,

$$\varepsilon_M = \frac{4}{3}T_M + V_A \tag{7.7}$$

From Eq. 6.29, we could obtain now the curves $\varepsilon_P^* = f(T_M)$ for different values of primary-to-Maxwellian electron densities ratio $(\frac{n_p}{n_M})$. Nevertheless, we have to take into account that such ratio depends on the electron temperature (T_M) and, hence, another expression, that relates $\frac{n_p}{n_M}$ with ε_P^*, should be found.

For that purpose, we will make use of the ratio of ion current produced by primaries to the total ion current produced, whose obtainment is detailed in [30],

$$\frac{J_P'}{J_P} = \frac{\varepsilon_P^* \sigma_+'}{V_D \sigma_0'} \tag{7.8}$$

From the definition of both ion currents,

$$J_P = n_0 n_p e v_p \sigma_+' V + n_0 n_M e < \sigma_+ v_e >_M V \tag{7.9}$$

$$J_P' = n_0 n_p e v_p \sigma_+' V \tag{7.10}$$

And Eq. 8.8, next expression for ε_P^* can be obtained,

$$\varepsilon_P^* = \frac{V_D \sigma_0'/\sigma_+'}{1 + \frac{< \sigma_+ v_e >_M}{\frac{n_p}{n_M} v_p \sigma_+'}} \tag{7.11}$$

Finally, two equations have been obtained (Eqs. 6.29 and 7.11), with which the dependence of the baseline cost can be evaluated as a function of the Maxwellian electron temperature $(\varepsilon_P^*(T_M))$.

Due to the complexity of the expressions, the attainment of an analytical solution to represent the curves would be cumbersome. Therefore, an iterative process must be developed, which is specified in *Annex C.1* [21]. It will be solved numerically through a Matlab program.

For validating the code, the solution for the following control parameters have been studied, $V_D = 40\ V$ and $V_C = 0\ V$.
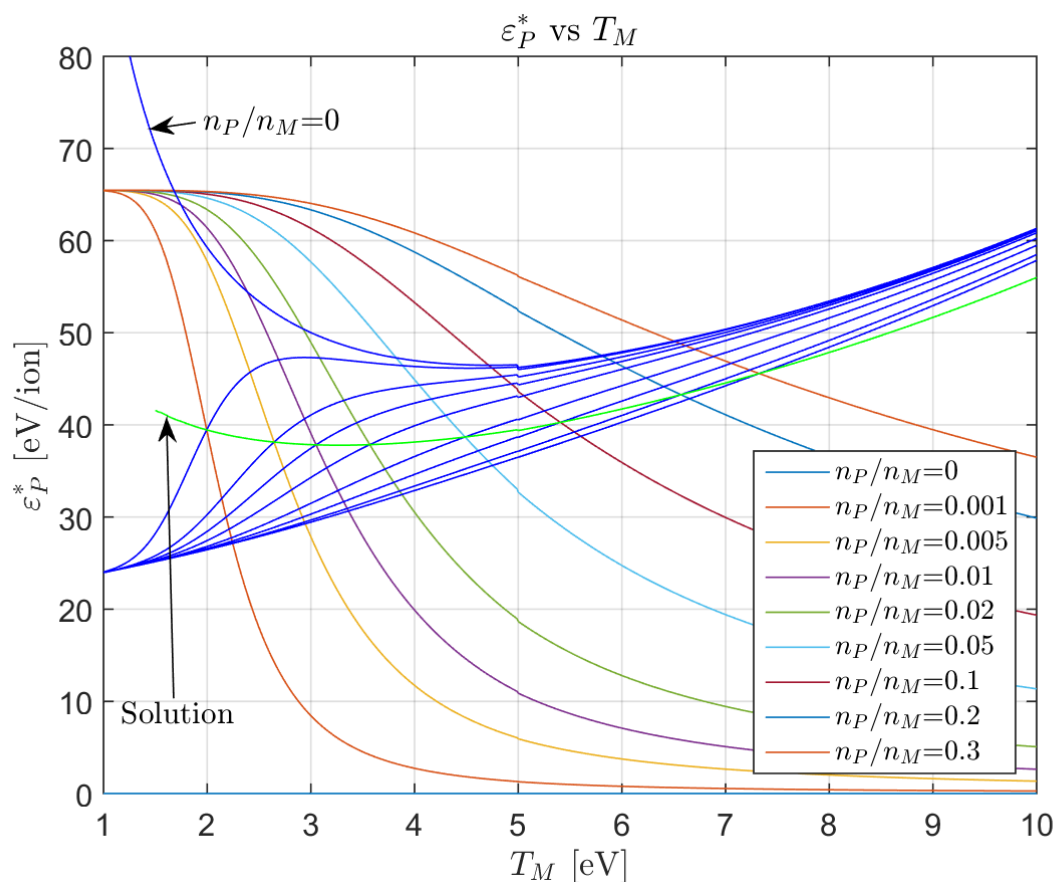
Figure 7.2: Baseline plasma ion energy cost as a function of T_M.

In Fig. 7.2, it can be seen the variation of ε_P^* with T_M. In blue, the solution for Eq. 6.29 is depicted for different values of $\frac{n_p}{n_M}$. With several colours, Eq. 7.11 solution is shown for the same values of $\frac{n_p}{n_M}$. The corresponding colour to each value of primary-to-Maxwellian electron densities ratio is specified in the legend of the plot. The green line is the result of combining the two solutions by an iteration process. As it is shown, this line pass through the intersections of the solutions for Eqs. 6.29 and 7.11 for the same value of $\frac{n_p}{n_M}$. Therefore, it can be concluded that, given V_D and V_C, the value of the baseline energy cost can be computed as a function of T_M. Moreover, the code implemented for the iteration process is correct, although the results should be validated.

If the results obtained are compared with those given in [30],
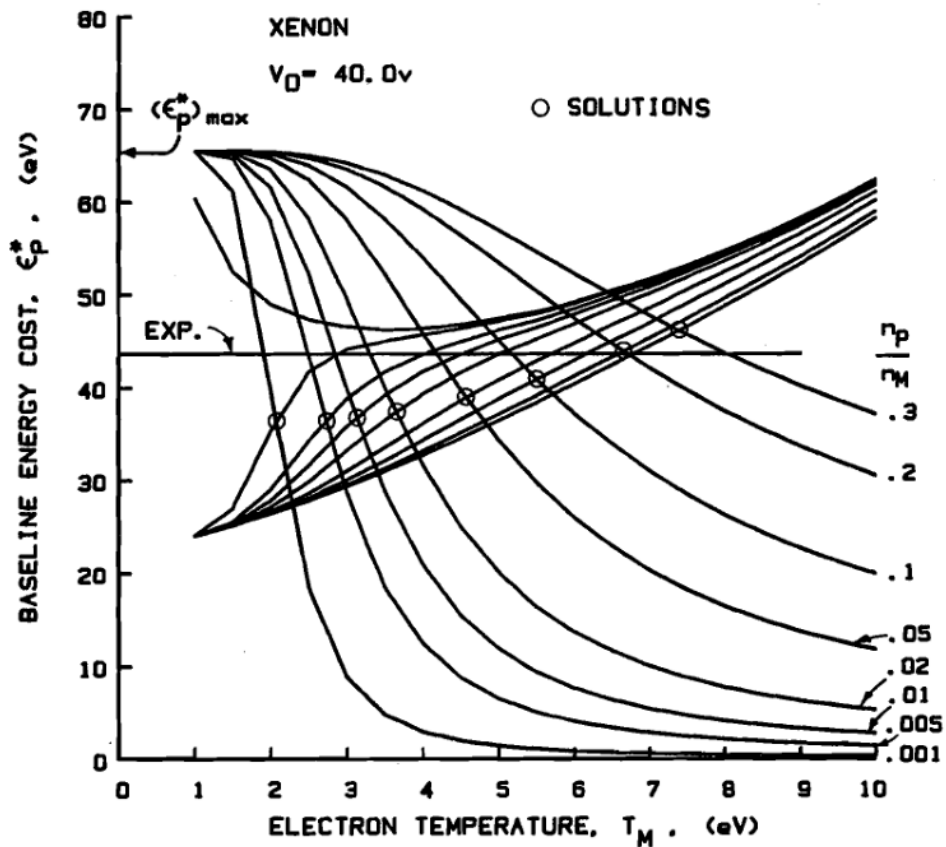
Figure 7.3: Solutions for the baseline plasma ion energy cost for xenon from [30].

it can be stated that both solutions are very similar although some differences can be found. For example, the solution in Fig. 7.2 has a positive offset with respect to that in Fig. 7.3.

Such differences might be due to disparities in the values of reaction rates for Maxwellian electrons and cross sections for primary electron collisions.

Despite such little variations, the code can be validated.

Down below, the effect of changing both control parameters (V_D and V_C) is studied.
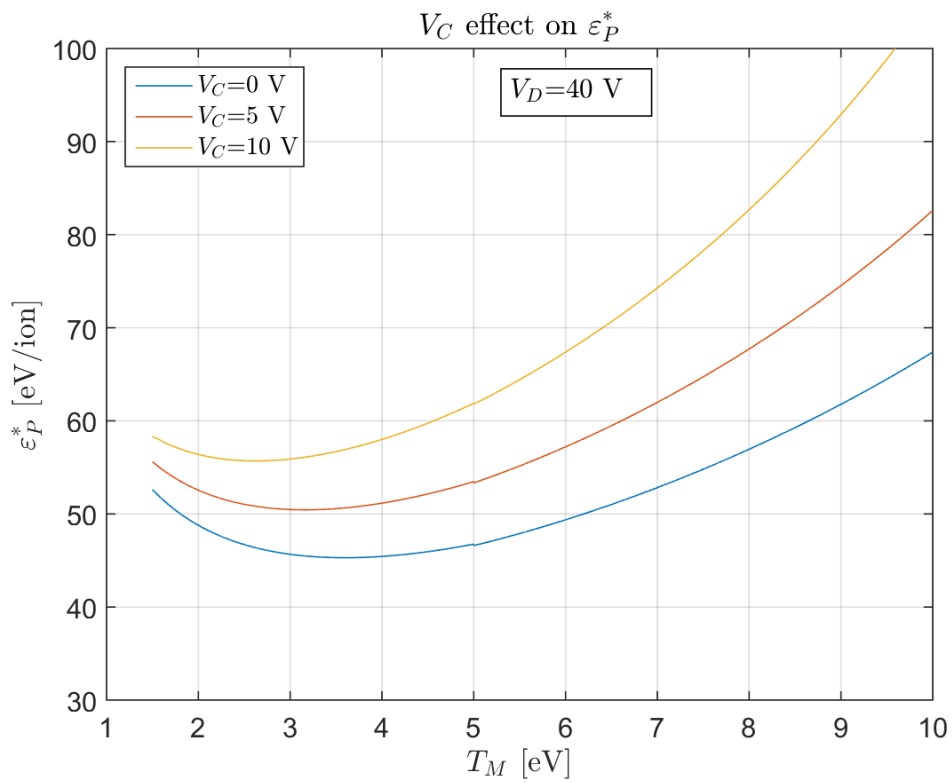
Figure 7.4: V_C effect on ϵ_P^* solution.
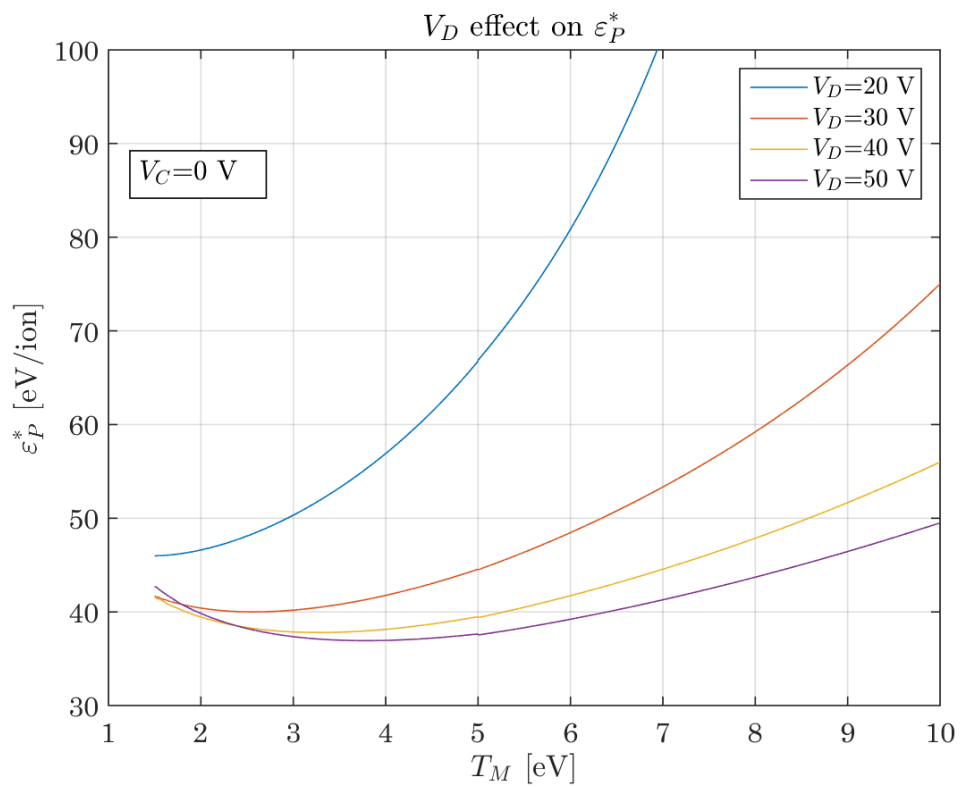
Figure 7.5: V_D effect on ϵ_P^* solution.

Fig. 7.4 shows the effect of increasing V_C at a constant V_D. As it could be expected, the baseline energy cost increases with V_C. Therefore, one must set this voltage as low as possible, but enough to guarantee that electrons are accelerated at a sufficient rate.

On the other hand, Fig. 7.5 shows the effect of varying V_D at a constant V_C. The most important effect on baseline energy cost is that, decreasing the discharge voltage, increases the slope of the curve. Despite this, at low values of Maxwellian electron temperature (2 to 5 eV), ε_P^* is nearly constant. Since typical values of T_M are in the mentioned range, the importance of V_D is not so important for determining ε_P^*. As it will be seen, the discharge voltage is chosen just enough for properly ionising the gas (30-40 V), because higher potentials lead to poor values of the extracted ion fraction (not desirable).

Once ε_P^* can be obtained for any operating point of the thruster,

7.1.2. Primary electron utilisation factor (C_0)

C_0 reflects the degree to which primary electrons interact with neutral atoms and, therefore, it should be as high as possible, since it would mean a lower plasma ion energy cost.

From Eq. 6.28, we know that,

$$C_0 = \frac{4\sigma_0' l_e}{e v_0 A_g \phi_0}$$

It can be noted that C_0 may be increased in several ways. First of all, it depends on the propellant properties. A gas characterised by a larger total inelastic collision cross section (σ_0') would result in a larger C_0. Moreover, heavier particles would result in lower neutral velocities (v_0) and, therefore, larger C_0.

Regarding the grids, the effect of their design in C_0 is taken into account through the parameters A_g and ϕ_0. The equation suggests that decreasing the area through which the beam is extracted (A_g), C_0 would be increased. Nevertheless, it would also result in a reduction of the extracted ion fraction, leading to an overall cut down in performance.

On the other hand, C_0 may also be increased by decreasing the grid transparency to neutrals (ϕ_0), which depends on the design and configuration of the grid system. This parameter may be modified by tailoring the holes size until optimise their configuration. The study of this parameter, even so, is out of the scope of the project and we will employ experimental values in our calculations.

Finally, one of the most important parameters in this equation is the primary electron containment length (l_e), which can be increased using an appropriate distribution and strength of the magnetic fields. In a cusped magnetic field thruster, being this the model corresponding to this study, electrons are lost to the anode through the cusps. Therefore, if the number of cusps at anode potential are decreased or the flux density at such points is increased, l_e would be enhanced. Unfortunately, this cannot be done indefinitely and there is a limit, where the operation of the discharge becomes unstable. Nevertheless, the determination of this parameter is beyond the scope of this theoretical model and typical values will be used.

7.1.3. Extracted ion fraction (f_B)

The extracted ion fraction is one of the most influential parameters when determining the beam ion energy cost. It is defined as the ratio of the beam current to the total ion current produced. Since the objective is not only generate ions efficiently but extract as many of them as possible, this ion fraction must be high in order to guarantee good performance of the thruster.

The calculation of f_B cannot be predicted with Brophy's theory and, therefore, it has been experimentally determined by measuring it for different thruster configurations.
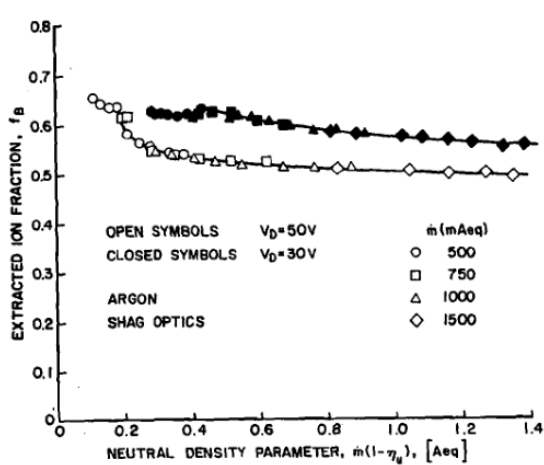

Figure 7.6: Effect of V_D on the extracted ion fraction for argon propellant [30].
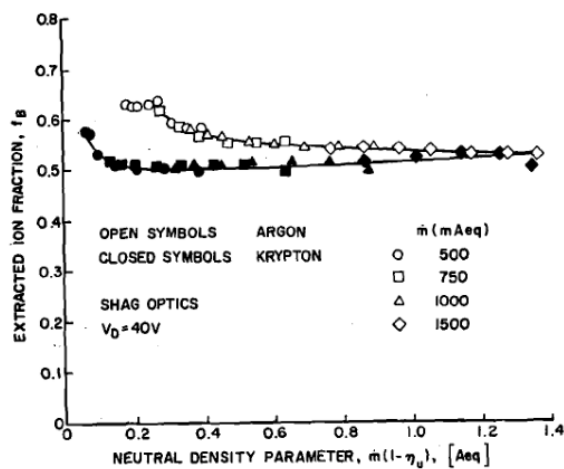
Figure 7.7: Effect of propellant on the extracted ion fraction [30].

Results obtained indicate that the extracted ion fraction is relatively independent of the neutral density parameter ($\dot{m}(1 - \eta_u)$) for a given thruster configuration (Fig. 7.6 and 7.7). That is, for a given design (size, geometry, magnetic fields), propellant and discharge voltage, f_B is constant. Results also show that, decreasing the discharge voltage, the extracted ion fraction is increased, so low V_D is required although it must be enough to properly ionise the propellant.

Moreover, it is known from other studies that, f_B is strongly dependent on magnetic fields and thruster geometry [30], although it will not be analysed in this model.

Fig. 7.6 and 7.7 indicates the values of the extracted ion fractions for ring cusped ion thrusters for different discharge voltages and propellants. They are kept between 0.5 and 0.6. For xenon propellant, results are not depicted, but it has a value of 0.5 for a V_D of 30 V [30].

7.1.4. Fraction of ion current to cathode surfaces (f_C)

This parameter reflects the ion current lost to the cathode potential surfaces and, therefore, low values are desirable.

A way of reducing this value is operating the discharge chamber at anode potential, instead of cathode potential. This is one of the reasons why the ion thruster typically works in such configuration. Moreover, it is highly dependent on the design of the thruster, but is constant for a given configuration. Therefore, it does not vary with the neutral density parameter or operating point.

As well as the extracted ion fraction, f_C must be found experimentally. Results obtained in ring cusped thrusters indicate that typical values are around 0.1.

7.1.5. Maxwellian electron temperature in bulk plasma (T_M)

Until now we have considered T_M as an independent variable, and the baseline ion energy cost has been calculated as a function of this parameter.

In this section, a new expression shall be derived in order to calculate the value of such temperature for a given operating point and configuration of the ion thruster.

To that end, an equation relating the Maxwellian electron rate factor with the baseline ion energy cost must be obtained.

$$Q_0^+ = <\sigma_+ v_e>_M = \frac{v_p \sigma_+' \left(\frac{V_D \sigma_0'}{\varepsilon_P^* \sigma_+'} - 1\right)}{\left(\frac{v_p V_D \sigma_0' V}{0.15 e \varepsilon_P^* v_0 v_B A_g^2 \phi_0 \phi_i}\right) \dot{m}(1 - \eta_u) - 1} \tag{7.12}$$

The detailed process to obtain Eq. 7.12 is available in [30].

As it has been stated in Section 7.1.1, the rate factor is a function of the temperature of the electrons, and such function is depicted in the next figure.
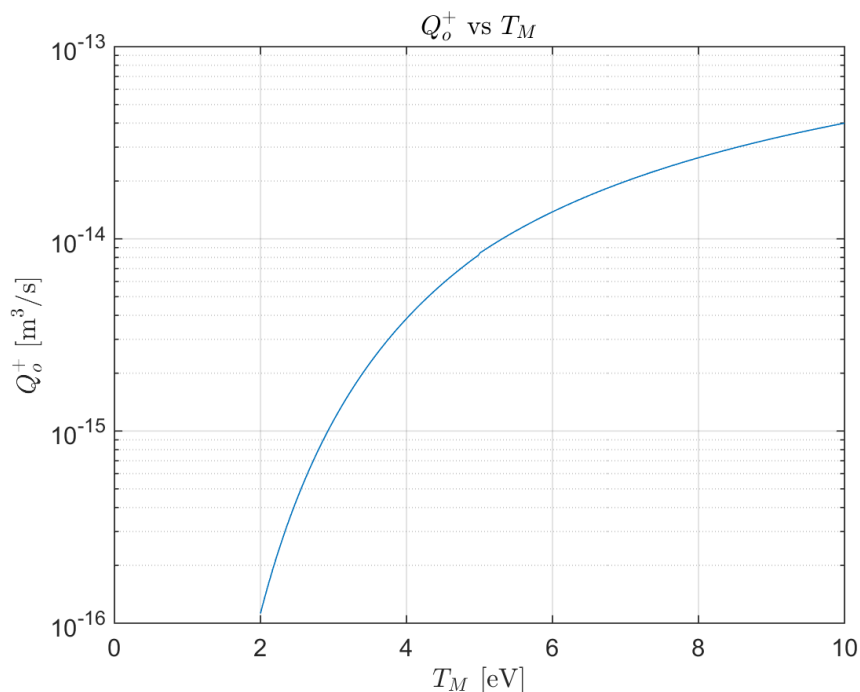
Figure 7.8: Ionisation rate factor Q_0^+ for xenon as a function of the electron temperature.

Combining Eq. 7.12 with the procedure employed in section 7.1.1, a further iterative process, which will be detailed in *Annex C.2* [21], may be followed in order to find a solution for T_M. Finally, we have a program that, given thruster's design parameters and its operating point, allows us to calculate a single solution for the baseline ion energy cost (ε_P^*) and, therefore, for the beam ion energy cost.

$$\varepsilon_P^* = f(V_D, V_C, f_C, f_B, \dot{m}, \eta_u, X) \tag{7.13}$$

$$\varepsilon_B = f(V_D, f_C, f_B, \dot{m}, \eta_u, C_0, \varepsilon_P^*) \tag{7.14}$$

X in Eq. 7.13 denotes all the design parameters that are fixed and do not depend on the operating point of the thruster, that is, propellant properties, geometric parameters, etc.

Thus, we should be able now to represent the different performance curves and assess the influence of each control parameter presented in Eq. 6.31.

7.2. Performance curves

A performance curve for the ion thruster is given by the next equation, firstly obtained in Section 6.2,

$$\varepsilon_B = \frac{\varepsilon_P^*}{f_B[1 - e^{-C_0 \dot{m}(1-\eta_u)}]} + \frac{V_D f_C}{f_B}$$

Next are exposed the results obtained. First of all, the effect of varying the extracted ion fraction on the performance is shown. The values of the parameters V_D, V_C, C_0, f_C, and $\dot{m}$ used to generate curves in Fig. 7.9 are specified in the legend.
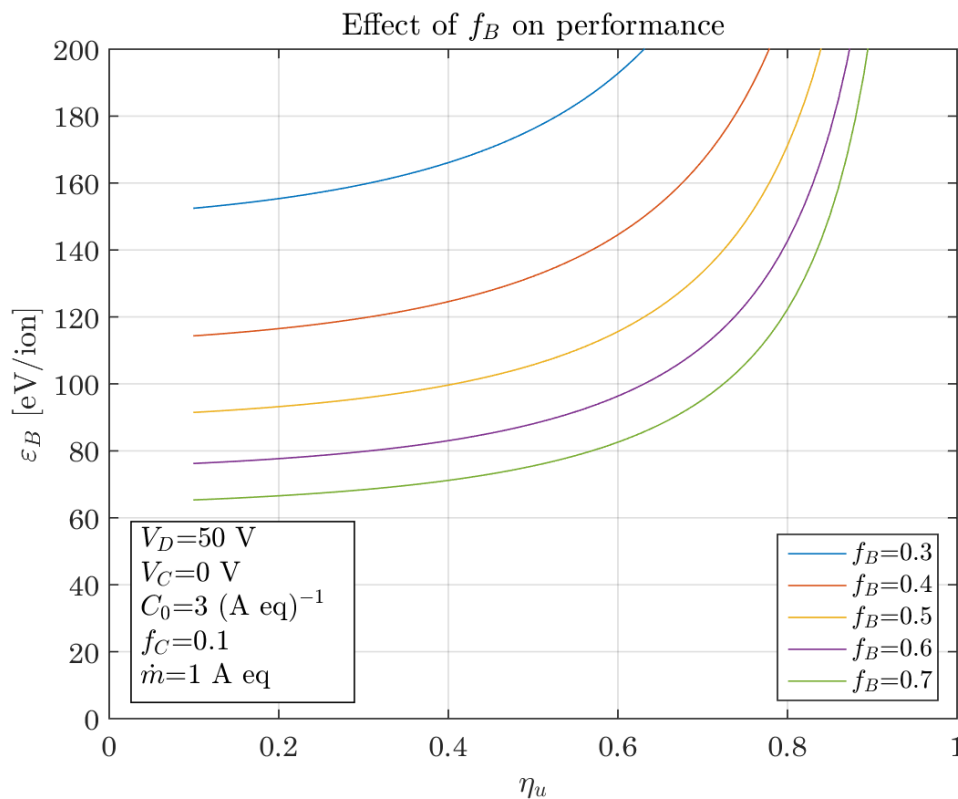
Figure 7.9: Effect of f_B on performance.

As it can be seen in Fig. 7.9, as f_B is increased, the ion energy cost is strongly reduced, so a value as large as possible is desirable. Nevertheless, the shape of the function is very similar in all cases. It is worth noting that, for low values of the extracted ion fraction, the differences are larger between consecutive data (i.e. 0.3 to 0.4). It can be concluded that, for the beam ion energy cost to be under 100 eV/beam ion, it is important to have, at least, an extracted ion fraction of 0.5.

Curves on Fig. 7.10 reflects the effect of changing the primary electron utilisation factor. Again, values of V_D, V_C, f_C, f_B and $\dot{m}$ are detailed in the legend.
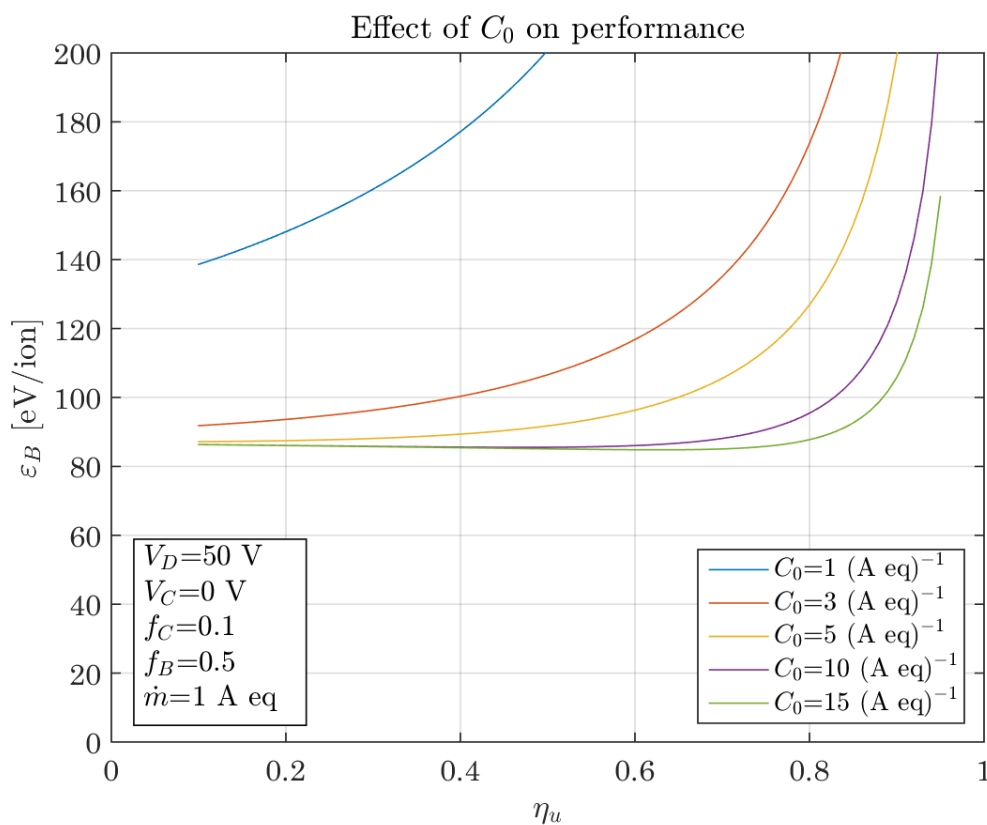
Figure 7.10: Effect of C_0 on performance.

As it can be seen in Fig. 7.10, the beam ion energy cost is reduced by increasing C_0. However, as this value gets larger, the function tend to a lower limit, which depends on the other parameters of the equation. In this case, the parameter we are studying not only determines the value of the beam ion energy cost, but it also determines the shape of the curves. More sharply defined "knees" (for high η_u values) correspond to larger values of C_0. Therefore, it can be concluded that large values of the primary electron utilisation factor are desirable,

although at high values, the differences on performance curves for different values of C_0 are not very important. In order to guarantee optimum thruster's performance, minimum values around $5\ A^{-1}$ are needed.

The effect of the propellant flow rate is shown in Fig. 7.11. The values of V_D, V_C, C_0, f_C, and f_B used to plot the curves are detailed in the legend.
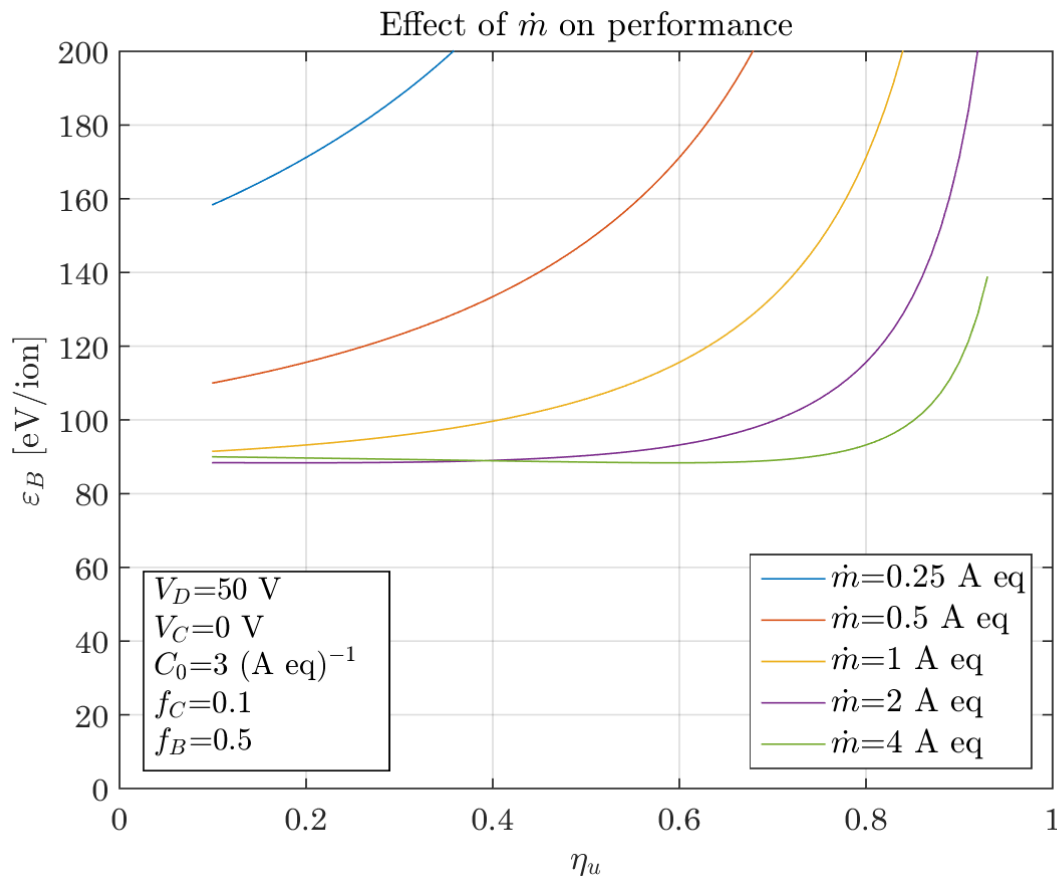
Figure 7.11: Effect of $\dot{m}$ on performance for $C_0 = 3\ (A\ eq)^{-1}$.

The curves obtained suggest that larger values of $\dot{m}$ are required to obtain better performance. Moreover, as well as it happens with C_0, the curves tend to a lower limit which is independent of $\dot{m}$. Despite this, the flow rate is limited by the accelerator system capacity to extract the ion current directed toward it and cannot be indefinitely increased.

With the next figure, we can assess the effect of the propellant flow rate for larger values of C_0.
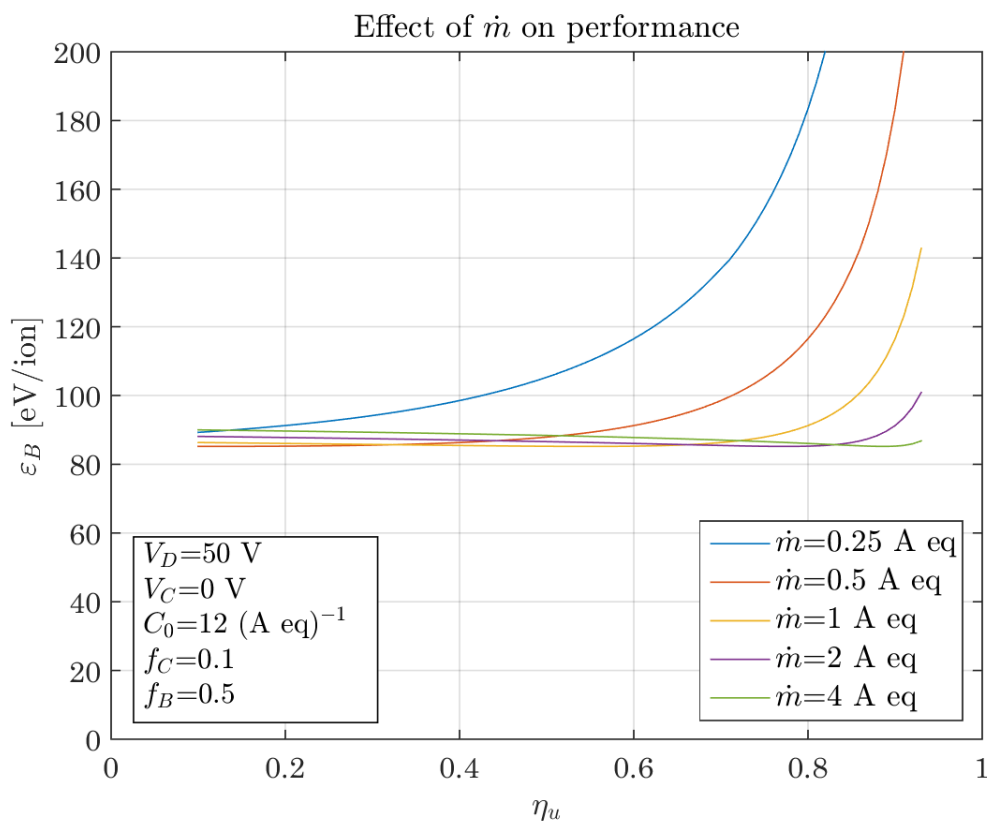
Figure 7.12: Effect of $\dot{m}$ on performance for $C_0 = 12\ (A\ eq)^{-1}$.

It can be drawn from comparing results exposed in both figures 7.11 and 7.12, that changes in the propellant flow rate are less important when the thruster is operating with large values of C_0. The "knees" are more sharply defined and, therefore, penalty in thruster's performance due to changes in $\dot{m}$ is smaller.

The effect of V_D is shown in Fig. 7.13.

As we can see, for high values of V_D, the thruster's performance does not depend on such potential. However, for low values (20 V), the curve is shifted up. This may be due to the shape of the ε_P^* function, which, for small values of V_D, changes its slope considerably, not being, therefore, constant at a given range of electron temperatures T_M. We can conclude that optimum values of V_D would be from 30 V upwards.

Finally, the effect of V_C on performance is exhibited in Fig. 7.14. This parameter does not appear in equation 6.31, but it has a strong effect on the baseline ion energy cost and, therefore, in the beam ion energy cost as well.
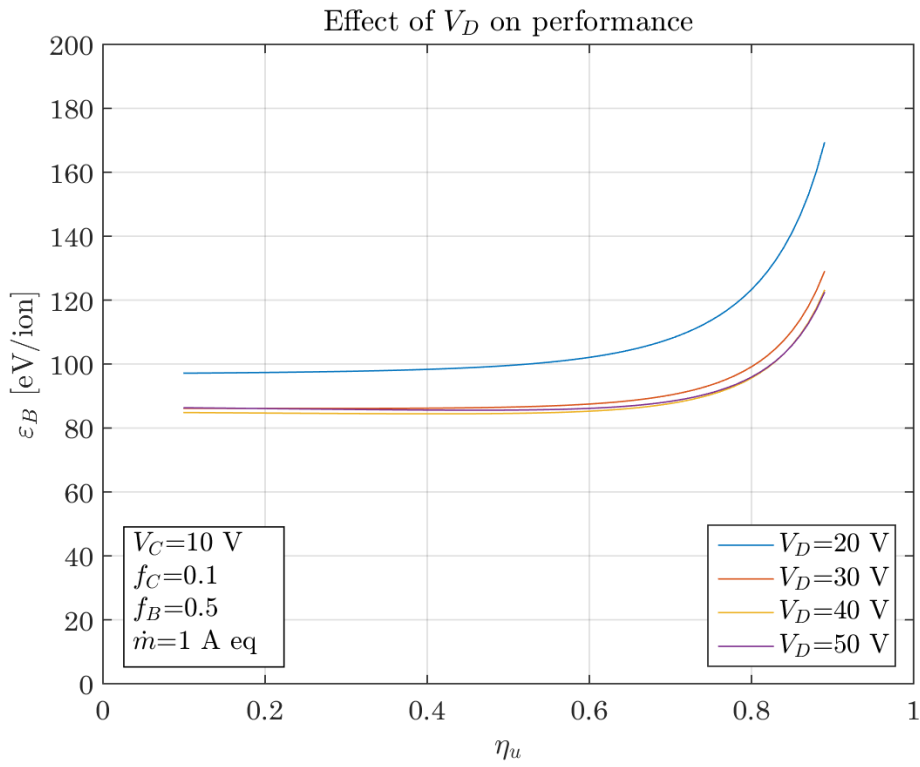
Figure 7.13: Effect of V_D on performance.
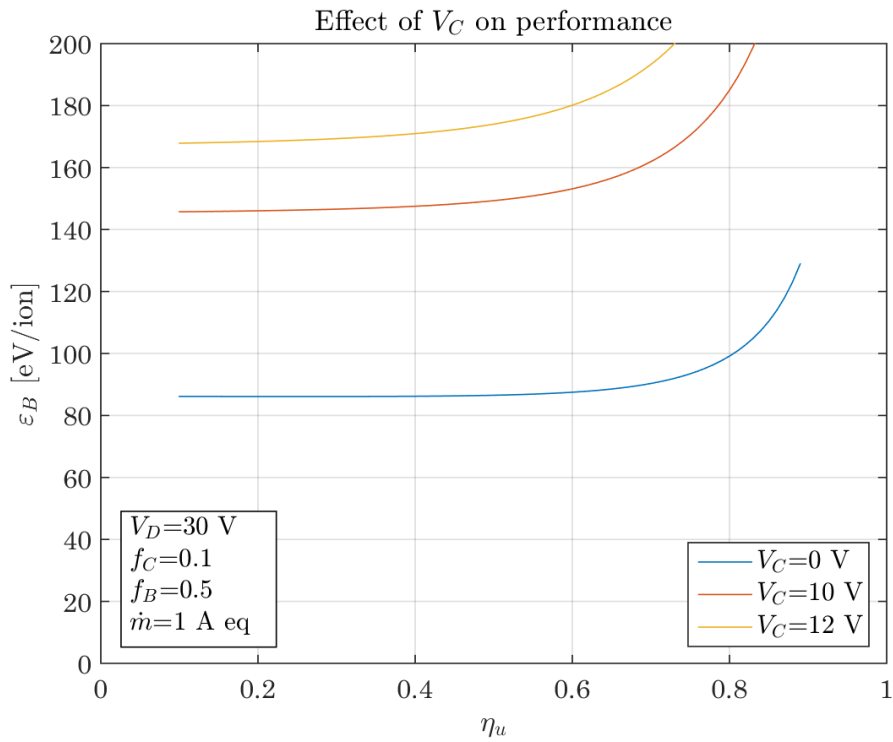
Figure 7.14: Effect of V_C on performance.

Looking at curves in last figure, it can be confirmed the importance of a low value of V_C. As it has been said in Chapter 5, the operating potential of the hollow cathode has a strong effect on the discharge chamber's performance. Increasing V_C shifts the solutions up.

Chapter 8.   Validation

In this section, the results obtained in the previous study (Section 7.2) will be validated.

To that end, we will make use of experimental data provided by the National Aeronautics and Space Administation, in [32] and [33]. These papers contain the characteristics of operation with xenon of Kaufman type ion thrusters at different operation points.

Since our analysis enables us to determine the performance of a given ion thruster $(\varepsilon_B = f(\eta_u))$, we will compare experimental data with our results, obtained for the same operating conditions.

First of all, data from [32] is presented in Table 8.1.

$\dot{m}$ [A]	η_{u_C}	V_D [V]	β	$\varepsilon_{B_{exp}}$ [eV/ion]
1.18	0.875	38.4	0.9215	209
1.34	0.933	45.2	0.8993	228
2.31	0.905	36.1	0.9215	158
2.57	0.954	38.1	0.9027	166
2.92	1.019	42.9	0.8566	190
3.43	0.915	27.9	0.9215	177
3.67	0.947	28.7	0.9095	190
4.02	0.991	31.2	0.8873	196
4.22	1.016	33.5	0.8686	205

Table 8.1: J-Series line-cusp ion thruster's performance with xenon propellant. Experimental data [32].

Measurements in [32], show the J-Series ion thruster's performance. It is a line-cusp ion thruster. Therefore, it has not the optimum magnetic configuration in order to maximise the containment length of electrons in the ionisation chamber. Hence, the primary electron utilisation factor (C_0) has a low value, as indicated in Section 7.1.2, leading to high ionisation costs (Table 8.1).

To simulate the results, the assumed containment length of this engine has been,

$$l_e = 0.5 \, m$$

Moreover, such ion thruster is fitted with a SHAG optics system for the extracting grids, whose transparencies are, for the grid screen and accelerator grids, respectively [30],

$$\phi_s = 0.68 \qquad\qquad \phi_a = 0.3$$

Taking into account these parameters, leads to a primary electron utilisation factor near to (using Eq. 6.28),

$$C_0 = 2 \, (A \, eq)^{-1}$$

Although C_0 is a function of the discharge and hollow cathode voltages, it keeps nearly constant for a given ion thruster design.

Before exposing our results, we must highlight that, as it was stated in Section 7.1.3, the extracted ion fraction is constant for a given design, but varies with the discharge voltage. Therefore, for values of V_D between 45.2 V and 36.1 V, f_B has been assumed to be equal to 0.5. For lower values of V_D, f_B decreases (Fig. 7.6) and, for discharge voltages under 36.1 V, we will consider an extracted ion fraction of 0.35.

Finally, we should mention that our model neglects the doubly charged ion current, in contrast to results provided by [32] and [33]. Since their definition of propellant utilisation efficiency is slightly different, their η_u's can reach values larger than the unity, as we can see in Table 8.1. In order to compare equivalent utilisation efficiencies, those provided experimentally must be multiplied by a correction factor β (given in tables 8.1 and 8.3),

$$\eta_u = \eta_{u_c}\beta \tag{8.1}$$

β is defined as follows [28],

$$\beta = \frac{1 + \dfrac{r}{2}}{1 + r}$$

Where r is the doubly-to-singly charged ion current ratio, which is not considered in our preliminary analysis,

$$r = \frac{J_B^+}{J_B^{++}}$$

The results obtained with the model developed in Chapter 7, for the same operating conditions as in Table 8.1, are presented below.

$\dot{m}$ [A]	V_D [V]	η_u	f_B	ε_B [eV/ion]	$\varepsilon_{B_{exp}}$ [eV/ion]	Error [%]
1.18	38.4	0.806	0.5	208	209	0.5
1.34	45.2	0.839	0.5	242	228	6.1
2.31	36.1	0.834	0.5	155	158	1.9
2.57	38.1	0.861	0.5	173	166	4.2
2.92	42.9	0.873	0.5	188	190	1.1
3.43	27.9	0.843	0.35	177	177	0.0
3.67	28.7	0.861	0.35	191	190	0.5
4.02	31.2	0.879	0.35	200	196	2.0
4.22	33.5	0.882	0.35	208	205	1.5

Table 8.2: Line-cusp ion thruster's performance calculated with the model.

Next, experimental data, retrieved from [33], is shown.

$\dot{m}$ [A]	η_{u_C}	V_D [V]	β	$\varepsilon_{B_{exp}}$ [eV/ion]
2.07	0.682	29.4	0.985	90.5
3.51	0.889	32.8	0.965	91.8
4.41	0.996	35.6	0.940	94.6

Table 8.3: Ring-cusp ion thruster's performance. Experimental data [33].

Table 8.3 shows the performance of a ring-cusp ion thruster. This engine has significant improvements in the discharge chamber over the line-cusp thruster analysed above. It has strong boundary ring-cusp magnetic fields, a diverging field in the cathode region, and a nearly field-free volume upstream of the ion extraction system. This allows to increase the electron

containment length, leading to primary electron utilisation factors in the order of 10 (A eq.)$^{-1}$. Regarding the extracted ion fraction, Brophy's Theory document [30] provides an experimental value for ring-cusp thrusters using xenon as propellant, $f_B = 0.5$. This is valid for the V_D range considered [30].

The results obtained with the model developed in Chapter 7, for the same operating conditions as in Table 8.3, are presented below.

$\dot{m}$ [A]	V_D [V]	η_u	f_B	ε_B [eV/ion]	$\varepsilon_{B_{exp}}$ [eV/ion]	Error [%]
2.07	29.4	0.672	0.5	89.1	90.5	1.5
3.51	32.8	0.858	0.5	93.5	91.8	1.9
4.41	35.6	0.936	0.5	98.5	94.6	4.1

Table 8.4: Ring-cusp ion thruster's performance calculated with the model.

In order to assess the reliability of the model, the mean error of the results has been reported. It has been computed as the average of the individual errors of each sample.

$$Individual\ error\ \% = \frac{\left|\varepsilon_{B_{exp}} - \varepsilon_B\right|}{\varepsilon_{B_{exp}}} \cdot 100$$

The average error is,

$$Average\ error = 2\ \%$$

We can conclude then, that validity is supported by the results obtained in this section, since 2 % is an affordable error for a preliminary thruster's performance analysis.

Chapter 9.   Actuations

Once we have developed a model to obtain the performance of a given thruster, we may also analyse a specific space propulsion mission in order to optimise the engine operation.

9.1.   Performance parameters effect on mission optimisation

Until now, we have been able to calculate the beam ion energy cost (ε_B) as a function of the propellant utilisation efficiency (η_u). Therefore, the engine could work at different operating points (different η_u's). However, in this section we will see it can be found an optimum η_u for every singular mission.

To that end, firstly, we will study the effect of different parameters of the thruster on the payload mass fraction, defined later on. This will be done making use of data from a generic simplified mission, whose specifications are listed below,

$$\Delta v = 6.000 \ \frac{km}{s}$$

$$t = 200 \ days$$

Δv is the total change of velocity provided by the ion thruster over the manoeuver and t is the overall time needed to carry out the mission.

9.1.1.   Payload mass fraction determination

Considering a spacecraft of mass (m), whose propellant leaves the engine at an exhaust velocity u (considered constant over time), we can express the accelerating force of the propellant as follows,

$$m \frac{dv}{dt} = \frac{J_B m_i}{e} u \tag{9.1}$$

Where the right hand side term constitutes the thrust of our ion engine, since only high speed particles contribute to this force. $\frac{dv}{dt}$ is the acceleration provided by the thruster in the direction of the exhaust stream.

Taking into account that,

$$J_B = \dot{m}\eta_u = \dot{m}_p \frac{e}{m_i}\eta_u = -\frac{dm}{dt}\frac{e}{m_i}\eta_u \tag{9.2}$$

where $\dot{m}_p$ is the propellant mass flow rate [kg/s], Eq. 9.2 can be rewritten as,

$$m\frac{dv}{dt} = -\frac{dm}{dt}\eta_u u \qquad \rightarrow \qquad dv = -\eta_u u \frac{dm}{m} \tag{9.3}$$

The last expression can be integrated, yielding the rocket equation modified with η_u.

$$\frac{M_f}{M_i} = e^{-(\Delta v/\eta_u u)} \tag{9.4}$$

It gives us the ratio of final spacecraft mass (M_f) to initial mass (M_i) as a function of three characteristic parameters: Δv, η_u and u. Recognising that the propellant mass (M_{p_0}) is,

$$M_{p_0} = M_i - M_f \tag{9.5}$$

we also can write,

$$\frac{M_{p_0}}{M_i} = 1 - e^{-(\Delta v/\eta_u u)} \tag{9.6}$$

It is assumed that the power plant has a mass M_g, and it can be expressed as the sum of a part proportional to the power generated (P_g) and another one independent of the power level (M_{g_0}),

$$M_g = \alpha P_g + M_{g_0} \tag{9.7}$$

Being P_g given by,

$$P_g \eta_t = \frac{1}{2}\dot{m}_p u^2 \eta_u \tag{9.8}$$

where η_t is the thruster electrical efficiency. Again, assuming a constant thruster's rate of operation ($u = ct$ and $\eta_t = ct$), Eq. 9.8 can be integrated yielding,

$$P_g = \frac{M_{p_0} u^2 \eta_u}{2 \eta_t t} \tag{9.9}$$

Ellectrical efficiency is defined as follows,

$$\eta_t = \frac{1}{1 + \dfrac{\varepsilon_B}{V_N}} \tag{9.10}$$

It must be highlighted that Eq. 9.10 only considers discharge chamber losses. It is not the overall engine efficiency. The term V_N is the net accelerating voltage, firstly introduced in Section 5.2, and can be related to the exhaust velocity by considering that the whole power provided by the potential difference between the grids is used to accelerate the ions,

$$eV_N = \frac{1}{2} m_i u^2 \tag{9.11}$$

The value of the exhaust velocity (and specific Impulse ($I_{sp} = u/9.8$)) as a function of the net voltage, for xenon propellant, is shown in Fig. 9.1.
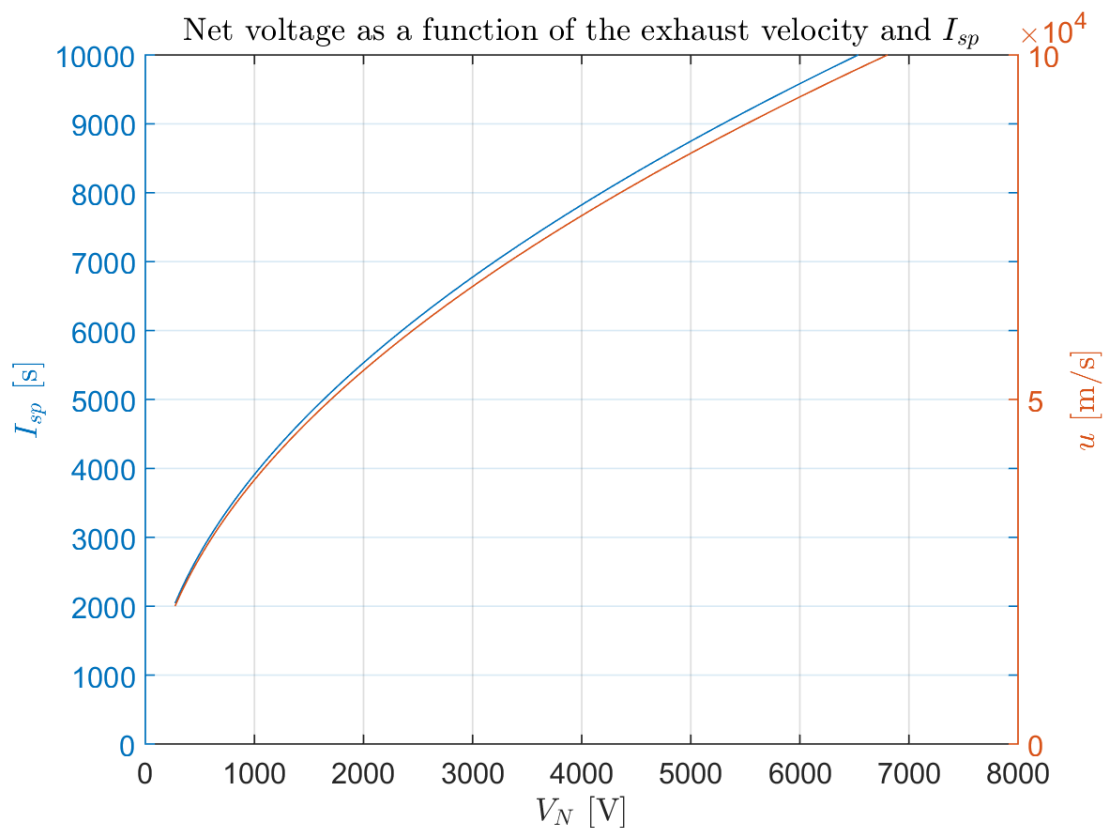

Figure 9.1: V_N as a function of u and I_{sp}.

Considering, for simplicity, that the final mass is comprised of the payload mass (M_l) and the power plant mass (M_g), we can obtain the following equations,

$$\frac{M_f}{M_i} = \frac{M_l}{M_i} + \frac{M_g}{M_i} \tag{9.12}$$

$$\frac{M_g}{M_i} = 1 - \frac{M_{p_0}}{M_i} + \frac{M_l}{M_i} \tag{9.13}$$

Finally, combining Eqs. 9.4, 9.6 and 9.9 to 9.13, yields,

$$\frac{M_l}{M_i} = e^{-(\Delta v/\eta_u u)} - \frac{\alpha u^2 \eta_u}{2t}\left(1 + \frac{2e\varepsilon_B}{m_i u^2}\right)\left(1 - e^{-(\Delta v/\eta_u u)}\right) - \frac{M_{g_0}}{M_i} \tag{9.14}$$

Eq. 9.14 indicates the value of the payload mass fraction $\left(\frac{M_l}{M_i}\right)$ as a function of the specific mission requirements ($\Delta V, t$), the beam ion energy cost (ε_B), the power plant specific mass (α), the power plant mass fraction independent of the power level $\left(\frac{M_{g_0}}{M_i}\right)$, the charge-to-mass ratio of the beam ions (e/m_i) and the operating point of the thruster (η_u, u). It should be noted that ε_B is also a function of the propellant utilisation efficiency through Eq. 6.31.

From all the parameters mentioned above, η_u and u can be easily modified given a thruster configuration and a mission design. Therefore, Eq. 9.14 might be doubly maximised.

First of all, we can calculate, for each propellant utilisation efficiency (η_u), the exhaust velocity that optimises the payload mass fraction. As we know the dependence of $\frac{M_l}{M_i}$ with u, we can set the analytical derivative of Eq. 9.14 (with respect to exhaust velocity), equal to zero and solve the resulting expression for u. Thus,

$$\frac{d\left(\frac{M_l}{M_i}\right)}{du} = \frac{ae^{-a/u}}{u^2} - 2bu\left(1 - e^{-a/u}\right) + \frac{abe^{-a/u}(c + u^2)}{u^2} = 0 \tag{9.15}$$

where,

$$a = \frac{\Delta v}{\eta_u} \qquad\qquad b = \frac{\alpha \eta_u}{2t} \qquad\qquad c = \frac{2e\varepsilon_B}{m_i}$$

Due to the complexity of Eq. 9.15, it must be numerically solved by means of an iterative process, detailed in *Annex C.3* [21].

Solving Eq. 9.15 yields a solution for u as a function of η_u. That is, for a given thruster configuration and specific mission, we can find for every η_u the exhaust velocity (or I_{sp}) that optimises the payload mass fraction. These results are depicted in Fig. 9.2. The values of the parameters used to generate the curve are shown in the legend.

$$I_{sp} \text{ vs } \eta_u$$

$$\Delta v = 6000 \text{ m/s} \quad C_0 = 5 \text{ (A eq)}^{-1}$$
$$t = 200 \text{ days} \quad \dot{m} = 1 \text{ A eq}$$
$$\alpha = 0.04 \text{ kg/W} \quad V_D = 40 \text{ V}$$
$$f_B = 0.5 \quad V_C = 0 \text{ V}$$
$$f_C = 0.1$$
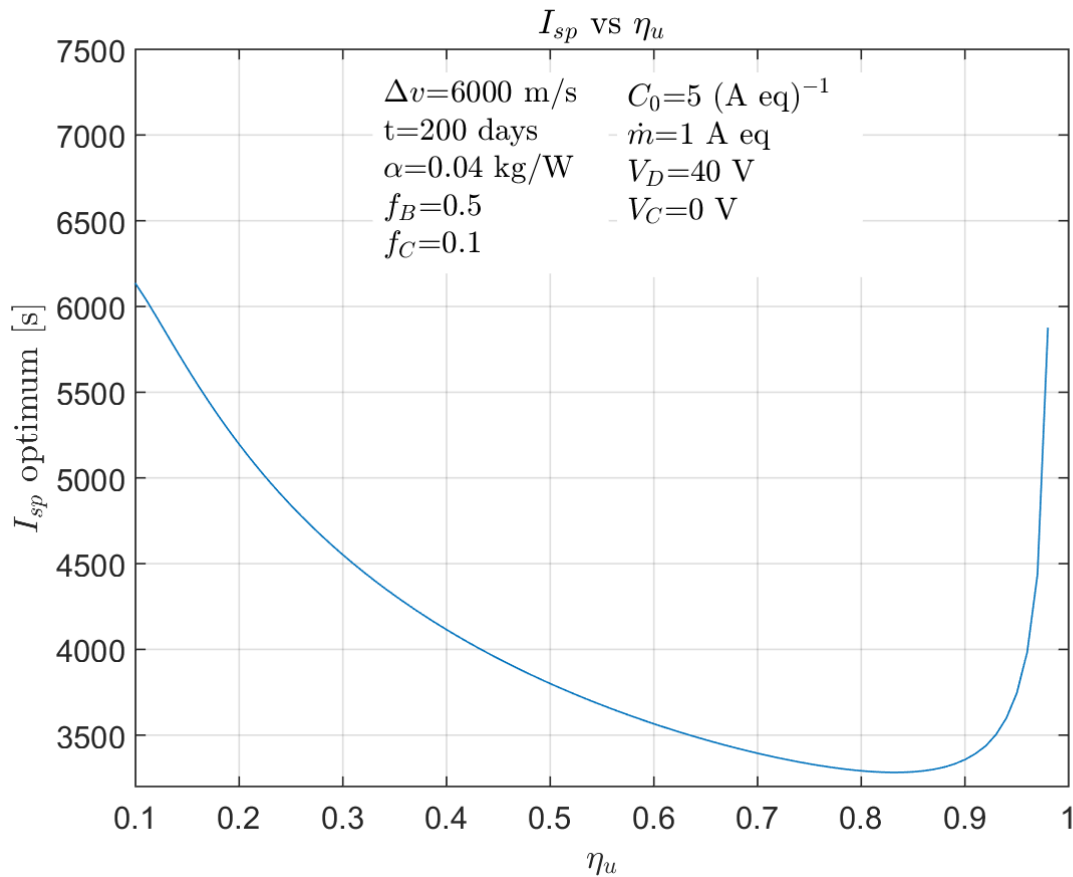
Figure 9.2: Specific impulse as a function of the propellant utilisation efficiency for a specific configuration.

Finally, once the value of the exhaust velocity (u) for an optimum payload mass fraction has been achieved for each η_u, the resulting expression shows another maximum when representing $\frac{M_l}{M_i} = f(\eta_u)$ (Fig. 9.3). It corresponds to the propellant utilisation efficiency that maximises the payload mass fraction, again. In the next figure, the initial propellant mass fraction $\left(\frac{M_{p_0}}{M_i}\right)$ and the power plant mass fraction $\left(\frac{M_g}{M_i}\right)$, along with the doubly optimised payload

fraction $\left(\frac{M_l}{M_i}\right)$ have been plotted. The parameters used to generate the curves are indicated in the legend.
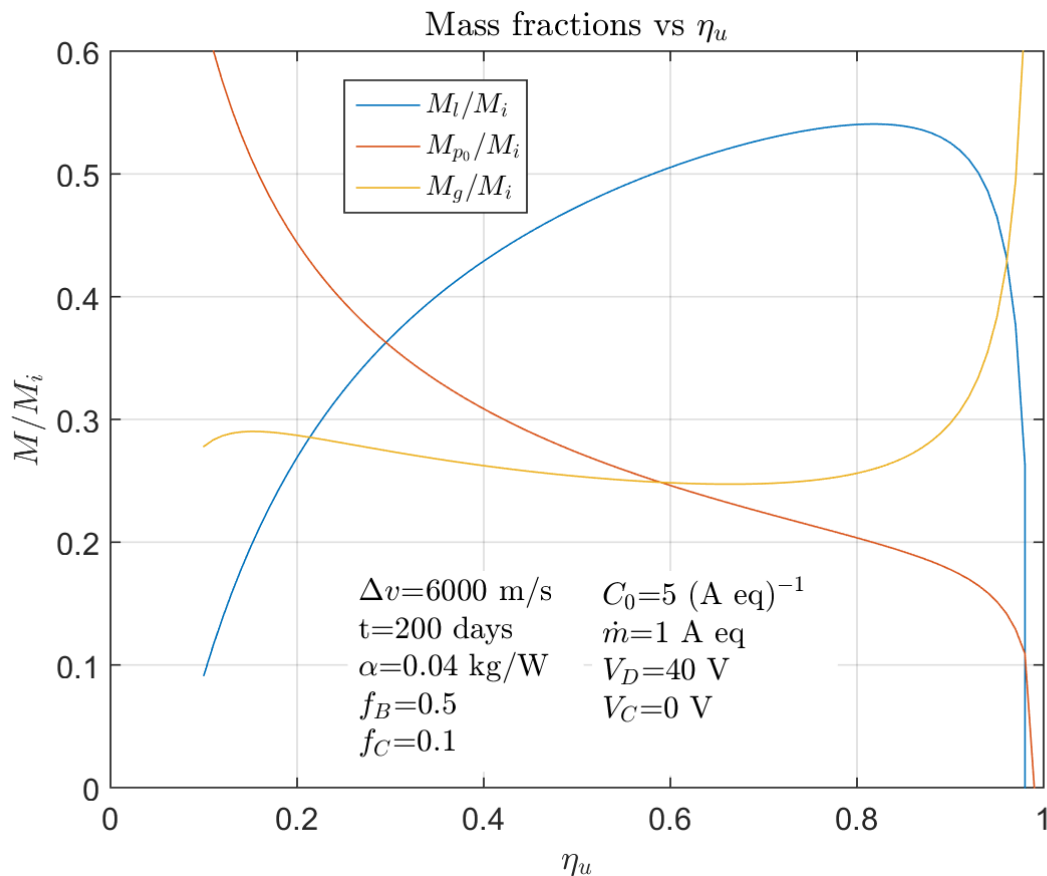
Figure 9.3: Payload, propellant and power plant mass fractions as a function of η_u.

As expected, the $\frac{M_l}{M_i}$ curve in Fig. 9.3 shows a maximum. This point indicates the propellant utilisation efficiency (η_u) that defines the optimum thruster performance curve corresponding to the specific mission.

We should note that the sum of the three curves are equal to unity, as stated in Eq. 9.13. Moreover, as η_u is increased, $\frac{M_{p_0}}{M_i}$ is reduced, since a larger part of the propellant is accelerated through the grids. Regarding the power plant mass fraction, we can see that it decreases with η_u for small values of the latter. It is due to a decreasing optimum exhaust velocity, as it is shown in Fig. 9.2. However, at high values of η_u, the power plant mass ratio increases rapidly due to an increment in beam ion energy cost (Fig. 7.10).

The following section will focus on the effect of different parameters in Eq. 9.14.

9.1.2. Effect of specific power plant mass (α)

First of all, the specific power plant mass (α) will be analysed.
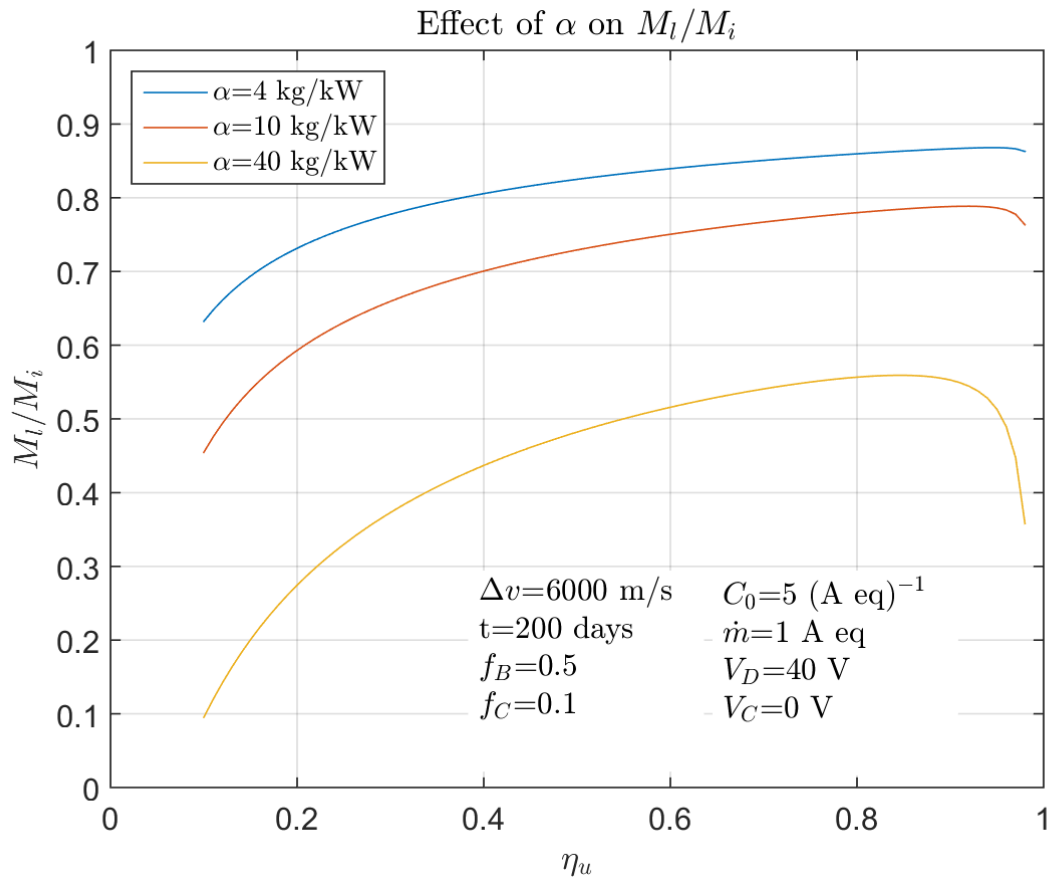
Figure 9.4: Specific power plant mass effect on payload mass fraction.

As we can see in Fig. 9.4, at lower values of α, the payload mass fraction is larger. In addition $\frac{M_l}{M_i}$ remains nearly unchanged for most values of the propellant utilisation efficiency. On the other hand, besides allowing smaller payloads, high α make the curves more sensitive to changes in η_u.

If we repeat the process for different values of specific power plant masses, we realise that the value at which optimum η_u occurs is a function of α. The results obtained are shown in Fig. 9.5.

Figure 9.5: η_u for doubly optimised payload mass fraction as a function of the specific power plant mass.
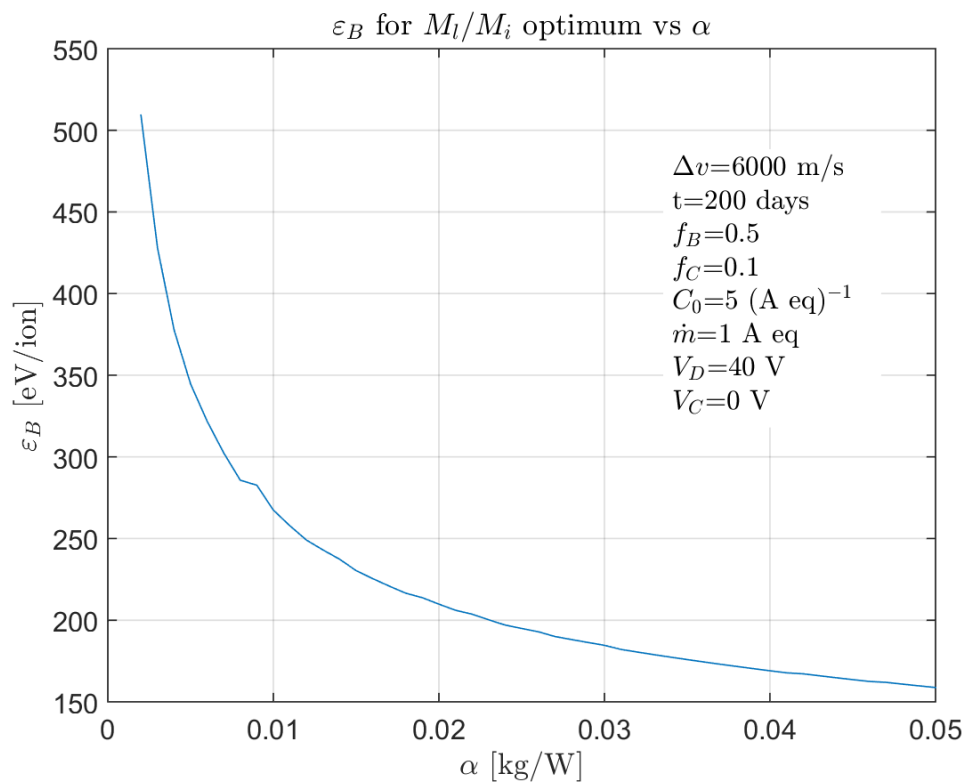
Figure 9.6: Ionisation costs for optimum M_l/M_i as a function of specific power plant mass.

In Fig. 9.5 we can see that the optimum propellant utilisation efficiency increases by decreasing the specific power plant mass. It could seem desirable since that woul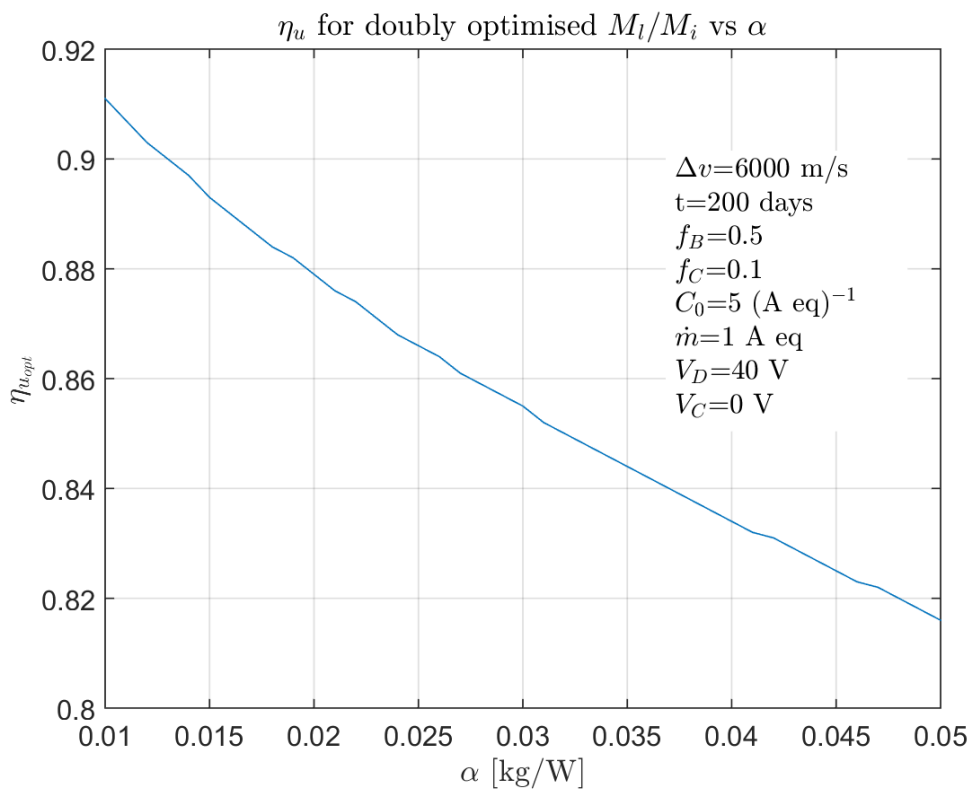d mean higher payload mass fractions. Nevertheless, if we take a look at the beam ion energy cost at which every case occurs, we see that ε_B is modified as shown in Fig. 9.36.

At very small α values, the ionisation cost is very high, and so η_u also is, leading to poorer electric efficiencies, which depend on ε_B, as it is stated in Eq. 9.10. The figure that follows, represents how η_t varies as a function of η_u for different values of net voltage (V_N),
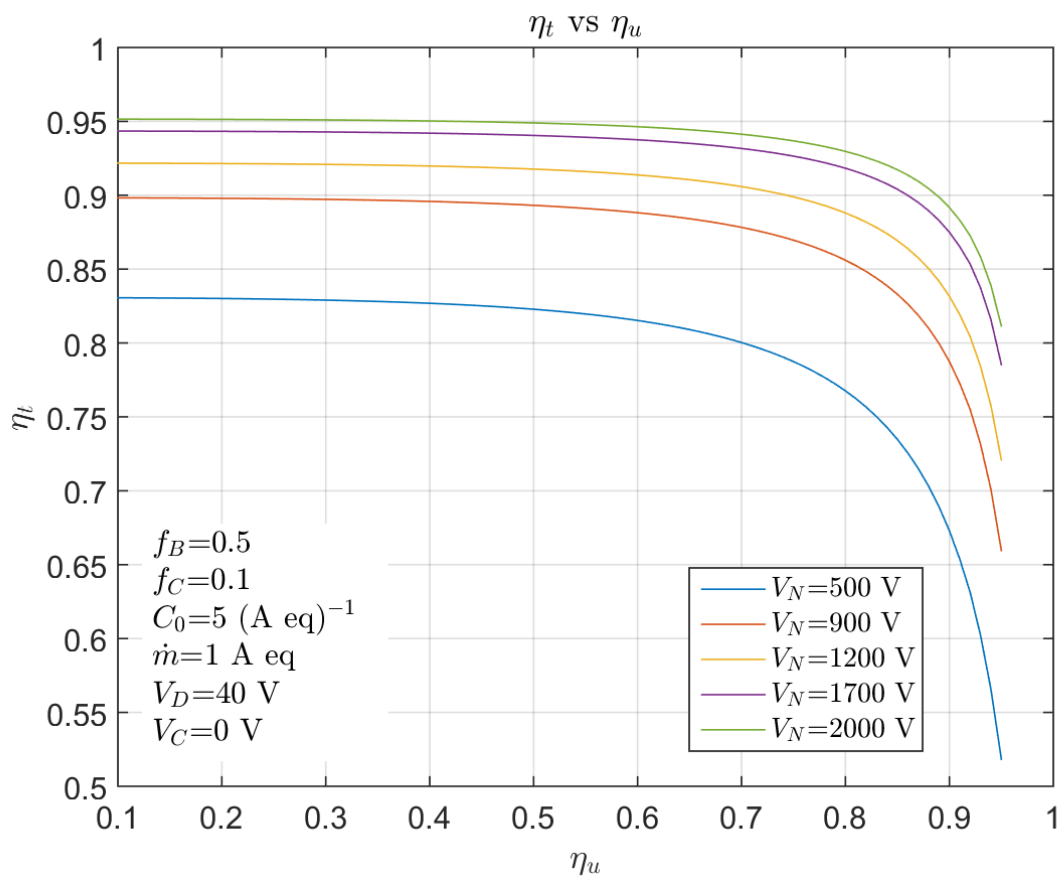
Figure 9.7: Electric efficiency as a function of propellant utilisation efficiency for different net voltages.

As we can see, electric efficiency rapidly declines at high propellant utilisation efficiencies, requiring higher power consumptions. Therefore, we should find a trade-off between an optimal payload mass fraction and an optimal electric efficiency.

Moreover, the effect of α on the optimum specific impulse is shown in Fig. 9.8. We can see that $I_{sp_{opt}}$ increases as the specific power plant mass is decreased. This is advantageous to some extent, because for very small values of α, a large exhaust velocity is needed to optimise the thruster. Such operating points would require too high net voltages (Fig. 9.1). As stated in Section 5.2.1, it is limited due to breakdown or shorting phenomena between the grids.
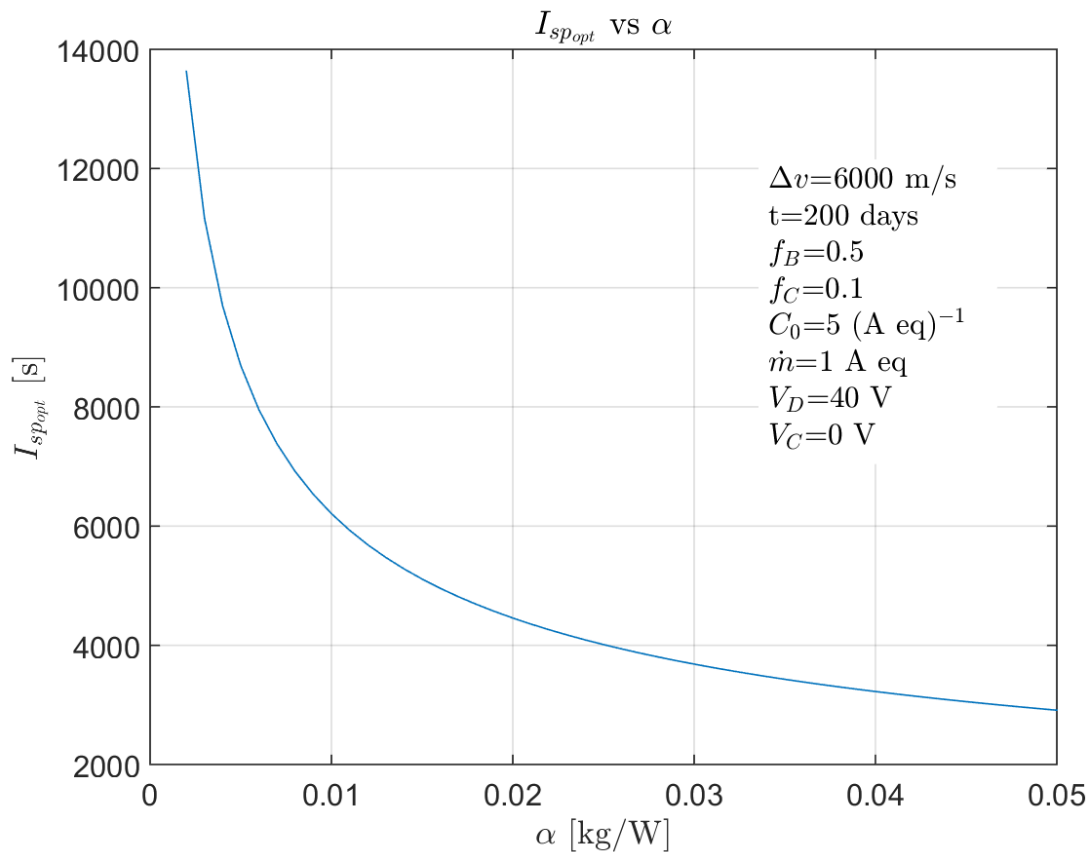
Figure 9.8: Optimum specific impulse as a function of specific power plant mass.

Next, the effect of the thruster performance parameters (C_0, f_B) shall be analysed.

9.1.3. Effect of primary electron utilisation factor (C_0)

Hereafter, we can see the consequences of using different C_0's.
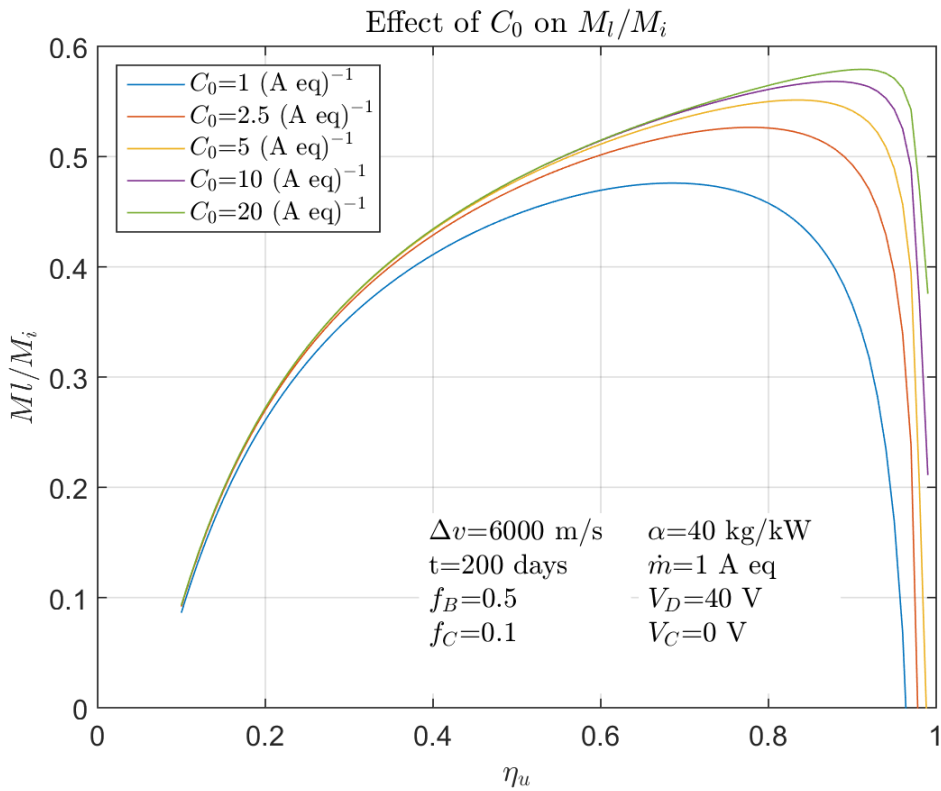
Figure 9.9: Effect of C_0 on payload mass fraction curves.
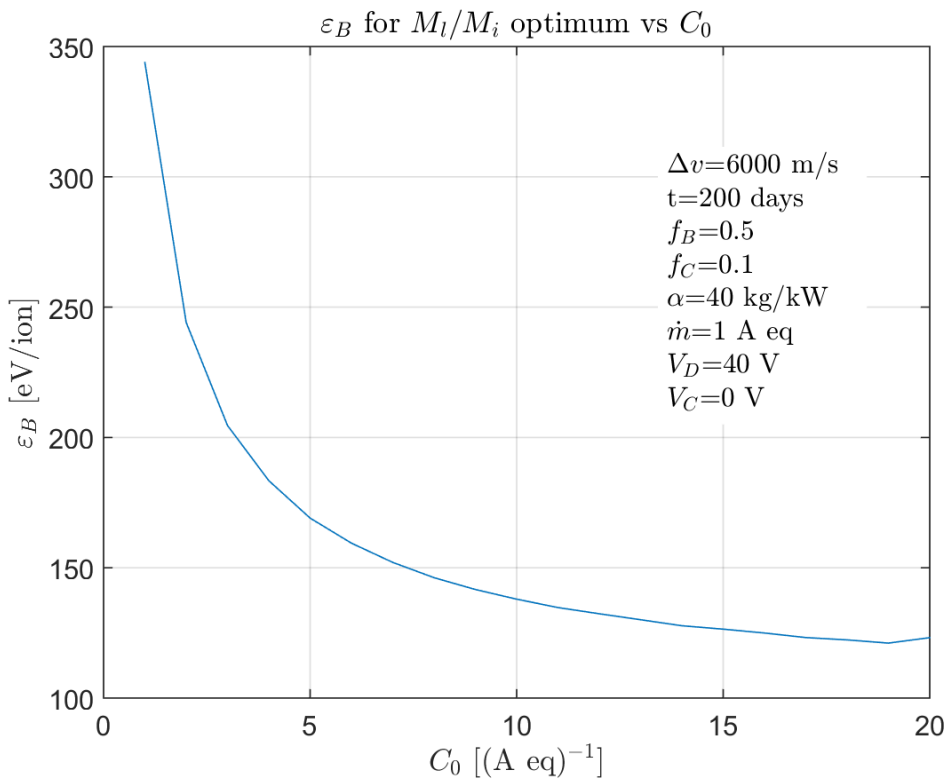
Figure 9.10: Ionisation costs for optimum M_l/M_i as a function of C_0.

The parameter studied in Fig. 9.9 basically defines the shape of the curves, emphasising the "knees" at the maximums. Larger values lead to higher maximum payload mass fractions. Moreover, the propellant utilisation efficiency at which that occurs, increase with higher C_0's. Again, the variation of this parameter concerns ionisation costs, as shown in Fig. 9.10.

This time, higher optimum η_u's entail lower beam ion energy costs. Therefore, it is clearly desirable large values of C_0. However, it must be noted that, from a given high value of C_0, there is a declining improvement in the performance curves. So values around 8 (A eq)$^{-1}$ would be enough.

9.1.4. Effect of extracted ion fraction (f_B)

The effect of the extracted ion fraction (f_B) is shown in Fig. 9.11.
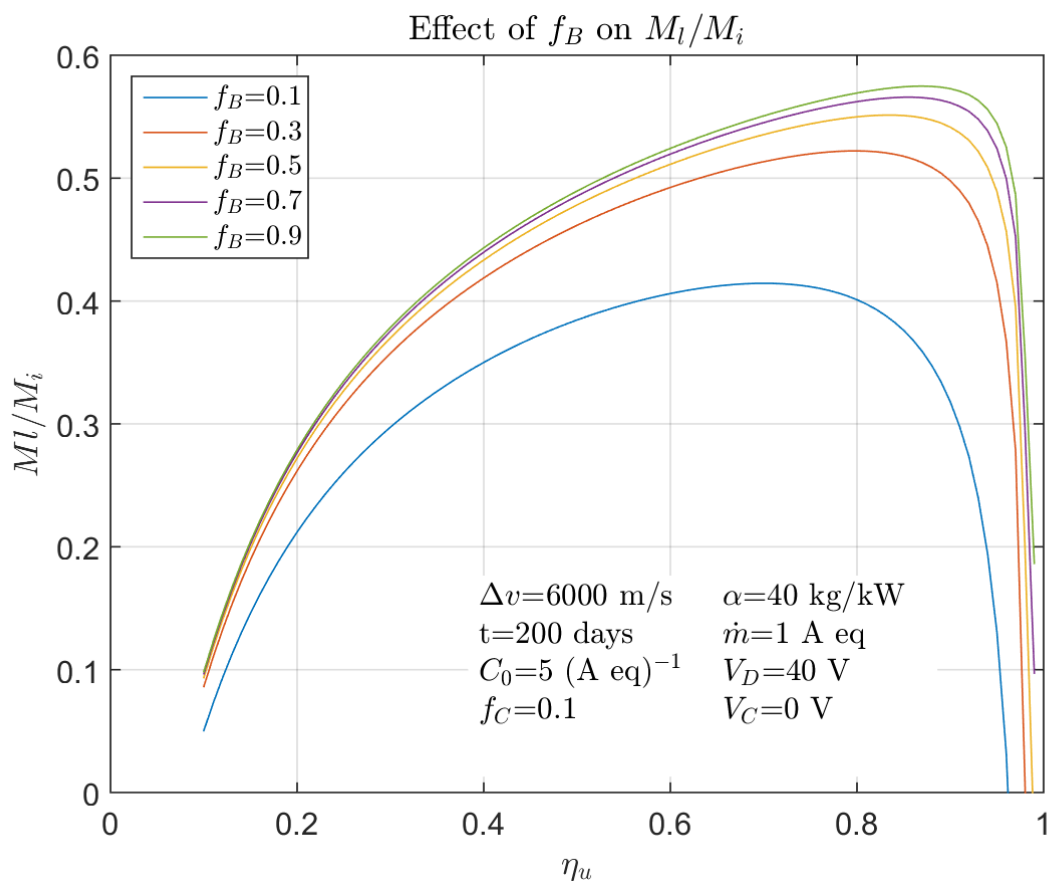
Figure 9.11: Effect of f_B on payload mass fraction curves.

As we can see, higher values of the extracted ion fraction shift up the payload mass fraction curves. Moreover, the "knees" are more sharply defined, although this effect is not as important as for C_0. The beam ion energy costs for the different values of f_B, for their corresponding optimum propellant utilisation efficiencies, are shown below.
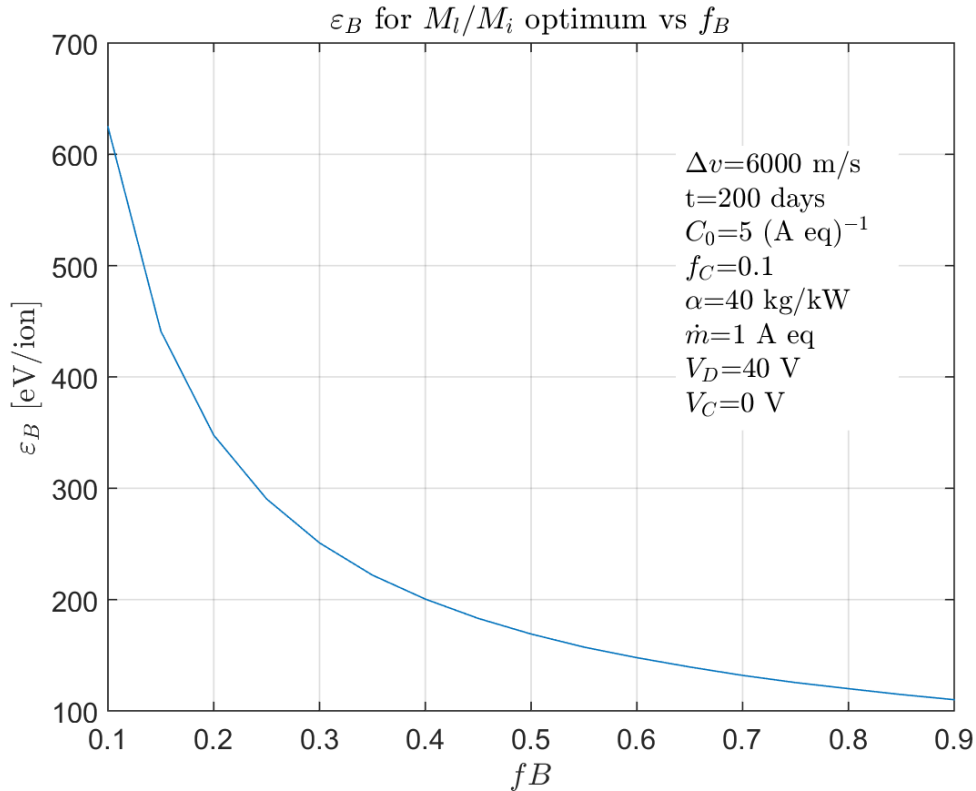
Figure 9.12: Ionisation costs for optimum M_l/M_i as a function of f_B.

We can see that, for higher values of f_B, higher optimum η_u's (Fig. 9.11) and lower ionisation costs (Fig. 9.12) are obtained. Therefore, as well as we deduced for C_0, values as high as possible are desired. Nevertheless, for the given thruster configuration, the extracted ion fraction is constant, and equal to 0.5 for the engine that is being studied. As said in section 6, this parameter calculation is not covered in this work.

Until now, we have studied the effect of three parameters that mainly depends upon the thruster design (α, C_0 and f_B). We have seen that they greatly determines the payload mass fraction curves and the ionisation costs for optimum operation.

After analysing the results, taking into account the advantages and drawbacks of each parameter mentioned before, we can conclude that the following are the ideal ranges in which they should be.

Parameter	Range
α [kg/kW]	0.009-0.035
C_0 [(A eq)$^{-1}$]	3-10
f_B	0.4-0.7

Table 9.1: α, C_0 and f_B parameters' optimum ranges.

The parameters' ranges have been selected in order to keep the ionisation costs under a limit (~200 eV) and get a relatively high propellant utilisation efficiency (>0.8).

9.2. Specific mission analysis

In the previous section, we have employed a generic mission (prescribed Δv and t) in order to assess the influence of three parameters affecting the thruster's performance (α, C_0 and f_B), which are, essentially, a function of the thruster design.

The present analysis is intended to determine the control parameters ($\dot{m}$, η_u, I_{sp}, V_N and T) of our thruster, which are not fixed, in order to achieve the best mission's performance (t and M_l/M_i) for an specific mission.

To that end, we will make use of the two orbit transfers with electric propulsion studied in Chapter 3. That is, a transfer from a highly elliptical orbit (SSTO with 78,000 km apogee and 6771 km perigee radius) to a geosynchronous orbit, and a transfer from LEO (300 km altitude) to GEO.

9.2.1. Constant parameters

First of all, we must set the known initial parameters that affect the performance of the specific mission and the given ion thruster.

From Chapter 3, we have the initial vehicle mass ($M_i = 2205\ kg$). M_i is common for both transfers and it has an important impact on the manoeuvre time (t). On the other hand, we also need the Δv of the mission, since Eq. 9.14 depends on it. Δv is also a fixed parameter (not common in both transfers) that only depends on the orbits used. However, if we consider the transfer from SSTO to GEO, the thrust is not applied parallel to the spacecraft's velocity, and it would be difficult to determine Δv analytically. Therefore, it will be determined from the rocket equation once the time (t) is obtained. In the case of the spiral climb, Δv is just the difference between initial and final velocities [24]. Even though, it will be calculated in the same way as in the other transfer. As we will see, the values obtained will result the same as the calculated in Section 3.2.

The parameters defining the thruster's performance will be taken from actual experimental data.

Extracted ion fraction (f_B) and fraction of ion current to cathode surfaces (f_C) values are assumed to be those obtained for a ring cusped ion thruster fed with xenon in [30]. As it has been stated before, such parameters are constant for a given thruster design, and they don't depend on the operating point of the device. C_0, on the contrary, is a function of the discharge voltage (V_D) and the hollow cathode potential (V_C). However, such voltages will be assumed constant since their optimum values are essentially a function of the propellant.

$$f_B = 0.5 \qquad\qquad f_C = 0.1 \qquad\qquad C_0 = 8\ (A\ eq)^{-1}$$

$$V_D = 40\ V \qquad\qquad V_C = 10\ V$$

On the other hand, the specific power plant mass (α) will be taken from the ion thruster employed to perform the mission analysis in Section 3.1.2 [13].

$$\alpha = 0.03\ kg/W$$

It is noteworthy to mention that all the values of the parameters analysed in Section 9.1 are in their optimum range (Table 9.2).

Parameter	Value
α [kg/kW]	0.03
C_0 [(A eq)$^{-1}$]	8
f_B	0.5
f_C	0.1
V_D [V]	40
V_C [V]	10
M_i [kg]	2205

Table 9.2: Summary of constant parameters for both missions.

9.2.2. Solving process

The main control parameter of this study will be the thruster propellant flow rate $(\dot{m})$. We want to analyse the variation of the following parameters with $\dot{m}$.

- $\eta_{u_{opt}}$
- $I_{sp_{opt}}$
- $\varepsilon_{B_{opt}}$
- V_N

- T
- t
- $\frac{M_l}{M_i}$

This analysis will give us a rough idea about the capabilities of our propulsion system, as well as the power requirements to perform such missions.

First of all, we will impose the flow rate $(\dot{m})$, and we will use it to calculate the thrust provided by the engine, which is given by,

$$T = \frac{J_B m_i}{e} u = \frac{\dot{m}\eta_u m_i}{e} u \qquad (9.16)$$

Having the thrust and the flow rate, we would be able to determine the time invested in performing the orbit transfer, as well as the Δv provided by the engine over the trajectory. The latter can be calculated using the rocket equation (Eq. 9.17),

$$\Delta v = \ln\left(\frac{M_i}{M_f}\right) u \eta_u \tag{9.17}$$

where M_f is,

$$M_f = M_i - \dot{m}_p t \tag{9.18}$$

being $\dot{m}_p$ constant over the whole mission.

As we can see in Eqs. 9.16 and 9.17, the thrust and Δv depend on η_u and u. Those are some of the parameters that we want to determine in order to optimise the thruster operation. They must be obtained following the process detailed in Section 9.1.1. The basic equation (Eq. 9.14) of that study is retrieved here below,

$$\frac{M_l}{M_i} = e^{-(\Delta v/\eta_u u)} - \frac{\alpha u^2 \eta_u}{2t}\left(1 + \frac{2e\varepsilon_B}{m_i u^2}\right)\left(1 - e^{-(\Delta v/\eta_u u)}\right) - \frac{M_{g_0}}{M_i}$$

Eq. 9.14 shows that, in order to find the optimum values of η_u, u, $\frac{M_l}{M_i}$ and ε_B, we would need the time (t) and the Δv of the mission.

Therefore, an iterative process must be applied. We should suppose initial values for η_u and u, and repeat the process detailed above until reach a convergent solution for both parameters.

9.2.3. Results

In order to approximate this study as much as possible to the reality, the propulsion system of the spacecraft will consist of 4 ion thrusters, just as the mission analysis undertaken in Section 3.1.2.

Therefore, when computing the total thrust provided to the vehicle, the mass propellant flow will be multiplied per 4:

$$T_T = 4\dot{m}_p \eta_u u = \dot{m}_{p_T} \eta_u u \tag{9.19}$$

The mass flow considered when determining the thruster's performance will be that of a single engine ($\dot{m}_p = \dot{m}_{p_T}/4$).

The propellant flow rates ($\dot{m}$) tested have been, for both transfers, 0.5, 1, 2, 4, 6, 8 and 10 A eq.

In the following two tables, we can see the thruster's parameters that optimise the payload mass fraction of each mission for the different values of propellant flow rate. It should be noted that, parameters of the transfer using circular orbits (spiral climb) are denoted by the superscript (^{C}). On the other hand, the transfer mission starting from the supersynchronous orbit is denoted by (^{S}).

$\dot{m}$ [A eq]	T^C/engine [mN]	$\eta_{u_{opt}}^C$	$I_{sp_{opt}}^C$ [s]	$\varepsilon_{B_{opt}}^C$ [eV/ion]	V_N^C [V]
0.5	41	0.898	6932	354.1	1978
1	65	0.911	5398	226.0	1219
2	104	0.923	4211	161.0	755
4	166	0.936	3303	131.1	479
6	218	0.945	2879	123.1	373
8	267	0.951	2616	119.6	316
10	312	0.956	2434	118.0	280

Table 9.3: Optimum thruster's parameters for different $\dot{m}$ for spiral climb transfer.

$\dot{m}$ [A eq]	T^S/engine [mN]	$\eta_{u_{opt}}^S$	$I_{sp_{opt}}^S$ [s]	$\varepsilon_{B_{opt}}^S$ [eV/ion]	V_N^S [V]
0.5	32	0.874	5502	295.3	3140
1	51	0.890	4319	195.6	1904
2	82	0.906	3398	146.6	1159
4	134	0.924	2707	125.3	713
6	180	0.936	2389	119.9	542
8	222	0.944	2198	117.7	447
10	262	0.951	2071	116.8	387

Table 9.4: Optimum thruster's parameters for different $\dot{m}$ for transfer from SSTO.

Down below, the resulting main features of the missions are presented.

$\dot{m}$ [A eq]	T_T^C [mN]	Δv^C [km/s]	t^C [months]	M_l/M_i^C
0.5	165	4.677	23.163	0.841
1	262	4.672	14.479	0.802
2	416	4.667	8.993	0.752
4	663	4.666	5.555	0.685
6	873	4.666	4.172	0.634
8	1067	4.665	3.387	0.590
10	1247	4.665	2.879	0.551

Table 9.5: Mission's performance for different $\dot{m}$ for spiral climb transfer.

$\dot{m}$ [A eq]	T_T^S [mN]	Δv^S [km/s]	t^S [months]	M_l/M_i^S
0.5	129	2.035	13.153	0.903
1	204	2.035	8.256	0.879
2	329	2.035	5.086	0.846
4	536	2.035	3.099	0.798
6	719	2.035	2.299	0.760
8	890	2.036	1.852	0.726
10	1047	2.036	1.570	0.695

Table 9.6: Mission's performance for different $\dot{m}$ for transfer from SSTO.

As we can see in tables 9.5 and 9.6, the Δv budgets are constant for both transfers, as expected, since they only depend on the initial and final orbits. Moreover, we should note that, for both missions, the values correspond with those obtained in Section 3.2.

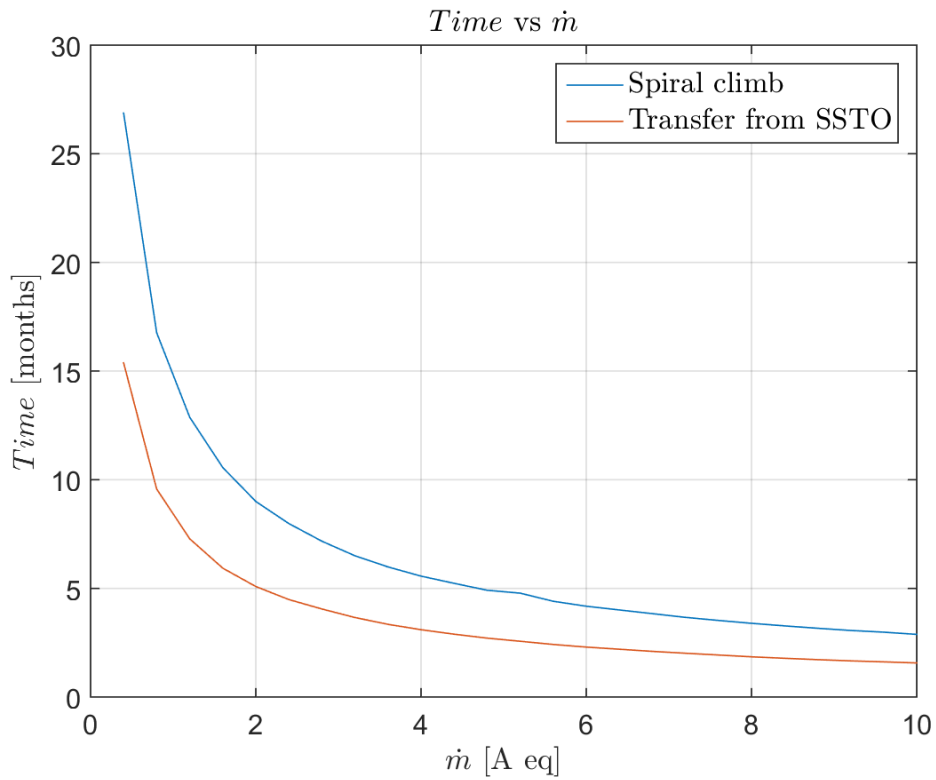Hereafter, some of the results found above are graphically depicted, in order to easily analyse them.

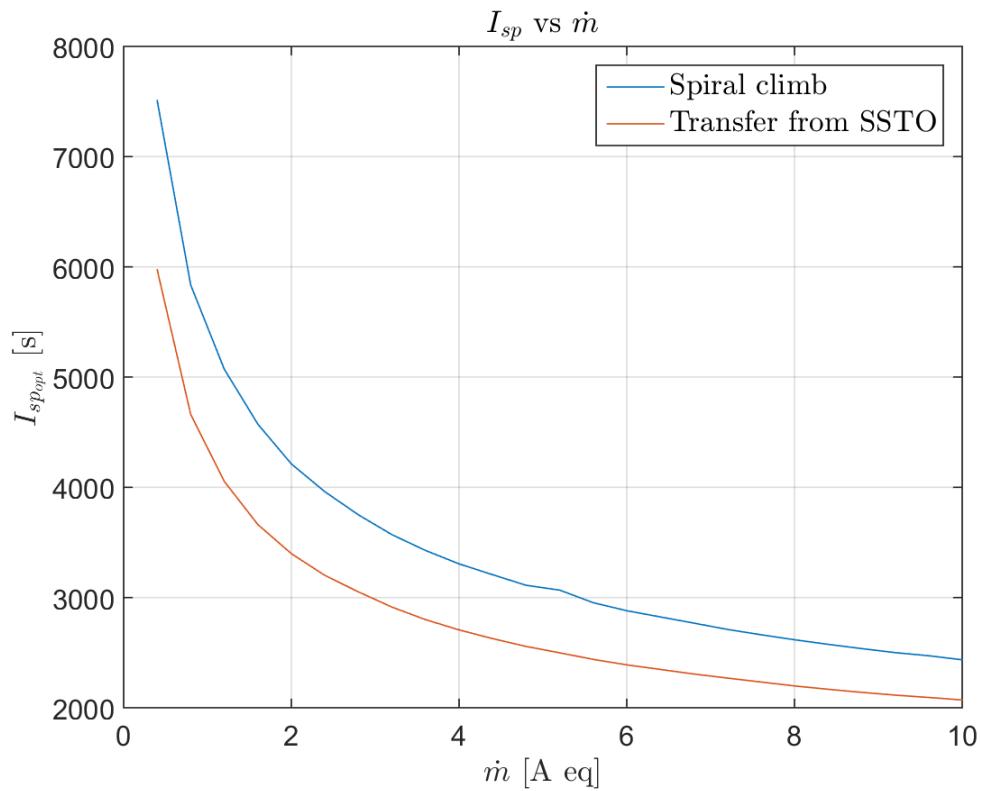*Figure 9.13: Mission duration as a function of the propellant flow rate.*

Figure 9.14: Optimum specific impulse as a function of the propellant flow rate.

As expected, the time invested to transfer the vehicle decreases as $\dot{m}$ is increased (Fig. 9.13), since the thrust, as shown in tables 9.5 and 9.6, also increases with the propellant flow rate. We should note that the mission time is always smaller for the transfer from SSTO, for a given $\dot{m}$, as predicted in Section 3.2. Consequently, the propellant mass required is also lower than for a spiral climb.

From Fig. 9.14, we can draw that $I_{sp_{opt}}$ decreases as $\dot{m}$ is increased. It is important to note that, at very low propellant flow rates, optimum specific impulses imply too high net voltages (V_N), as indicated in tables 9.3 and 9.4. Therefore, we could conclude that, for assuring an appropriate thruster operation, propellant flow rates higher than 1 A eq. should be employed.
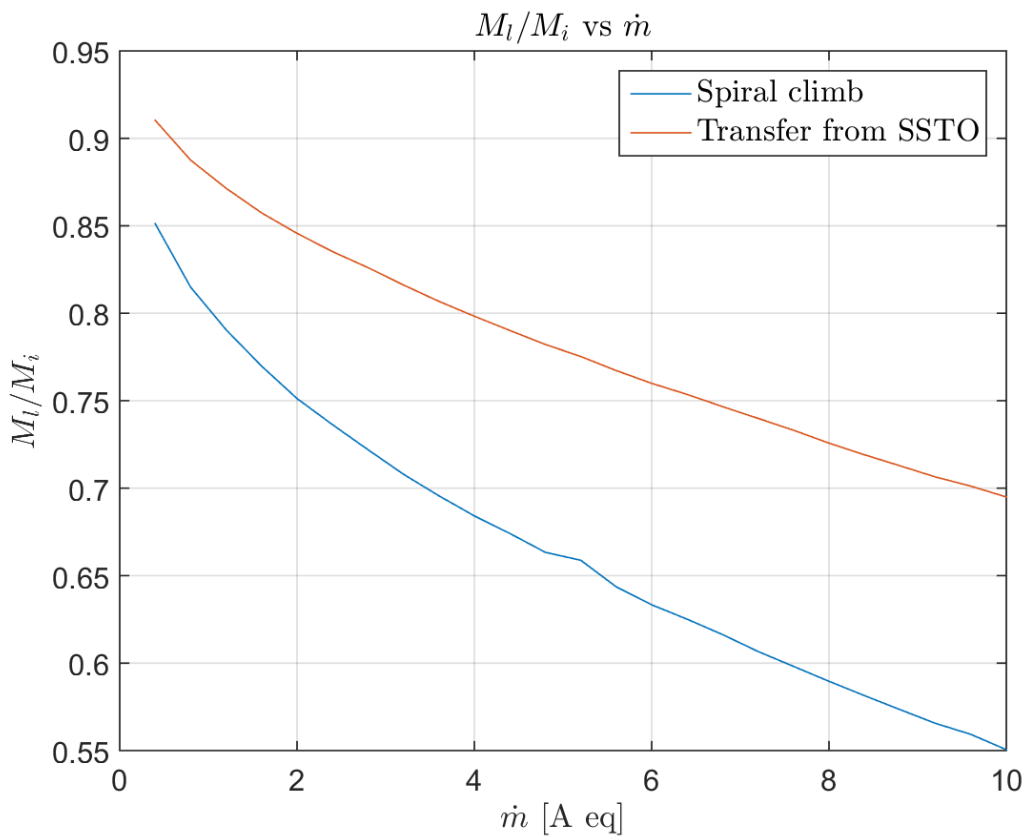

Figure 9.15: Payload mass fraction as a function of the propellant flow rate.

Figure 9.15 shows that M_l/M_i decreases when rising the propellant flow rate. Thus, in order to carry a larger payload mass, smaller $\dot{m}$'s are needed and, consequently, longer mission times.
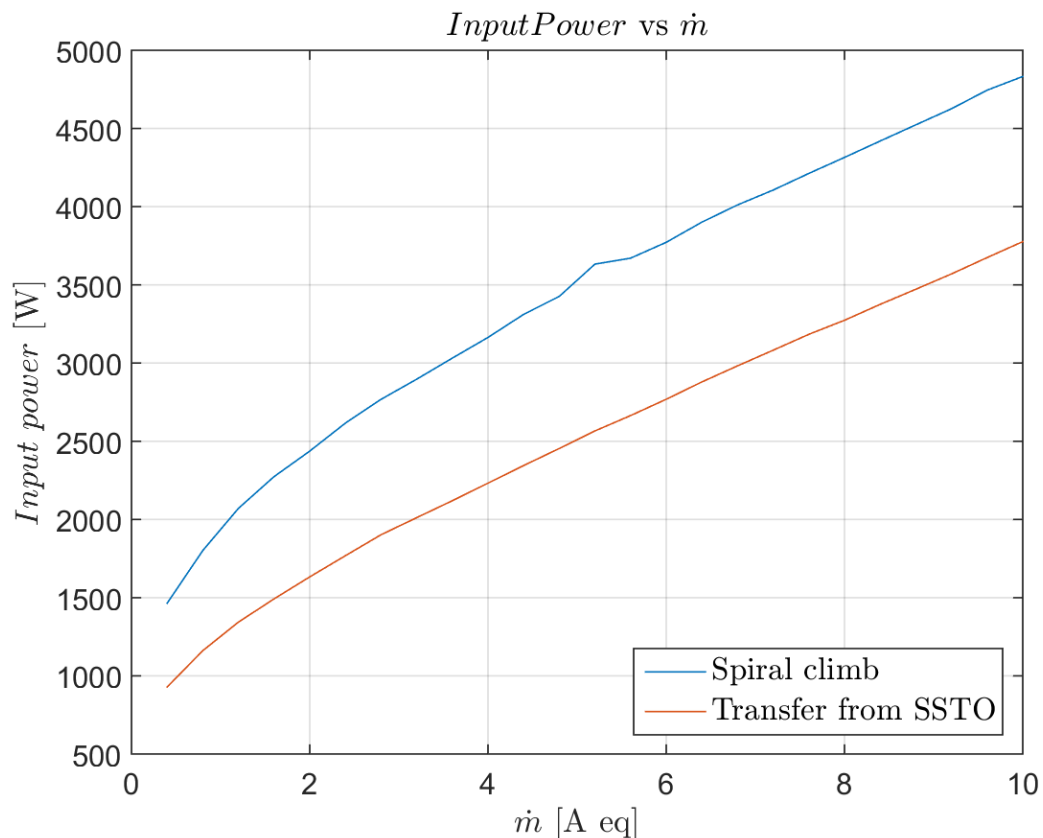
Figure 9.16: Thruster input power as a function of the propellant flow rate.

Fig. 9.16 shows the required power to operate a single ion thruster as a function of $\dot{m}$. It has been computed from data in tables 9.3 and 9.4, and using Eq. 6.9, where we firstly defined this term. Input power is a very important issue to take into consideration when designing a spacecraft. The more power you need, the larger power supplies you require, and the heavier the spacecraft is. For example, it would give us a rough idea about the size of the solar panels employed to feed the propulsion system of a satellite. As we can see, this input power increases with the propellant flow rate and, therefore, if we wanted to save mission time, we should fit the spaceship with more powerful electric suppliers.

We also should keep in mind that, power presented in Fig. 9.16, only takes into consideration the engine demands, but not the power controller and power processor units, which are necessary devices to operate the thrusters. They add weight and power demands to the spacecraft.
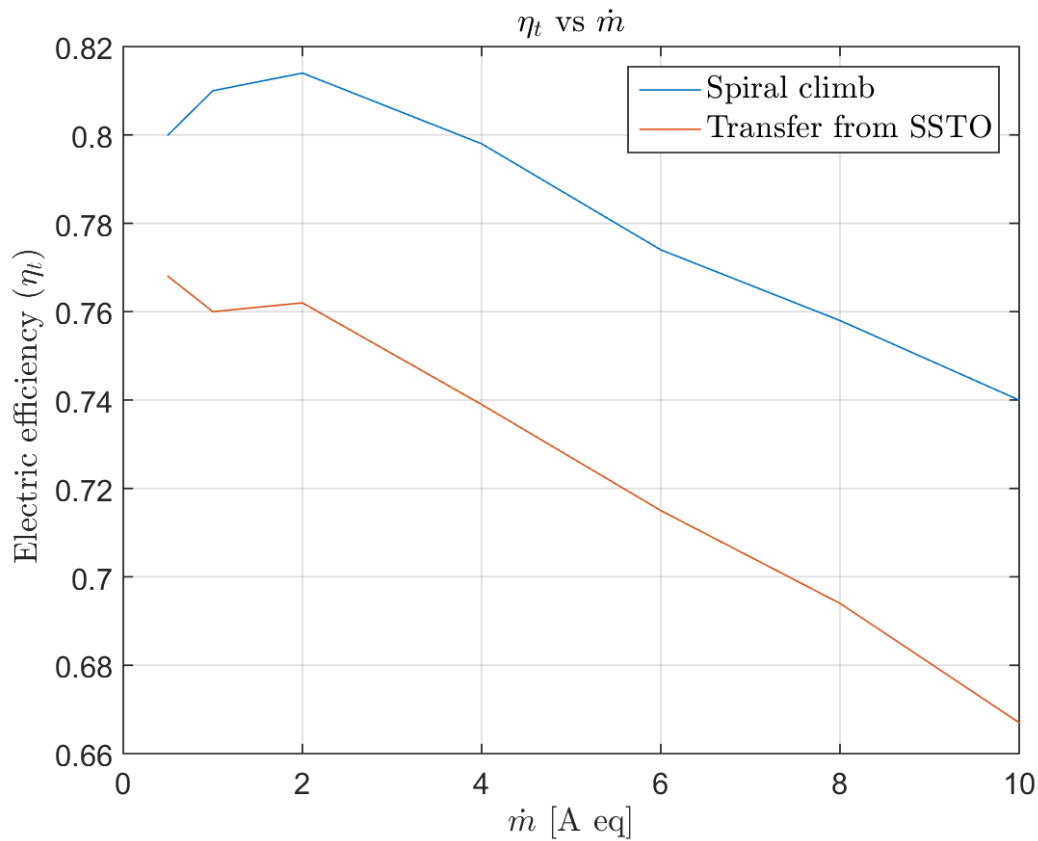
Figure 9.17: Thruster's overall efficiency as a function of the propellant flow rate.

Finally, in Fig. 9.17, we can see the overall thruster's efficiency, given as the ratio of the produced power by the exhaust stream to the total input power.

$$Produced\ power = \frac{1}{2}u^2\dot{m}_p\eta_u = \frac{T^2}{2\dot{m}_p\eta_u}$$

As we can see, results obtained are close to typical achievable values for ion thrusters (0.6-0.8) [33]. This high efficiency is one of the main reasons why ion thrusters have been historically considered in space missions as the main electric propulsion system, besides their low power consumption and high specific impulse.

Chapter 10. Conclusions and future work

The main goal of this work was to develop a preliminary study of an ion thruster, in a way which could be useful for optimising its performance for certain mission's specifications. Moreover, a feasibility study was needed in order to assess the suitability of an electrostatic ion engine for different in-space manoeuvers.

Through a state-of-the-art research, it has been demonstrated that the ion thruster is the most used electric propulsion system for station keeping or deep-space manoeuvers, operations requiring a large delta-V budget which may be delivered over long periods of time. This is because it provides reasonable thrust levels, at high specific impulses, with high efficiencies. Nevertheless, another promising application has recently arisen for this kind of devices, orbit transfers.

We have performed a quantitative comparison between different transfers (all of them with the same target, GEO) carried out either by chemical engines or ion thrusters. We can draw several conclusions. Electric propulsion systems cut down launch costs, with respect to chemical propulsion, since they allow to undertake the manoeuvers employing significantly less propellant mass. This results in lighter spacecraft to be placed into orbit, or the possibility of increasing the payload. The problem is that mission's duration increases, from days or weeks to several months. Even so, the electrically propelled transfer was analysed considering different points of departure and using different techniques to reach the same final orbit. On the one hand, the results show that, employing an SSTO (instead of LEO), mission times can be reduced by more than 50 per cent. On the other hand, launcher delta-V requirements are increased. There is a trade-off between time and costs. The transfer from SSTO to GEO is in an intermediate point between chemical and electric propulsion (spiral climb). Therefore, it has been recently introduced as a possible low-cost solution for companies which cannot afford placing their satellites into orbit because of the high costs involved.

For the purpose of analysing the working principle of ion thrusters, we focused our study on the most developed and refined one, the electron bombardment ion thruster. Its operation can be divided into two main stages, ion extraction and acceleration system, and ionisation chamber.

The analysis of the former one has enabled us to determine the parameters affecting the extracting capabilities of the grids. The theoretical one-dimensional model developed in section 5.2.1 provides an analytical expression to define the maximum beam ion current that a specific accelerating system could extract. This is achieved imposing one of the main limitations of these devices, the space charge limit condition. The other limitation is breakdown or shorting phenomena. The model is useful to know the dependencies between the maximum current and the different geometrical parameters of the grids, the propellant or the potential difference between electrodes. However, it does not provide accurate results if compared with experimental data from tested ion thrusters. Several corrections are required in order to take into consideration three-dimensional effects, being this out of the scope of the project. It would be going one step further and it would be part of a possible future work.

Brophy's Theory has been used to develop a quasi-unidimensional model of the discharge chamber, providing results for the ionisation costs for different operating conditions (different discharge voltages, propellant utilisation efficiencies and flow rates). Outcomes have been validated carrying out a comparison between them and experimental data from a line-cusp and a ring-cusp ion thrusters. The model has demonstrated to be successful with an average error of 2 % in the evaluation of the chamber's performance. Both tested thrusters were operated without hollow cathode. Although our model is ready for simulating designs with and without hollow cathode, it has not been validated for engines fitted with one of them. Validating such results would be a further step on the refinement of the program and it could be part of a future work.

As said above, the ionisation chamber model allows us to determine the thruster's performance given some operating conditions, but it also enables us to know the effect of different parameters on the performance curves. From results in Section 7.2 we can draw the following conclusions. The extracted ion fraction and primary electron utilisation have a very important effect on ionisation costs. They depend exclusively on the thruster's design and values as high as possible are desirable. They might be improved essentially modifying the magnetic fields strength and their layout. This would lead to larger primary electron containment lengths. Nevertheless, the analysis of the magnets disposal and their influence is out of the scope of this project. It would be part of a possible future study to improve the ionisation chamber operation.

Finally, a model was developed in order to optimise the thruster's operation for a specific mission. The model shows that, given a specific mission (delta-V budget and mission duration), there exists an optimum working point which maximise the payload mass fraction. Fixing a thruster design (so, setting parameters that depend upon the engine configuration), the model provides the optimum propellant utilisation efficiency and exhaust velocity that maximises the payload. Using a generic mission, with fixed delta-V budget and mission duration, the effect of performance parameters on the payload mass fraction was observed. Again, the extracted ion fraction and primary electron utilisation showed a very important effect on the curves. Payload mass fraction was increased as they were increased, and ionisation costs were not enhanced.

Moreover, this last model was tested making use of the electrically propelled transfers studied in Chapter 3. This time, delta-V budget and mission duration were not prescribed. Therefore, an analysis of the effect of the propellant flow rate on the optimum operating points and the mission's performance was performed. Results showed that, as propellant flow rate was increased, mission's duration was reduced (this is obvious taking into account that thrust is proportional to flow rate). However, it was also seen that power required to operate the thruster increases, and electrical efficiency and payload mass fraction decreases when rising the propellant flow rate. We can conclude that the model developed has been useful to determine the optimum operation point of a given ion thruster when taking into consideration a specific mission, allowing to modify the propellant flow rate as a function of the requirements (short duration, low electric power consumption, high efficiency, maximum payload, etc.).

Finally, as another possible improvement of the work, it would be interesting to develop a model to evaluate the effect of the magnetic fields on the operation of the ionisation chamber, given the important effect on performance of parameters depending on them.

Chapter 11. Environmental impact

The environmental analysis is divided into two parts, direct impacts, related with the development of this work, and indirect impacts, related with the benefits of the study and electric propulsion.

This study has been mainly developed making use of a personal computer and some sheets of paper, and there are not other direct environmental impacts, since no physical products have been generated. Therefore, the following issues must be taken into account.

- Power consumption: Electricity consumed concerns CO_2 emissions and, according to the *Budget* document [34], 435 hours have been invested to perform the study, which involve the same hours of computer utilisation (160 W). Therefore, 69.60 kWh is the power consumption estimation. According to the Spanish ministry of energy [35], each kWh produces around 0.33 kg CO^2. Therefore, this work has entailed a total production of 20.88 kg of carbon dioxide.
- Paper consumption: It concerns printing of documents needed to perform the study as well as paper used to write down ideas ant take notes. It should be highlighted that deliverables are required in digital format, cutting down, in this way, paper waste.

Here below, indirect environmental impacts, associated with the usefulness of the study, are presented.

As it has been said, up to this day, the development of ion thrusters' designs has been largely experimental, needing expensive and long iterative procedures until an acceptable configuration is obtained. These processes are time consuming and they have a large impact on electric power consumption. Moreover, the manufacture of prototypes involves material waste and debris generation. Making use of the present study would allow to reduce the product design time, since computer simulations should provide a guidance to quickly find an optimum configuration and operating condition.

It is also worth noting that the evolution of the space propulsion towards the extensive use of electric devices (specifically ion thrusters) implies a significant reduction of the launcher propellant, leading to a reduction of greenhouse gases.

Chapter 12. Budget

In this section we present the budget of the work *Design and Performance Analysis Study of an Ion Thruster*, which have been estimated accounting for human resources costs, hardware costs and software costs. In *Budget* document [34], it is explained in detail how costs have been computed. Hereafter, we present a review of it.

Human resources costs have been estimated taking into account dedicated hours to the study, and considering an hourly wage of 15 € per hour for the student and 40 € per hour for the director of the project, who has contributed to the realisation of the work. He was required to provide support and knowledge about several concepts related with space propulsion with which the student was not familiar. Additionally, an overhead of 10 % has been applied since the work extends for 4 months.

On the other hand, hardware and software costs accounts for price of the equipment employed and licenses of the software used to carry out the study. We have considered a 25 % annual amortisation of the personal computer.

In addition, the electrical power consumption has been considered, which is the result of the hardware usage during the project development.

Finally, by adding all the costs, we can obtain the total budget of the study, which has been estimated in 8771.81 €.

Concept	Cost [€]
Human resources	8448.00
Hardware	58.33
Software	254.00
Electricity	11.48
Total costs	8771.81

Table 12.1: Budget of the work Design and Performance Analysis Study of an Ion Thruster.

Bibliography

[1]   Jet Propulsion Laboratory (NASA), "Power On! Ion Propulsion System." [Online]. Available: http://dawn.jpl.nasa.gov/technology/ion_prop.asp. [Accessed: 09-Jun-2016].

[2]   R. G. Jahn and E. Y. Choueiri, "Electric Propulsion. Technology Programmes," *ESA Publications Division*, 2002.

[3]   E. Y. Choueiri, "A Critical History of Electric Propulsion: The First 50 Years (1906-1956)," *Journal of Propulsion and Power*, vol. 20, no. 2, pp. 193–203, 2004.

[4]   NASA, "Glenn Contributions to Deep Space 1," 14-Apr-2015. [Online]. Available: http://www.nasa.gov/centers/glenn/about/history/ds1.html. [Accessed: 23-Mar-2016].

[5]   M. J. L. Turner, *Rocket and spacecraft propulsion*, 2nd ed. Leicester, UK: Springer International Publishing, 2005, p.145-166. ISBN 3-540-22190-5

[6]   "ME 599 Final Review Flashcards." [Online].
        Available: http://www.cram.com/flashcards/me-599-final-review-2500724. [Accessed: 04-Jun-2016].

[7]   E. Y. Choueiri, "New Dawn for probes to the outer solar system," *Scientific American*, pp. 58–65, 2009.

[8]   F. R. Chang, "The VASIMR Rocket," *Scientific American*, vol. 283, no. 5, 2000.

[9]   S. Anthony, "NASA's NEXT ion drive breaks world record, will eventually power interplanetary missions." [Online].
        Available: http://www.extremetech.com/extreme/144296-nasas-next-ion-drive-breaks-world-record-will-eventually-power-interplanetary-missions. [Accessed: 09-Jun-2016].

[10]   B. W. Longmier, J. P. Squire, L. D. Cassady, M. G. Ballenger, M. D. Carter, C. Olsen, A. V Ilin, T. W. Glover, G. E. Mccaskill, and F. R. C. Díaz, "VASIMR ® VX-200 Performance Measurements and Helicon Throttle Tables Using Argon and Krypton,"

32nd International Electric Propulsion Conference, 2011.

[11] R. G. Jahn and E. Y. Choueiri, "Electric Propulsion," *Encyclopedia of Physical Science and Technology*, vol. 5, pp. 125–141, 2002.

[12] SITAEL, "PRODUCT SHEET AT 1k Arcjet," Technical report, 2015.

[13] L.-3 E. Technologies, "25 cm Xenon Ion Propulsion System (XIPS ®) Thruster and XIPS Power Controller (XPC)," Technical report, 2015.

[14] B. Welander, J. Monheiser, N. Meckel, K. De Grys, P. Peterson, Aerojet, and L. Martin, "Demonstration of the XR - 12 Hall Current Thruster," *33rd International Electric Propulsion Conference*, pp. 1–10, 2013.

[15] Glenn Research Center (NASA), "SPACE ELECTRIC ROCKET TEST II (SERT II)," 2009. [Online]. Available: http://www.grc.nasa.gov/WWW/ion/past/70s/sert2.htm. [Accessed: 23-Mar-2016].

[16] M. Martínez Sánchez, "Session 10-11 : Electrostatic Thrusters (Kaufman Ion Engines)," Lecture notes , 2004.

[17] Wikipedia, "Eutelsat 115 West B," 2016. [Online].
Available: https://en.wikipedia.org/wiki/Eutelsat_115_West_B.   [Accessed: 23-Mar-2016].

[18] Wikipedia, "List of spacecraft with electric propulsion." [Online]. Available: https://en.wikipedia.org/wiki/List_of_spacecraft_with_electric_propulsion.   [Accessed: 23-Mar-2016].

[19] R. Frost, "How does one launch satellites into a geostationary orbit?," 2014. [Online]. Available: https://www.quora.com/How-does-one-launch-satellites-into-a-geostationary-orbit. [Accessed: 05-Jun-2016].

[20] C. Bergin, "Legless Falcon 9 conducts Static Fire test ahead of Sunday launch," 2015. [Online].   Available: http://www.nasaspaceflight.com/2015/02/legless-falcon-9-static-

fire-ahead-launch/. [Accessed: 17-Jun-2016].

[21] C. Sánchez, "Design and Performance Analysis Study of an Ion Thruster: Annex," Terrassa, 2016.

[22] AEROJET, "BIPROPELLANT ROCKET ENGINE," Technical report, 2006.

[23] K. Chien, K. Chien, S. L. Hart, S. L. Hart, W. G. Tighe, W. G. Tighe, M. K. De Pano, M. K. De Pano, T. a Bond, T. a Bond, R. Spears, and R. Spears, "L-3 Communications ETI Electric Propulsion Overview," *29th Int. Electr. Propuls. Conf. 2005*, 2005.

[24] M. Martínez Sánchez, "Lecture 3: Approximate ∆V for Low-Thrust Spiral Climb," Lecture notes, 2004.

[25] Chemicool, "Xenon Element Facts," 2012. [Online].
Available: http://www.chemicool.com/elements/xenon.html. [Accessed: 16-Jun-2016].

[26] Astronautix, "N2O4/Hydrazine." [Online].
Available: http://www.astronautix.com/props/n2oazine.htm. [Accessed: 16-Jun-2016].

[27] M. Martínez Sánchez, "Session 8: Basic Electromagnetic Theory and Plasma Physics," Lecture notes, 2015.

[28] M. Martínez Sánchez, "Lecture 13-14: Electrostatic Thrusters," Lecture notes, 2004.

[29] Wikipedia, "Ionisation," 2016. [Online].
Available: https://de.wikipedia.org/wiki/Ionisation. [Accessed: 09-Jun-2016].

[30] J. R. Brophy, "ION THRUSTER PERFORMANCE MODEL," Colorado, 1984.

[31] D. M. Goebel and I. Katz, *Fundamentals of Electric Propulsion: Ion and Hall Thrusters*, 1st ed. Hoboken, New Jersey: John Wiley & Sons, 2008, p.471-478. ISBN 978-0-470-42927-3

[32] V. K. Rawlin, "Operation of the J-series thruster using inert gas," *AIAA Paper*, no. 82–

1929, 1982.

[33]   J. S. Sovey, "Improved ion containment using a ring-cusp ion thruster," *AIAA Paper*, no. 82–1928, 1982.

[34]   C. Sánchez, "Design and Performance Analysis Study of an Ion Thruster: Budget," Terrassa, 2016.

[35]   Ministerio de Industria Energía y Turismo, "Factores de emisión de CO2 y coeficientes de paso a energía primaria de diferentes fuentes de energía final consumidas en el sector de edificios en España," Technical report, 2014.